PROTEIN CAGE ARCHITECURES AS A NANO-PLATFORM FOR MATERIAL SYNTHESIS AND METAL BINDING

by

Mark Andrew Allen

A dissertation submitted in partial fulfillment
of the requirements for the degree

of

Doctor of Philosophy

In

Chemistry

MONTANA STATE UNIVERSITY
Bozeman, Montana

July 2006

APPROVAL

of dissertation submitted by

Mark Andrew Allen

This dissertation has been read by each member of the dissertation committee and has been found to be satisfactory regarding content, English usage, format, citations, bibliographic style, and consistency, and is ready for submission to the Division of Graduate Education.

Dr. Trevor Douglas

Dr. Mark Young

Approved for the Department of Chemistry and Biochemistry

Dr. David Singel

Approved for the Division of Graduate Education

Dr. Joseph J. Fedock

STATEMENT OF PERMISSION TO USE

In presenting this dissertation in partial fulfillment of the requirements for a doctoral degree at Montana State University, I agree that the Library shall make it available to borrowers under rules of the Library. I further agree that copying of this dissertation is allowable only for scholarly purposes, consistent with "fair use" as prescribed in the U.S. Copyright Law. Requests for extensive copying or reproduction of this dissertation should b e referred to ProQuest Information and Learning, 300 North Zeeb Road, Ann Arbo, Michigan 48106, to whom I have granted "the exclusive right to reproduce and distribute my dissertation in and from microform along with the non-exclusive right to reproduce and distribute my abstract in any format in whole or in part."

Markk Allen

July 2006

ACKNOWLEDGEMENTS

I would like to thank the following people who have contributed to the research presented in this disseration. I gratefully acknowledge myt advisors for allowing me to conduct research in their laboratories. First and foremost, thanks to Dr. Trevor Douglas and Dr. Mark Young for their continual scientific mentorship. I greatly appreciate each member of the Youn/Douglas laboratories, especially Zack Varpness. Many members of the group have had a direct impact on the research performed, specifically Dr. Michael Klem for his help in understanding magnetic characterization as well as data collection at the synchrotron light sources, Lars Liepold for his work on relaxivity measurements, Matt Prissel for friendship and work with 3D image reconstruction on the TEM. In the Young lab I greatly appreciate the help of Debbie Willits for her work in performing mutagenesis on some of the protein cages, and Sue Brumfield for her help on the TEM. I thank Yves Idzerda and group members, especially Keith Gilmore for work on the synchrotron runs and helping me understand magnetic measurements.

I appreciate the support of a lively cast of friends in the Bozeman area and to my family. Finally, and most of all, I thank God for getting me through it all.

TABLE OF CONTENTS

TABLE OF CONTENTS - CONTINUED

TABLE OF CONTENTS - CONTINUED

TABLE OF CONTENTS - CONTINUED

LIST OF TABLES

LIST OF FIGURE

LIST OF FIGURES - CONTINUED

LIST OF FIGURES – CONTINUED

Figure Page

LIST OF FIGURE – CONTINUED

Figure Page

ABSTRACT

Supramolecular proteins that assemble into cage like architectures have been used for nano-material synthesis and as a scaffold for metal binding. Material synthesis can be performed by exploiting the cage-like properties of these nano-containers and relying on the electrostatically distinct interior environment that drive mineral encapsulation. Ferritin and ferritin like proteins can be used as size constrained reaction vessels that encapsulate materials that have sizes that are determined by the internal dimensions of the protein cage. These range from 5 nm for the ferritin like protein from *Listeria innocua* to 24 nm for the interior of an engineered plant virus (Cowpea chlorotic mottle virus). Inorganic materials synthesized within these constrained reaction volumes are monodisperse in size. The crystallinity and phase of material prepared is determined by the reaction conditions, which are mild compared to other preparative methods. The metal binding affinity of certain viral protein cages allows the study of the role that metals play in such processes as viral assembly and infection as well as transmission. If paramagnetic metal ions are bound to the viral protein cage, the biological scaffold has potential use as an MRI contrast agent.

Here multiple protein cage platforms are discussed with an emphasis on engineering non-native functionality to many of the protien cages. Engineering non-native function to protein cages involves both genetic and chemical modification for the purpose of increaseing stability and changing electrostatic interactions. Together these modifications serve to reinforce the versatility of protein cage architectures for both mineral synthesis and metal binding.

INTRODUCTION AND BACKGROUND

Protein Cage Architectures

Biological systems have developed an amazing ability to control the hierarchical assembly of both hard (biominerals) and soft (supramolecular protein/lipid assemblies) materials. In most biological systems there is a marriage between the hard mineral in intimate contact with macromolecules (proteins, carbohydrates, lipids) to form a complex composite material in a process known as biomineralization. For instance, strands of fibrous collagen protein enable the crystallization of apatite crystals that perpetuate to form bone. In the structure of bone, the protein remains present and adds strength and flexibility. In most biological minerals some organic matrix is used in order to both facilitate the mineralization of a particular crystal phase and to stabilize the hard product[1]. Among the many interesting facets of biomineralization is the ability of soft biomolecules to constrain and encapsulate a mineral within an organic matrix. One of the clearest examples of this is the protein cage ferritin which is found nearly ubiquitously throughout biology and is responsible *in vivo* for the sequestering of toxic Fe(II) ions and storing it as an innocuous nano-particle of iron oxide.

There are a number of protein cage architectures that are similar to ferritin in that they are all assembled from a distinct number of subunits to form a precisely defined container in the 5-100 nm size regime. Among these cage like nano-containers are chaperonins[2-4], DNA binding proteins [5-15]and a very large class of protein cages; viruses and virus like particles (VLP)[16-27]. Typically protein cages are roughly spherical

in nature and represent a range of relatively simple symmetries including tetrahedral, octahedral, and icosahedral. Protein cage architectures assemble using precisely defined symmetries because simple symmetry operations allow for identical subunits to come together with a maximum number of noncovalent interactions, and also allow the encapsulation of the largest possible cavity from a minimal number of subunits [28]. While many viruses assemble into capsids that can have a broad range of alternative structures, they are outside the scope of this dissertation, which only focuses on using cages as size-constrained reaction vessels for material synthesis.

A library of protein cage architectures has been developed by multiple groups in order to demonstrate different functionality for biomimetic materials synthesis, magnetic

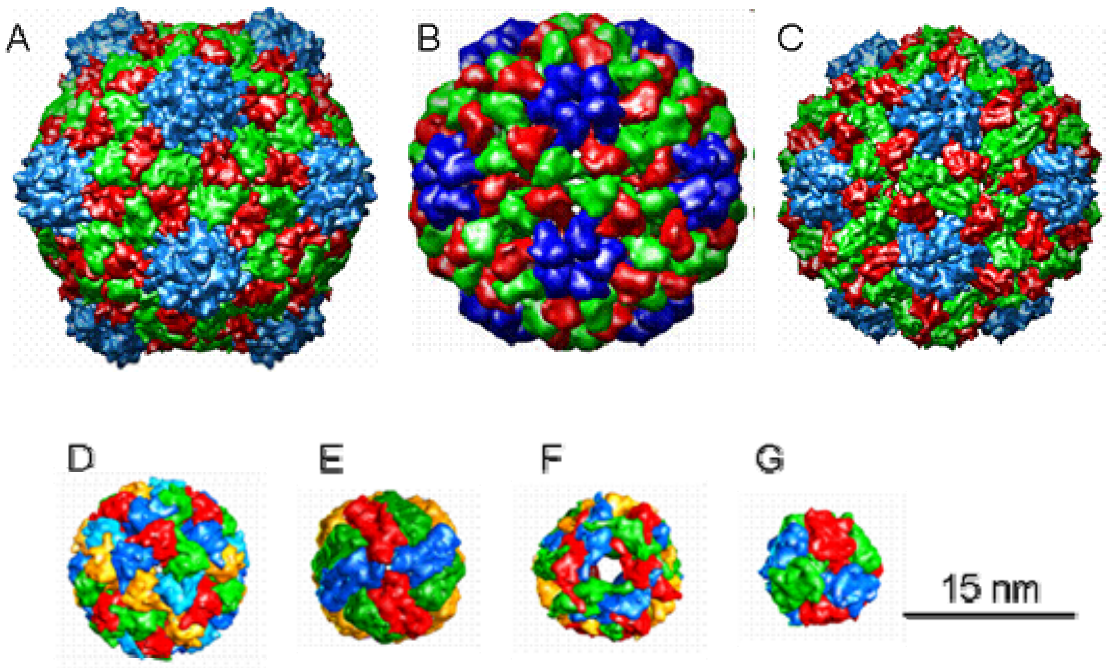

Figure 1.1: Library of protein cages, A. Cowpea mosaic virus (31 nm, 60 subunits), B.Cucumber mosaic virus (29 nm, 180 subunits), C. Cowpea chlorotic mottle virus (28 nm, 180 subunits) [32], D. Lumazine synthase (15 nm, 63 subunits), E. Ferritin (12 nm, 24 subunits), F. Small heat shock protein (12 nm, 24 subunits), G. DNA binding protein from starved cells (9.5 nm, 12 subunits) .

resonance imaging (MRI) contrast agents, gene therapy, drug encapsulation, cell specific targeting, and catalysis (Figure 1.1)[29-32]. In each of these protein cages there are three interfaces that have properties of interest to both materials and biomedical research, and which can be modified by design. These are the exterior surface, the interior surface, and the interface between subunits represented schematically in figure 1.2. All of the protein cages represented in figure 1.1 have been manipulated by both chemical and genetic modification to add non-native functionality to the cage.

The goal of this dissertation research is two fold: (1) to understand how protein cage architectures can be used for the biomimetic synthesis of nanometer scale materials

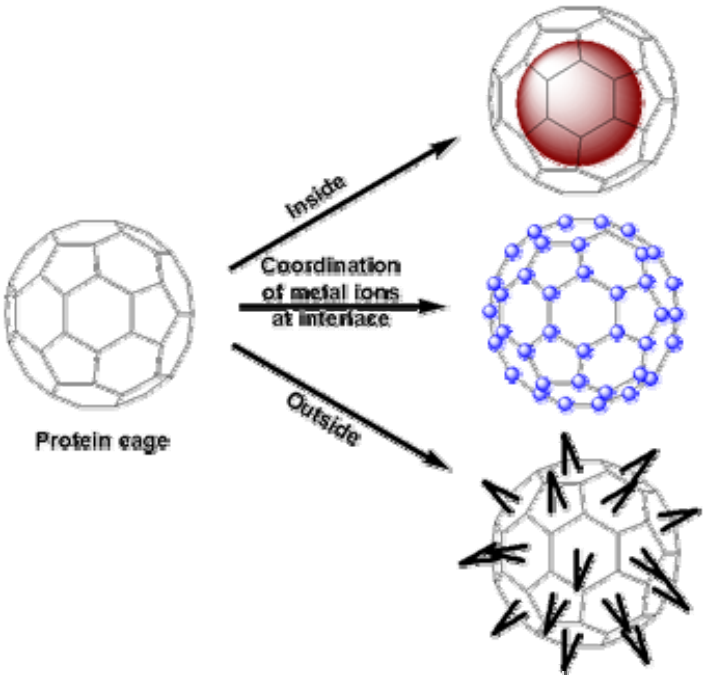

Figure 1.2: Schematic representation of three distinct interfaces present in all protein cage systems; interior, exterior and the interface between subunits.

that have unusual and controllable properties and (2) to probe some of the dynamic properties of protein cages with respect to there ability to bind metal ions at specific metal binding sites and to determine binding affinities. The purpose was to gain a basic scientific understanding and to move into a realm of functional nano-materials synthesis in the development of protein cage constrained catalytic or magnetic materials and to use the metal binding properties of certain protein cages to probe their ability to be used as paramagnetic MRI contrast agents. Part one of this project has been guided by the hypothesis that all protein cages that have electrostatically distinct interior and exterior surfaces and pores in the protein shell which allow molecular access to the interior surface can be used for size constrained material synthesis. In order to probe hypothesis one multiple protein cage systems were investigated; (1) a homologue to a DNA binding protein from nutrient starved *E. coli* cells (Dps) which was actually isolated from the bacterium *Listeria innocua* (LDps)[33, 34], (2) Cowpea chlorotic mottle virus (CCMV)[35] and (3) a mutant of CCMV which was designed to have a ferritin like function (SubE)[36, 37]. Part two of this project describes the use of fluorescence resonance energy transfer (FRET) to determine the metal binding affinity of two viral protein cages. Understanding the role that metal ions play in a virus will give insight into many processes like viral replication, transmission and assembly, as well as structural transitions in the viral capsid. Furthermore, binding paramagnetic metal ions (Gd^{3+}) at the metal binding sites provide an added functionality of the viral cage for biomedical applications like magnetic resonance imaging. Hypothesis two was investigated using two different systems, CCMV (Figure 1.1C) [38, 39]and Cucumber mosaic virus (CMV) (Figure 1.1B)[24].

Protein Cage Architectures for Material Synthesis

Ferritin:

When considering protein cages for the size constrained synthesis of hard materials it is first necessary to discuss a model system for protein encapsulated mineral formation. An ideal model for this biomineralization is the iron storage protein ferritin[29]. Ferritin is a spherical protein cage that has been isolated from each of the three domains of life[40, 41]. While the primary amino acid sequence may deviate greatly among ferritins, the class of proteins is related through their strong structural similarity[40]. All ferritins are composed of 24 structurally identical subunits that assemble into a very stable protein cage with octahedral symmetry (Figure 1.3A and B) (PDB structure file 1EIR). The external diameter of the assembled protein cage is 12 nm and it encapsulates a cavity that is 6-8 nm in diameter[40]. Figure 1.3C shows a dimer of protein subunits and each subunit of all known ferritins are related by a four helix bundle motif with a fifth helix (helix E)

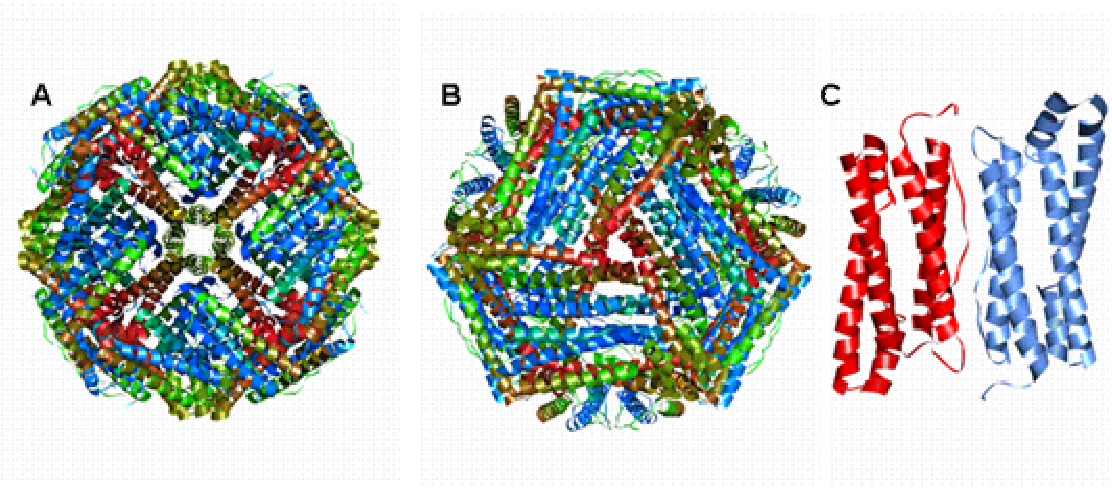

Figure 1.3: Ribbon diagram of mammalian Fn, A. The assembled 24 subunit protein centering on four fold axis, B. Assembled 24 subunit protein down three fold axis, C. A dimer of protein subunits arranged antiparrallel making up the two fold axis in the assembled protein cage.

at the C-terminus oriented 60^{o} to the four helix bundle axis and acts as a capping helix (Figure 1.3C)[31, 42, 43]. In the assembled protein this fifth helix comes together to form the four fold axis (Figure 1.3A). Ferritin (Fn) has become a universal term referring to all classes of ferritin molecules though they can be divided into at least four different groups that have been extensively characterized; mammalian Fn (representing two classes of subunits, H-chain and L-chain), plant Fn, bacterial Fn (BFn) which have been isolated from bacteria and are functionally similar to mammalian H-chain Fn, and bacterioferritin (BcFn), which have also been isolated from bacteria, but are different because they have a heme group bound inside the four helix bundle at a stoichiometry of about 0.25-1 heme per subunit[40]. Archael ferritins have been isolated and some characterization has been done by several groups[5, 6] including the Douglas/Young laboratory. These archael ferritins have not yet been thoroughly distinguished from other ferritins, however they may represent their own subclass. In this introduction, ferritin will be discussed as a model system for biomineralization with a focus on mammalian ferritin; other classes of ferritin will only be mentioned when it is relevant to the discussion at hand.

As mentioned previously, mammalian Fn is divided into two classes of subunits that are structurally identical though there is little sequence similarity[42]. These two forms of subunits, H-chain and L-chain, self assemble to form hetero-24mers with relative ratios of each chain being determined by the organ from which the ferritin is isolated. Originally H and L chains were acronyms meaning heart and liver since it was apparent that there was a prevalence of H-chain isolated in Fn from the heart and more L-chain was isolated in Fn from the liver. As it became apparent that this was not a clear

enough distinction then the H and L was renamed for heavy and light chains corresponding to their differences in molecular mass as determined by electrophoretic mobility with molecular masses of 21 and 19 kDa respectively. H-chain ferritin has a conserved enzymatic activity known as the ferroxidase site and is known to catalyze the oxidation of Fe^{2+} more rapidly than L-chain. In the assembled Fn L-chain is known to have a greater degree of negative charge on the interior with clusters of glutamates and aspartates that make up the nucleation site (discussed later).

Iron Toxicity and Necessity: Iron is a necessary component to most biological systems yet it is extremely toxic and is responsible for the formation of damaging reactive oxygen species (ROS)[44, 45]. This paradoxical relationship between iron and oxygen results in the need for maintaining tight regulation of the concentration of labile iron species in the body. Part of the reason why iron has become a necessary component in most biological systems is because of its ability to cycle between Fe^{2+} and Fe^{3+}, which makes it a valuable part of electron transfer in enzymes and many functional proteins.

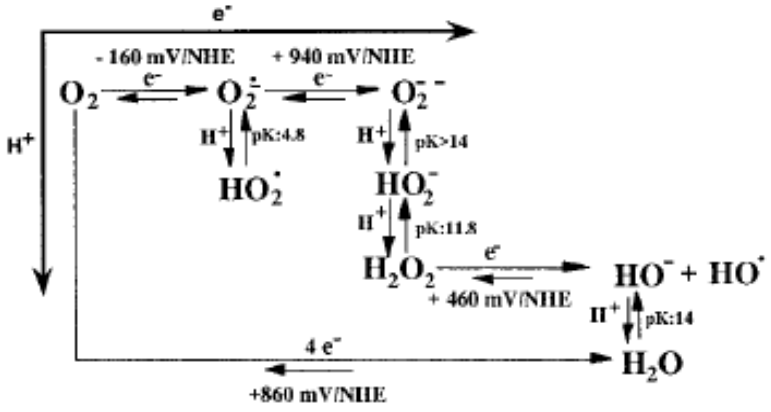

Figure 1.4: Reaction schematic of oxygen with pKs and reduction potentials listed [46].

Also, the ligand environment in which the biologically complexed iron finds itself, allows for the selective tuning of the reduction potential to achieve processes that are controllable under physiological conditions[46].

The toxicity of iron is mainly a result of a reaction with hydrogen peroxide to form hydroxyl radicals through the well characterized Fenton reaction as seen in reaction 1.1 [47, 48]:

$$Fe^{2+} + H_2O_2 \longrightarrow Fe^{3+} + OH^- + HO^{\bullet} \qquad (1.1)$$

Hydroxyl radicals are responsible for many harmful reactions with lipid peroxidation, protein oxidation, and DNA oxidative damage being the most studied and characterized[49]. In the iron reaction with molecular O_2 the first components to be produced are both superoxide as well as hydrogen peroxide. Once superoxide (O_2^-) is produced it can actually reduce the oxidized Fe^{3+} back to Fe^{2+} through another one electron transfer that is reversible under biological conditions (Reaction 1.2):

$$Fe^{3+} + O_2^{\cdot -} \rightleftharpoons Fe^{2+} + O_2 \qquad (1.2)$$

Together reactions 1.1 and 1.2 cycle together in what is referred to as the Haber-Weiss cycle[46]. Cu^{1+} is actually more reactive than Fe^{2+} in the Haber-Weiss cycle but since the overall abundance of Fe^{2+} is much greater than Cu^{1+} it is iron that is typically studied in this oxidative stress pathway[49].

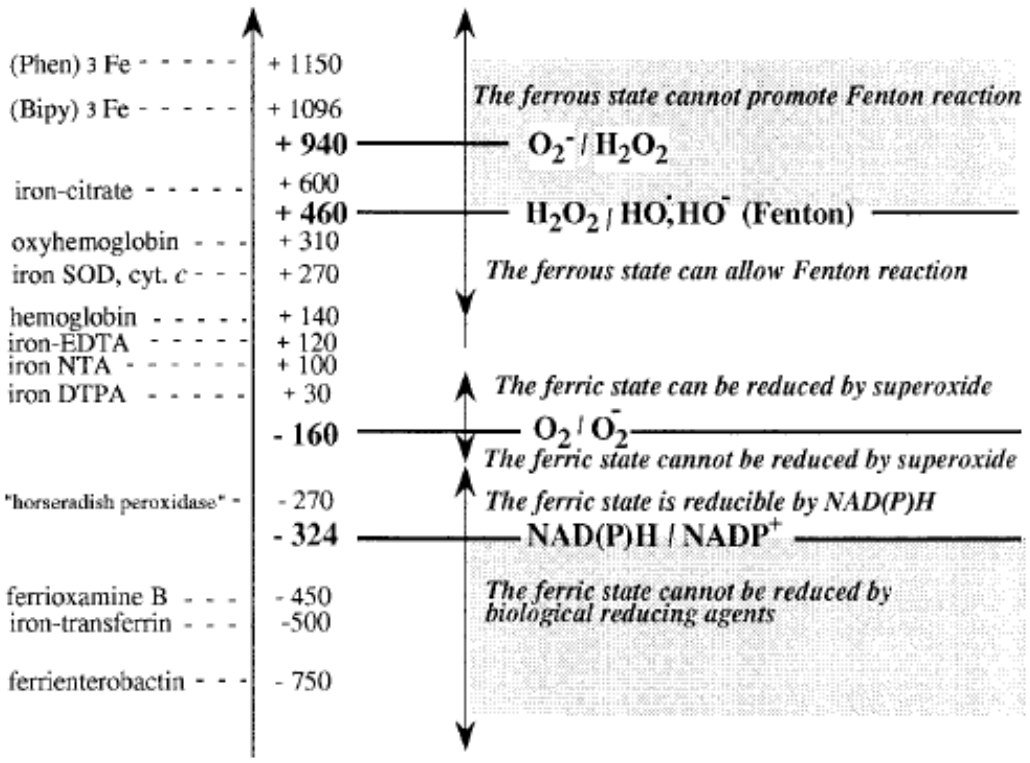

Figure 1.5: Fe^{3+}/Fe^{2+} reduction potentials measured at pH 7 as well as the reducing and oxidizing agents capable of cycling iron under these conditions *in vivo* [46].

It is necessary to address the fact that the redox properties of both iron and oxygen are only relevant under the certain conditions. These conditions are only satisfied at proper pH, concentrations of iron and the various oxygen species, as well as the ligand environment around the iron ion. The diversity of biological molecules allows for activated states of both oxygen and iron to be accessed under physiological conditions. Figure 1.4 outlines the chemistry of oxygen with proton and electron transfers listing pK values and reduction potentials. In each of these oxygen reactions, Fe^{2+} complexes can act as a one electron reducing agent while Fe^{3+} can act as both a reducing and an oxidizing agent. If Fe^{3+} behaves as an oxidizing agent, as in the forward reaction in reaction 1.2, then it regenerates Fe^{2+}. But if it is a reducing agent then high valent and

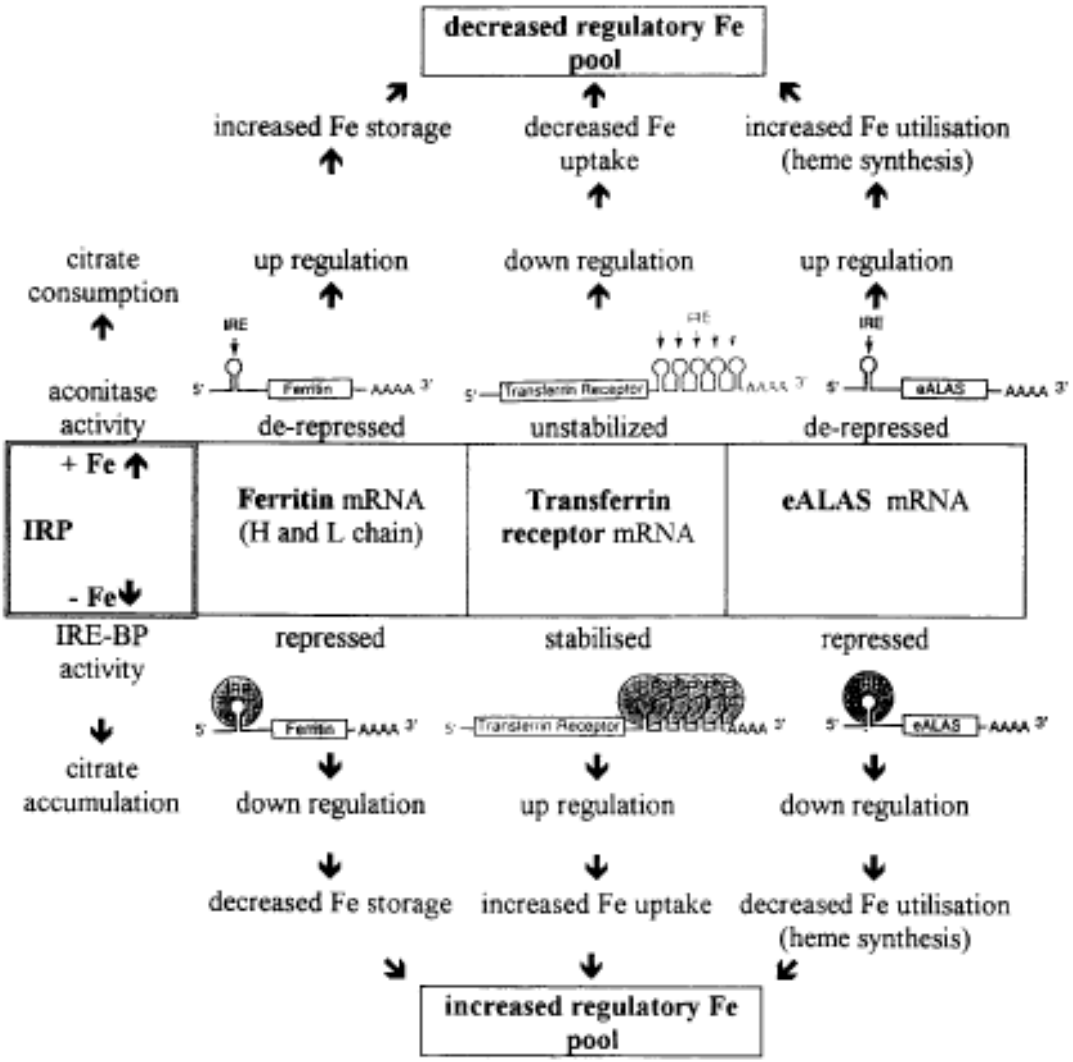

Figure 1.6: Schematic representation of the iron regulation pathway in a rat showing relationship between Fn regulation at the translational level with that of transferrin receptor mRNA and erythroid-specific δ-aminolaevulinic acid synthase (eALAS) mRNA [40].

highly reactive iron species are generated including both Fe^{4+} and Fe^{5+}, which are only typically seen in some enzymatic reaction like those performed by catalases and peroxidases[46]. Figure 1.5 expresses many of the more common reduction potentials of iron and the relevant biological processes that they correspond to; all measured at pH 7[46].

Most of these reactions are relevant to mammalian systems leading to the fluidity of the iron pool.

Iron Distribution *in Vivo*: In a typical human male there is about 3-5 g of iron in the body representing the overall iron pool. Of this iron pool about 2/3 is in circulating red blood cells as hemoglobin, and 15-25 % is stored in Fn or hemosiderin (a denatured and aggregated form of Fn that is largely present in the liver) [40, 50]. The remaining iron is in muscle myoglobin and in cytochromes and iron containing enzymes. Only a few mg is stored in transferrin, but since transferrin is an iron transporter, the actual amount of iron that is exchanged through a transferrin pathway is much higher than that[40]. Uncomplexed iron is almost never seen due to the extreme insolubility of any iron species at physiological pH with Fe^{2+} concentrations no more than 10^{-8} M and Fe^{3+} concentrations no greater than 10^{-18} M [51].

The major sites of iron storage are the liver (about one third), spleen, bone marrow, and muscle. There is a much lower concentration of iron present in myoglobin found in the muscle, but it is still a relevant storage site because of its large mass. Only about 1 mg of iron is actually absorbed into the body of a normal healthy adult per day[40]. This last statistic makes it alarming that iron pills are recommended to anyone when most of the iron present in the pills is either insoluble, never gets absorbed, or could partake in the harmful Fenton reaction, though iron overload is very seldom observed.

Ferritin Expression and Regulation: Ferritin regulation is a difficult question that has not yet been completely answered or understood. Detailed discussion about the

regulation of Fn is beyond the scope of this dissertation and many reviews have been written on the subject[40, 50, 52]. Many ferritins are produced in the presence or absence of iron though the addition of ferrous iron will usually increase the production of ferritin. The gene regulation is very different among the domains of life with bacteria and eukarya being the most studied and documented. In *E. coli*, for example, the two forms of ferritin that are expressed are controlled by two different mechanisms. The bacterial ferritin BFR is upregulated in stationary phase while the nonheme containing FTN remains constant throughout growth. Both BFR and FTN are upregulated in E. coli upon addition of iron, but BFR is upregulated based on some indirect interaction with ferric uptake regulator (FUR)[40, 53].

In mammalian systems it is generally accepted that both H and L chains of Fn is controlled at the translational level through a series of steps associated with a section of the ferritin mRNA called the iron responsive element (IRE). The IRE is part of an untranslated region (UTR) and is responsible for binding the iron regulatory protein (IRP)[52, 54]. A schematic of mammalian iron homeostasis is shown in figure 1.6[40]. In this figure there is a clear relationship between iron, Fn expression, Transferrin receptor expression and heme biosynthesis through the erythoid-specific δ-aminolaevulinic acid synthase (eALAS) expression. When iron concentration is low the IRP binds to the IRE and Fn regulation and eALAS are repressed, but transferrin receptor is upregulated. When iron concentration is high (due to the excess of transferrin receptor) then IRE releases the IRP and Fn and eALAS is de-repressed. This represents one way that ferritin biosynthesis is controlled however it is not a complete representation. There are several

responses that can cause for the upregulation of Fn at the cellular level, many of which do not involve iron concentration, these include chemically induced inflammation, cellular differentiation, or other chemical stresses like insulin and arsenite[40, 55]. The cellular differentiation is probably why many tumor cells are known to express very high levels of Fn, particularly H-chain.

Iron Transport: Iron transport in mammalian systems is well established to be the result of the protein transferrin. To enter the cell, transferrin binds to the transferrin receptor on the exterior of the cell, then enters through receptor mediated endocytosis[40, 56]. Once iron is inside the cell it is unclear whether transferrin directly causes the iron to be deposited into Fn or if this goes on by some other means. There is some evidence that transferrin can interact directly with Fn however this may involve small iron chelating molecules like citrate or ATP[52, 57]. There is some relationship between both the transferrin and Fn regulation paths and the cellular citrate metabolism[40]. While most attempts to mineralize apoferritin (AFn) with ferric citrate have failed [58], the Douglas/Young lab has shown that it is possible under certain conditions[59].

Ferritin Mineralization Mechanism: *In vivo* ferritin is responsible for sequestering and storing toxic iron as an innocuous mineral of iron oxide (ferrihydrite) through an overall protein mediated reaction represented in reaction 1.3[60].

$$4Fe^{2+} + O_2 + 6H_2O \longrightarrow 4FeOOH + 8H^+ \qquad (1.3)$$

The actual biological process of iron oxidation and encapsulation is considerably more complex than reaction 1.3 indicates and some of the steps are still controversial; this will be discussed later in this section. In the presence of ferritin, potentially toxic iron is immediately sequestered and stored inside the cavity of the protein cage. The mineralized particles are electron dense and are the approximate dimensions of the interior of the protein cage (5-7 nm diameter) (Figure 1.7A). When iron is allowed to undergo oxidative hydrolysis *in vitro* with no Fn protein present an uncontrolled

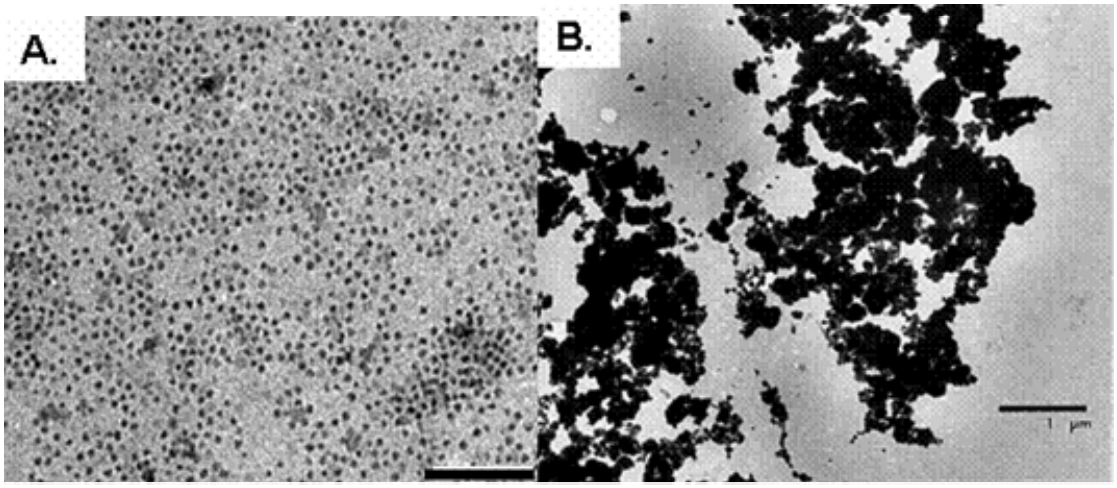

Figure 1.7: Unstained TEM of A. Native cow spleen Fn (scalebar = 100 nm) and B. Protein free iron oxide precipitate (scalebar = 1000 nm).

homogeneous mineralization results in precipitation of iron oxide in multiple forms depending on the conditions in which this precipitation is allowed to occur. But under biological conditions (25-37^{o}C, pH 6-7.5) typically a particular mineral phase of iron oxide, either lepidocrocite (γ-FeO(OH)) or Goethite (α-FeO(OH)), will be formed[61] (Figure 1.7B).

The mechanism by which iron is incorporated into Fn *in vitro* changes depending on the stoichiometry of iron added to the Fn, but the overall process can be summarized by iron entering through a pore in the Fn shell (probably the hydrophilic pore around the three fold axis (Fig 1.2B)), then binding to a catalytic site found in the H-chain subunit called the ferroxidase site where it is oxidized (mostly by molecular O_2). The oxidized iron is then bound as a diiron complex on the interior of the cage where it forms the nucleus of a mineral, the mineral nucleus is then autocatalytic forming a ferrihydrite mineral that is constrained by the size of the Fn protein cage. Each of these processes will be discussed in greater detail.

Iron Entry: Most groups consider the iron entry pathway to be the hydrophilic three-fold axis. There is some doubt to this since some bacterial and plant ferritins

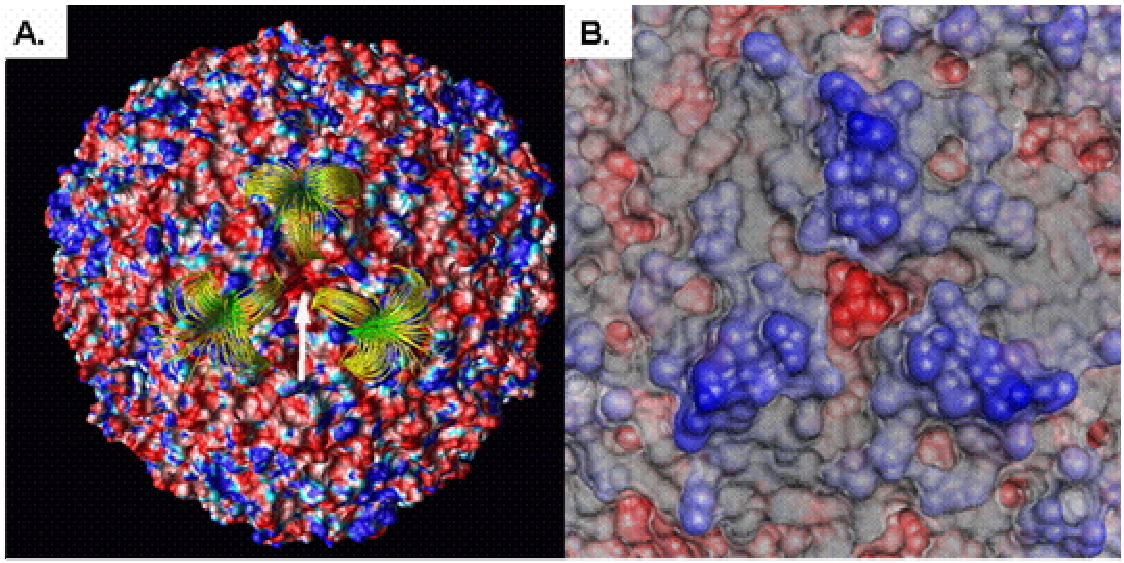

Figure 1.8: Representation of the hydrophillic pore at the three fold axis, A. Electrostatic gradient lines showing a funnel like shape, B. Chimera electrostatic surface image of three fold pore (red corresponds to areas of negative charge, blue to areas of positive charge).

actually have hydrophobic residues lining the three fold axis[40], but there is also a lot of support for this axis to be the main pore of iron entry[62, 63]. There are multiple residues along the three-fold channel that are conserved in eukaryotes, these are D131 and E134. Part of the evidence for the three-fold channel being the main iron entry pathway comes from metal binding assays where some metals (Cd^{2+}, Zn^{2+} and Tb^{3+}) have been shown to bind in this channel[31, 42]. The electrostatic character of recombinant human H-chain Fn has been calculated and along the three-fold channel there is an electrostatic gradient that acts as a sort of funnel that guides cations toward the interior cavity[62] (Figure 1.8). Figure 1.8A shows this funnel like electrostatic gradient while figure 1.8B shows a zoomed in electrostatic surface around the three-fold channel. The size of this three fold channel is somewhat dynamic however it has been shown by EPR spin label studies to be at least 7-9 Å[64]. Douglas and Ripoll have also determined that once the iron is inside the three-fold channel, there is direct electrostatic guidance to the ferroxidase site.

Ferroxidase Activity: In the H-chain subunit of mammalian Fn there is an enzymatic site which directs the oxidation of Fe^{2+} to Fe^{3+} called the ferroxidase site. Once iron enters the protein cage it is bound first to the ferroxidase site. The ferroxidase site binds two irons with nearly equal affinity and there appears to be a binding cooperativity. The amino acids that make up this enzymatic activity consist of E27, Y34, E62, E107 and Q141 with E62 acting as a bridging ligand (Figure 1.9A)[65]. After there are two irons bound at the site, molecular oxygen can bind to the diiron center and oxidize both Fe^{2+} ions to form a μ-1,2-peroxo-diferric center, which decays to a μ-oxo-diferric complex[66] (Figure 1.9B). When the bound Fe^{2+} are oxidized by molecular O_2

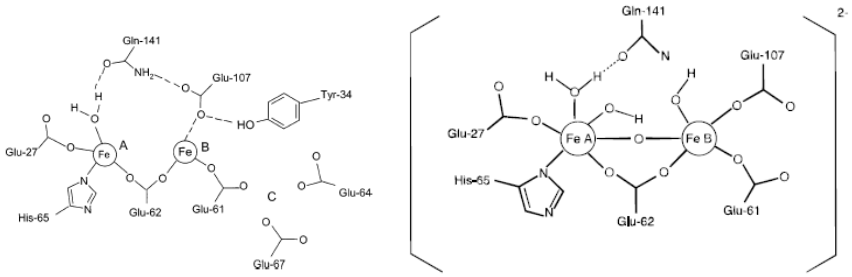

Figure 1.9: A. Ferroxidase site with two Fe^{2+} bound by amino acids E27, Y34, E62, H65, E107, and Q141, B. Ferroxidase site after the two Fe^{2+} ions have been oxidized by O_2 and the complex is degraded to the μ-oxo-diferric complex of H-chain Fn.

they form an intermediate μ-peroxo-complex, which degrades to a μ-oxo-diferric complex with the release of H_2O_2.

Nucleation: After forming, the diferric complex is released from the ferroxidase site to a cluster of negatively charged amino acids present in both H- and L-chain subunits called the nucleation site[61, 67, 68]. The iron complex binds to this cluster of negative charge as an FeO(OH) mineral nucleus. Once formed, growth at the nucleus is autocatalytic at causing the further oxidation and deposition of more iron at this nucleation site. At an iron stoichiometry of 50 Fe/Fn cage or greater this nucleation and heterogeneous mineralization takes over as the kinetically dominant process of mineralization.

Summary of Reaction Mechanism: These processes can be summarized through a series of reactions which eventually results in the formation of an iron oxide core. These are summarized by reactions 1.4-1.8

$$\mathrm{Pr} + 2Fe^{2+} \longrightarrow \mathrm{Pr}-[Fe_2]^{4+} \qquad (1.4)$$

$$\mathrm{Pr}-[Fe_2]^{4+} + O_2 \longrightarrow \mathrm{Pr}-[Fe_2^{4+}O_2]^{4+} \qquad (1.5)$$

$$\mathrm{Pr}-[Fe_2^{4+}O_2]^{4+} \longrightarrow \mathrm{Pr}-[Fe_2^{6+}O_2^{2-}]^{4+} \qquad (1.6)$$

$$\mathrm{Pr}-[Fe_2^{6+}O_2^{2-}]^{4+} + H_2O \longrightarrow \mathrm{Pr}-[Fe_2O]^{4+} + H_2O_2 \quad (1.7)$$

$$\mathrm{Pr}-[Fe_2O]^{4+} + H_2O \longrightarrow \mathrm{Pr}+ 2FeOOH_{(core)} + 2H^+ \quad (1.8)$$

In this scheme Pr is the protein and the charge is balanced by the presence of either hydroxide or negative charge on the protein. Reaction 1.4 demonstrates initial binding of two Fe^{2+} to the protein cage, reaction 1.5 is the binding of molecular O_2 to form a dioxygen complex, reaction 1.6 is the formation of the peroxo intermediate followed by degradation to the μ-oxobridged complex, finally reaction 1.8 is the release of the iron complex from the ferroxidase site to form the FeOOH core at the nucleation site[61]. This mechanism leads to the overall reaction presented in the balanced reaction 1.3.

There is experimental evidence for each of the complexes presented in this reaction scheme ranging from UV-Vis spectroscopy to EPR and Mossbauer spectroscopy. There is however a strong discrepancy in the initial stages of the mechanism, particularly the release of H_2O_2 in the ferroxidase reaction (1.7). Most people consider Fn to be a necessary component in preventing Fenton type chemistry from happening, yet reaction 1.7 would actually cause for Fenton reactions to occur. This question has recently been addressed by Zhao *et al.* where an EPR spin trapping experiment verified that the presence of H-chain ferritin in particular caused for the attenuation of hydroxyl radical and greatly reduces the oxidative stress[69]. Their research indicates that upon forming H_2O_2, this strong oxidant immediately reacts with more iron at the core by bypassing the ferroxidase activity using reaction 1.9.

$$2Fe^{2+} + H_2O_2 + 2H_2O \longrightarrow 2Fe(O)OH_{(core)} + 4H^+ \quad (1.9)$$

Since Fn has been verified to protect DNA and other biomolecules from oxidative stress in short term studies[40], it seems clear to think that there is some other reaction going on that at least removes peroxide as it is formed.

The reactions presented thus far only represent part of the story for biomineralization inside the Fn protein cage. Apart from discussing the electrostatic guidance of ions down the three-fold channel there has been little emphasis placed on the

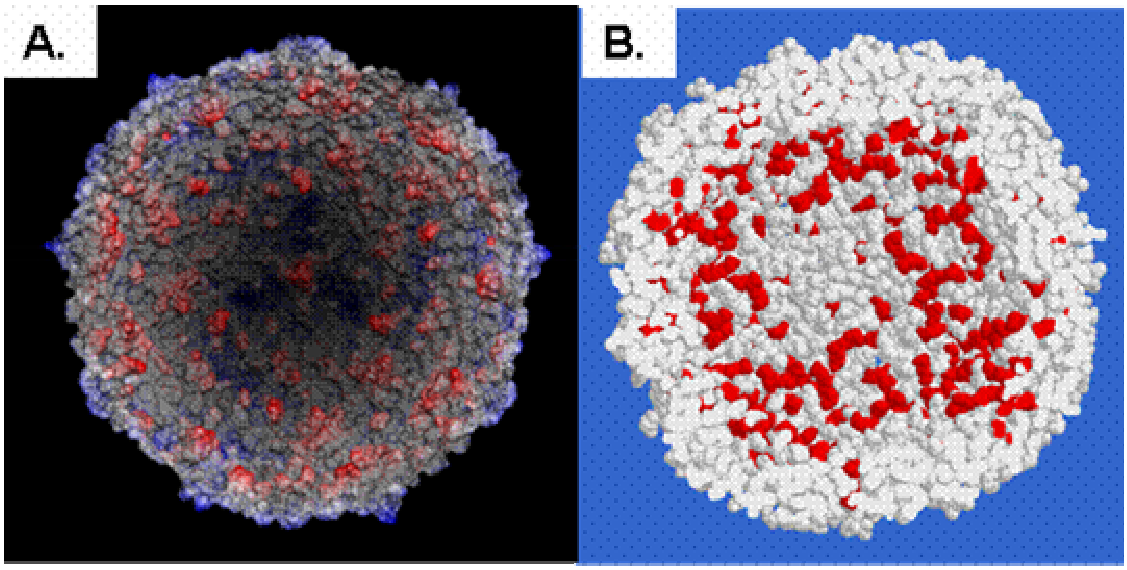

Figure 1.10: A. Chimera electrostatic surface image of the interior of mammalian Fn, B. Space filling model with amino acids responsible for nucleation shown in red.

overall electrochemical directionality of mineralization inside Fn. It is clear that reaction 1.4-1.9 all occur inside mammalian H-chain homo and hetero polymers. However, the extremely high density of negative charge specifically on the interior surface of Fn cause for this to be a robust platform for electrostatically controlling mineralization. This is apparent in L-chain homopolymers of Fn, which while they have no known ferroxidase like activity, are still able to catalyze the size constrained mineralization of iron oxide inside the assembled protein cage. This is due to the negative charge density of the

interior surface (Figure 1.10), which serves to aggregate cations along the interior surface of the protein cage resulting in a supersaturation, oxidation, and mineralization of the final iron oxide product. It is known that binding Fe^{2+} to carboxyl species greatly lowers the reduction potential making oxidation a favorable process. The nucleation site of L-chain Fn consists of residues E57, E60, E61, E64 and E67 all of which reside on or close to the interior surface of the protein making coordination of Fe^{2+} by carboxylic acid groups likely[70]. Under biological conditions the mineral ferrihydrite is the only phase of iron oxide that is isolated in the native protein. However, Fn has been used for the synthesis of other iron oxides as well as non-native cobalt oxides (CoOOH, Co_3O_4)[71-73], manganese oxides (Mn_2O_3, Mn_3O_4)[74-77] as well as a wide range of other materials[78-84]. The fact that *in vitro* mineralization is not specific to iron, as would be implied by the ferroxidase activity, indicates that the electrostatic character of the interior surface of the protein cage plays an important role in mineralization and that *in vivo* factors such as metal ion availability might dominate activity.

The electrostatic contribution to mineralization can be approximated using Gouy-Chapman theory of charged interfaces[85]. Briefly, Gouy-Chapman theory states that the

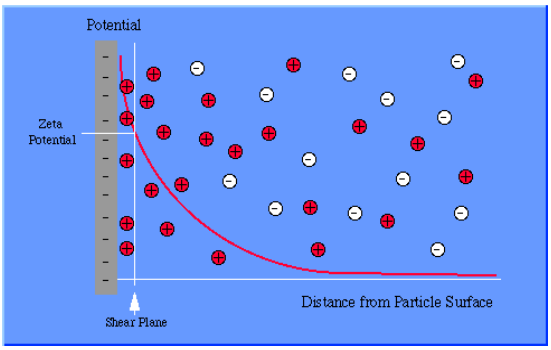

Figure 1.11: Gouy-Chapman model for charged interfaces, the surface is negatively charge, the concentration of positively charged ions in solution at the surface is greater than in the bulk; the red line corresponds to the exponential drop in concentration of positively charged ions.

charge on a surface influences the ion distribution of electrolyte close to that surface through Coulombic interactions (Figure 1.11)[86]. Gouy-Chapman theory is an extension of Helmholtz models of charged surfaces with the one distinction that in Gouy-Chapman theory there is not a rigid layer of positive charge at a negatively charged surface, but rather this layer is diffuse and fluid allowing for solvent effects to be taken into account. In this diffuse double layer modle there is some incorporation of negative ions around the cations that are aggregated at the negatively charged surface[86]. Figure 1.11 shows that the concentration of counterions will aggregate at a charged surface and that the concentration of those ions drops off exponentially with respect to distance from the charged surface. According to this model, at the very negatively charged interior surface of Fn there is a concentration gradient where positively charged ions aggregate in close proximity to this surface. This implies that while Fn does regulate iron concentration through multiple pathways that are largely governed by an enzymatic activity, a purely electrostatic mechanism is probably the mechanism for biomimetic synthesis of non-native materials inside the protein cage Fn. This purely electrostatic model is the primary tenet of hypothesis number one in determining that all protein cages that offer an electrostatically distinct interior and exterior surface along with pores in the protein shell that allow molecular access can be used for materials synthesis under the proper conditions of complimentary electric charge. All of the protein cages represented in figure 1.1 satisfy the requirements offered here and thus validate their use as nano-containers for materials synthesis.

12 Subunit Protein Cage

Background: When *E. coli* is stressed, either by oxidative stress or nutrient starvation, several proteins are upregulated including a multi-subunit protein that has been compared to Fn. This protein is Dps (DNA binding protein from nutrient starved cells) and since its discovery in 1992[87] many other proteins with similar function and

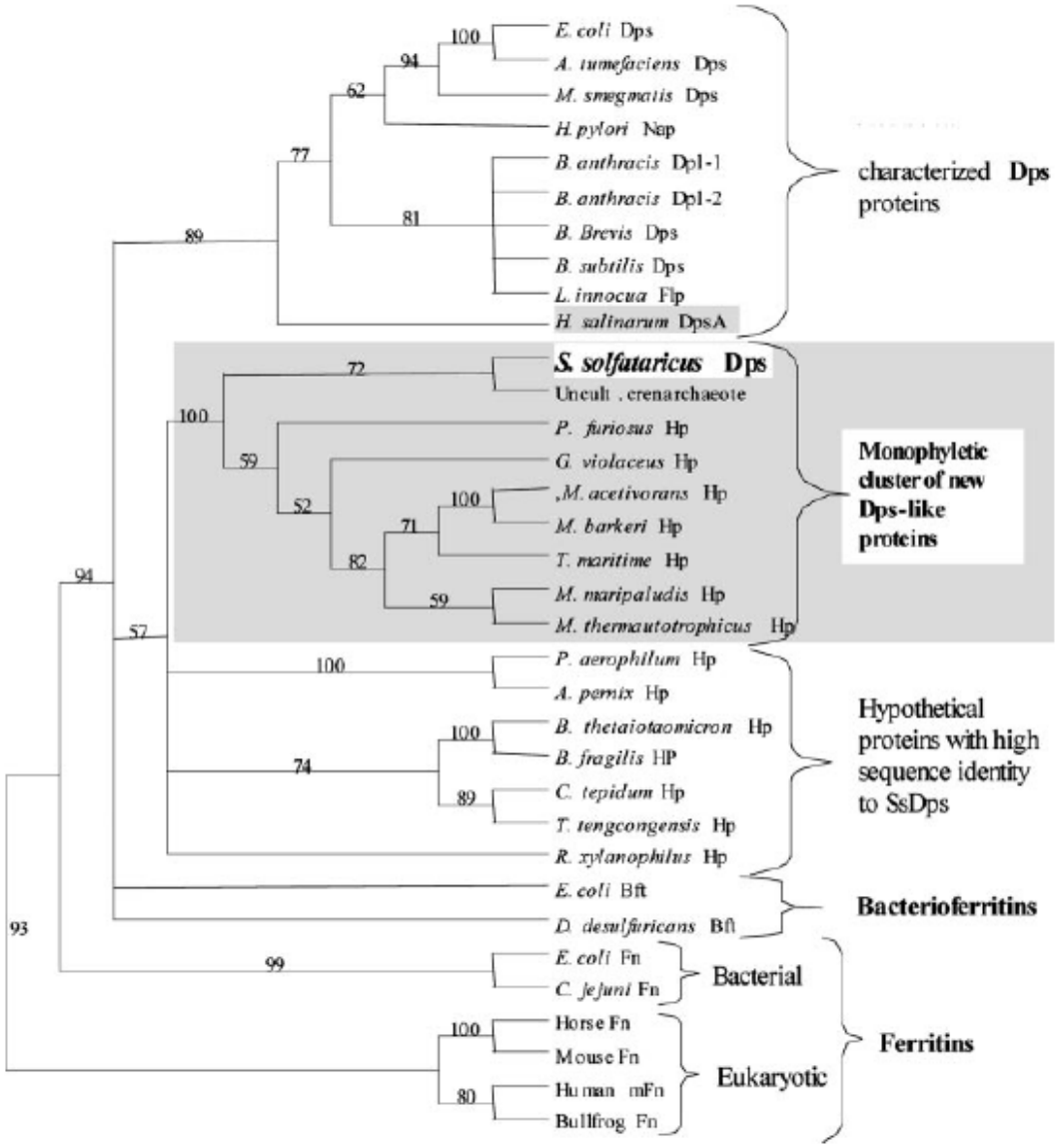

Figure 1.12: Phylogenetic analysis of several members of the ferritin like diiron carboxylate superfamily. The shaded area represents a grouping of protein from the archael domain of life in comparison to Fn and previously characterized Dps proteins [5].

structure have been isolated from both bacteria[30, 88, 89] and archaea[5, 6, 90] and grouped into this Dps family of proteins. One such protein was isolated from the bacterium *Listeria innocua*[30]. This *Listeria innocua* Dps (LDps) was originally considered a ferritin because it was isolated from its host with iron incorporated using the same techniques used to purify Fn (relying on its thermal stability)[45]. It is no longer considered to be a Fn since all Dps proteins discovered have some Fn like activity and have been grouped into a superfamily of proteins which contains Fn called the diiron carboxylates[12, 15]. It is interesting to note that while all Dps proteins have a ferritin-like activity for detoxifying the cell of both iron and H_2O_2, not all Dps proteins have a DNA binding activity as their name implies[45, 88].

There is a clear relationship between Fn and the Dps proteins. Structural and phylogenetic analysis shows a clear relationship between Fn and Dps proteins while also recognizing a split between the two subclasses of diiron carboxylates. Differences among diiron carboxylate proteins were recognized by Ishidaw *et al.* and extended to include several hypothetical and Dps proteins from Archaea by Wiedenheft *et al.* (Figure 1.12)[5, 91]. There are many differences between Dps and Fn that range from expression to primary function. One difference is that Dps is expressed under iron starvation conditions, but upregulated on H_2O_2 stressed conditions. While there is high structural similarity between the two proteins, Dps only assembles into a 12 subunit protein cage with 23 symmetry (Figure 1.13A)[30]. The subunit structural core is still based on a four helix bundle, however instead of a capping helix there is a fifth helix in the loop connecting the B and C helices (Figure 1.13B). Figure 1.13B shows a subunit dimer,

which also contains the metal binding site (still called the ferroxidase site)[8, 12, 92]. The ferroxidase site is a both a similarity between Fn and LDps and a difference, the intersubunit ferroxidase site is a novel place for the metal binding function of Dps. Lastly, another clear distinction between Fn and Dps is that all Dps proteins have a strong preference for H_2O_2 as the oxidant rather than using molecular O_2 [45] in a reaction depicted by reaction 1.10.

$$2Fe^{2+} + H_2O_2 + H_2O \longrightarrow 2FeOOH_{core} + 4H^+ \qquad (1.10)$$

This reaction indicates that the Dps proteins may have a main purpose of removing hydrogen peroxide rather than sequestering Fe^{2+}.

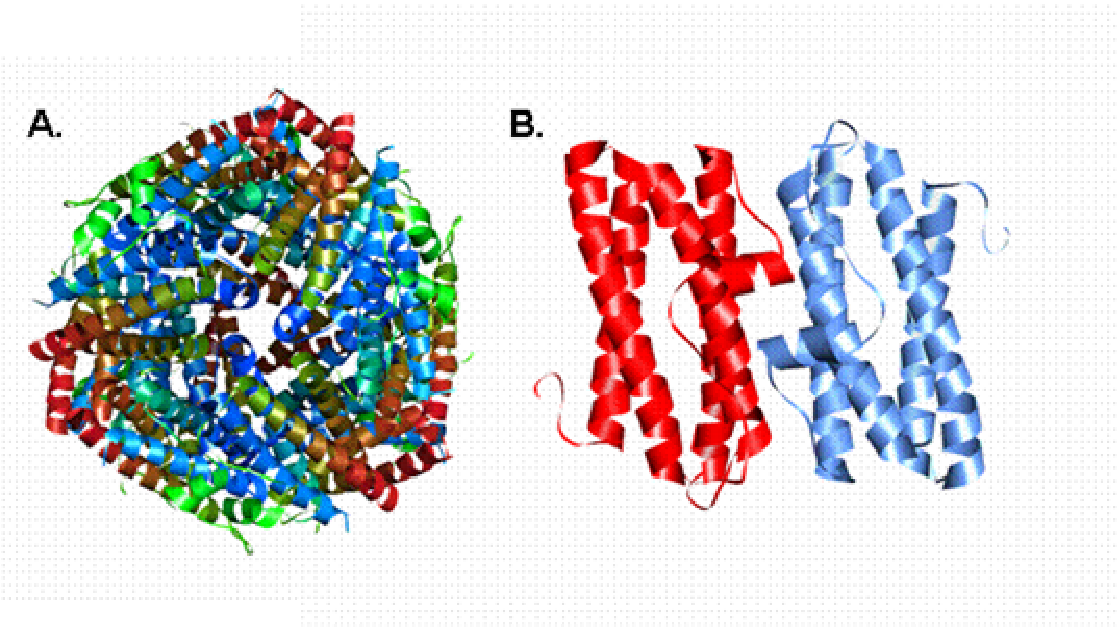

Figure 1.13: A. Ribbon diagram of LDps protein cage, B. Dimer interface between two subunits which contains the ferroxidase active site.

Mineralization Inside LDps: Dps proteins have not been as thoroughly studied as Fn, but have been shown to behave similar to Fn in its assembly and stability.

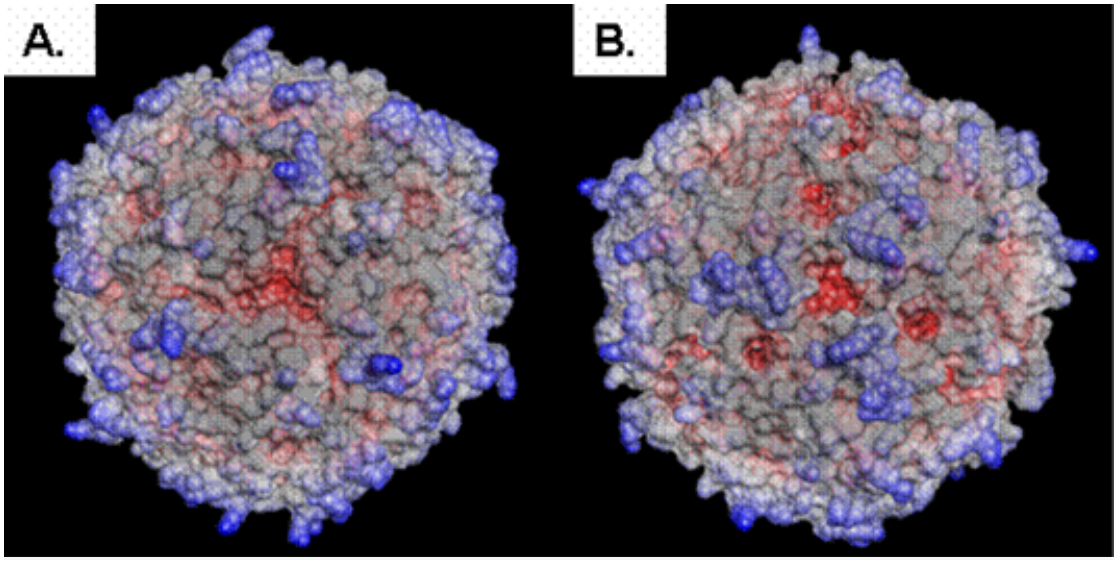

Figure 1.14: Electrostatic surface model visualizing down the two different environments represented by the three fold axis of symmetry, A. Same directional visualization as seen in the ribbon diagram of figure 1.13A.

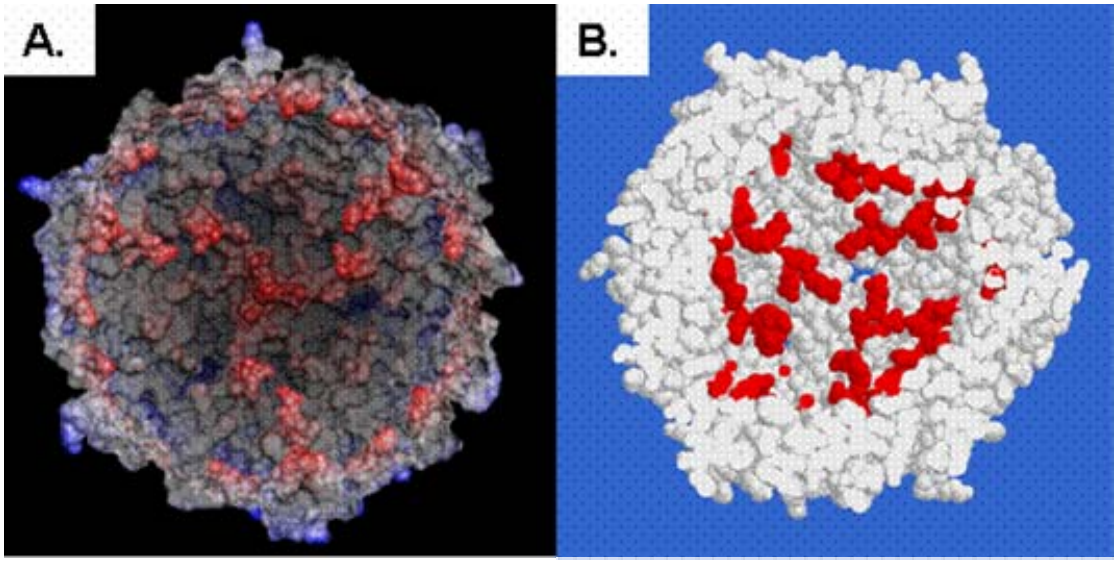

Figure 1.15: A. Chimera electrostatic surface image of the interior of LDps, B. Space filling model of the interior of LDps with glutamates and aspartates highlighted in red.

Furthermore, LDps has been shown to have a ferroxidase site that is at the dimer interface between the small fifth helix of two adjacent protein subunits[12]. Given the structural information on Dps; can LDps satisfy hypothesis number one in acting as a size constraining reaction vessel for materials synthesis?

Figure 1.13A shows a ribbon diagram of LDps looking down a pore in the three fold axis. This pore is lined with hydrophilic amino acids that can give molecular access of ions to the interior surface (Figure 1.14). Figure 1.14 shows an electrostatic surface determined by (Chimera (UCSF)) looking down the two environments of the three-fold channel, figure 1.14A corresponds to the pore seen in figure 1.13A. The size of this pore is on the same order as the three fold pore of Fn, about 8 Å[93]. Once the cation is inside LDps there is a very negatively charged interior surface similar to Fn on which nucleation can take place (Figure 1.15). Figure 1.15A shows the electrostatic surface of the interior of LDps while figure 1.15B labels the actual amino acids that can be responsible for nucleation of a mineral core in red.

LDps was isolated from its host with an iron oxide core indicating that it has a Fn like function. Furthermore, in isolating the protein from an *E. coli* expression system a process similar to that of Fn purification is undertaken. This involves heating *E. coli* cells up to 70^{o}C for 10 minutes before the final SEC purification indicating that there is a Fn like stability. In addition, the architecture suggests an ideal environment for constrained material synthesis. The use of LDps for size constrained synthesis of non-native minerals will be discussed in detail in chapter 2.

Viruses and Virus Like Particles

Introduction: Viruses and virus like particles (VLPs) are exquisite examples of supramolecular assembly that represents the ordering of subunits into a precisely defined, stable protein cage. All viruses function by using a protein or protein/lipid capsid to transport their nucleic acid to and between appropriate host cells. Under the proper conditions, early in its replication cycle, the virus will typically release its nucleic acid cargo (sometimes by completely disassembling), initializing viral gene expression. The simple fact that viruses store nucleic acid through non-covalent interactions implies that the virus has electrostatically distinct interior and exterior surfaces.

In introducing viruses as protein cage systems, it is first necessary to discuss viral capsid symmetry. All viruses are assembled from multiple copies of a limited number of subunits that can come together into several different quatenary structures including filaments, rods, spindles, helices, and spherical capsids with icosahedral symmetry[94].

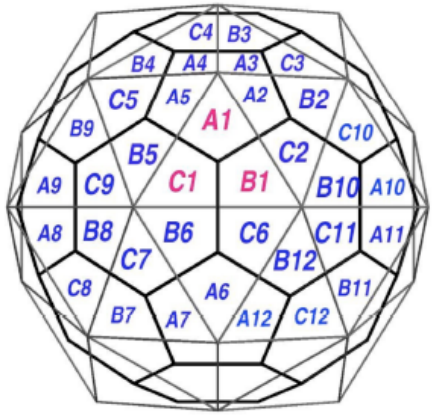

Figure 1.16: Truncated icosahedron defined by T=3 symmetry.

The last two virus types (helical and icosahedral) represent the largest portion of viruses[95], examples of which can be found in hosts from all domains of life. The highly symmetrical assembly of subunits is favorable because it allows for a maximum number of subunit contacts while assembling into a capsid that is capable of encapsulating the genome large enough to encode capsid protein[96].

An icosahedron is defined a structure with 20 triangular faces and 12 vertices resulting in 60 identical points like a Buckminster fullerene (C_{60}). In Buckminster fullerenes each carbon atom is identical though the environment in which it sits is related by 532 symmetry. A spherical virus that assembles into a true icosahedron could be built from 60 copies of an identical coat protein subunit, however this severely limits the size of the genome that can be packaged inside the assembled virion[96] and very few functional viruses actually form T=1 viruses. Most spherical viruses are assembled based into quasi-icosahedra, which simply means that they are assembled from supramolecular structures that are integer multiples of 60 where the integer is also the triangulation (T) number. This means that a T number of 3 would define a virus composed of 180 identical subunits (Figure 1.16). There are formulae that can be used to calculate T numbers based on the structure of the assembled virus, which involves measuring the number of virus subunits present in a single triangular face of the quasi-icosahedron, but at its foundation and in its earliest definition, the T number is defined as the integer multiple of 60 that defines a quasi-icosahedron[95]. T=3 viruses tend to be the most common however structures have been solved for viruses with extremely high T numbers using cryo electron microscopy image reconstruction (Figure 1.17). Figure 1.17

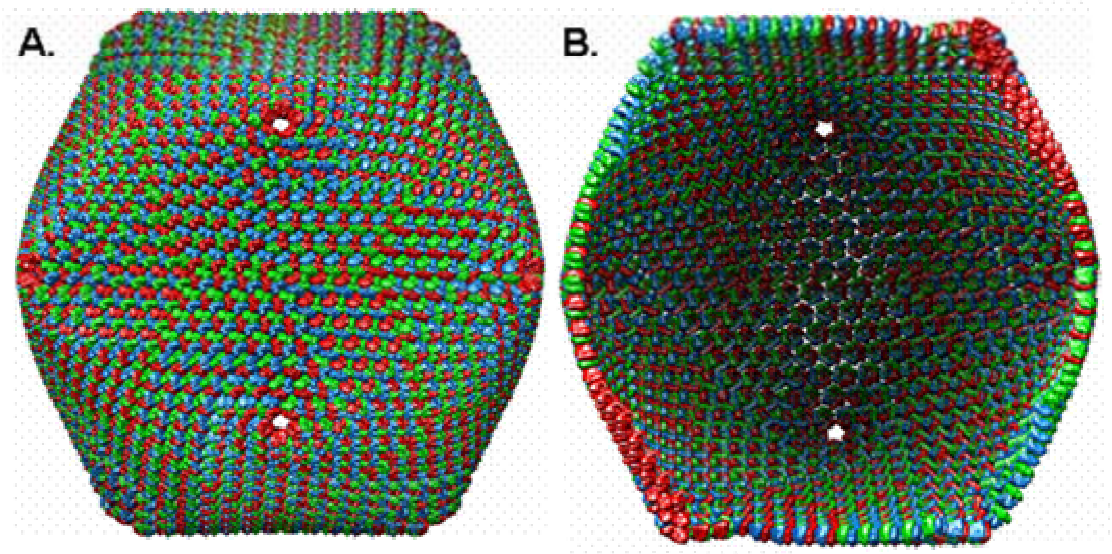

Figure 1.17: A. Exterior and B. Interior views of PBCV1 (Reddy *et al.*).

represents the A. exterior and B. interior of an assembled virus PBCV1 composed of 5040 subunits [32].

CCMV as a Protein Cage: Cowpea chlorotic mottle virus (CCMV) is a plant virus that assembles from 180 identical subunits into a T=3 quasi-icosahedral viral capsid (Figure 1.18). In the quasi-icosahedral arrangement, each subunit, though chemically identical, is present in three slightly different chemical environments designated A, B, and C, which correspond to the colors in figure 1.18 as blue, green, and red respectively. CCMV is a member of the *Bromoviridae*, which are distinguished from other classes of plant viruses by encapsulating a tripartite genome that consists of three unique, single-stranded, positive-sense RNA molecules that are encapsulated independently of each other in separate viral capsids[97]. The total size of the genome is about 8.2 kb and is composed of RNA 1 (3.2 kb), RNA 2 (2.9 kb), and RNA 3 (2.1 kb), included in the viral capsid encapsulating RNA 3 there is a small fourth strand of RNA (RNA-4)[98].

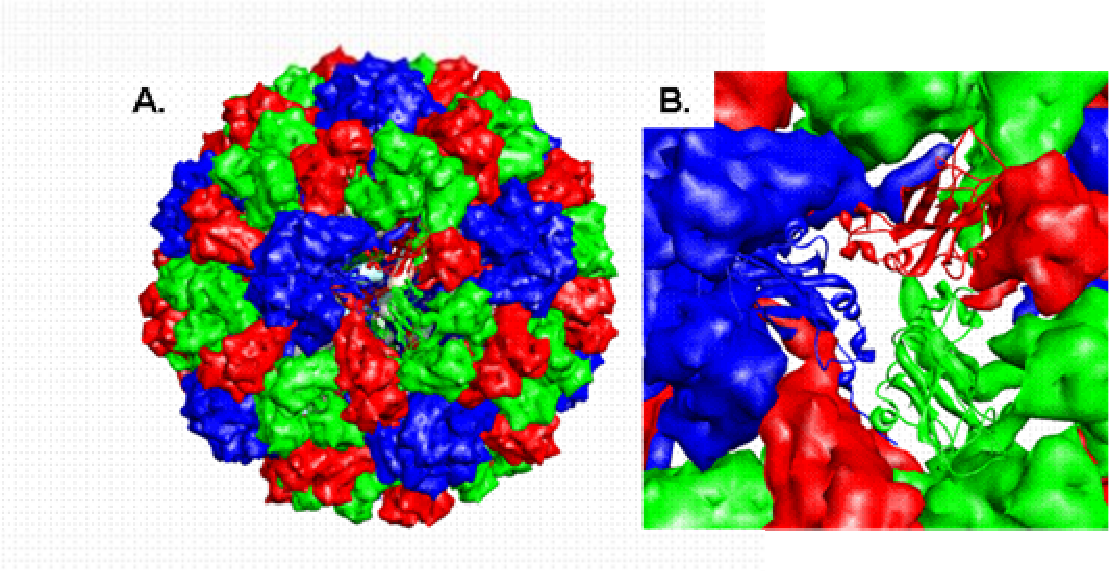

Figure 1.18: A. Surface model of CCMV with the three subunits that make up the asymmetric unit shown as ribbons, B. Zooming in on the three distinct subunits that make up the asymmetric unit.

It has been shown that the very positively charged N-terminus of the virus is responsible for encapsulating the viral nucleic acid. If the first 25 amino acids (containing several positively charged lysine and arginine amino acids) are deleted from the viral capsid, it is not capable of encapsulating viral nucleic acid. However, if only the first seven amino acids (not containing positive charge) are deleted, the virus still forms infectious particles that has symptoms of the native virus infection[97]. This indicates that the very positively charged portion of amino acids is located specifically on the interior of the assembled viral capsid.

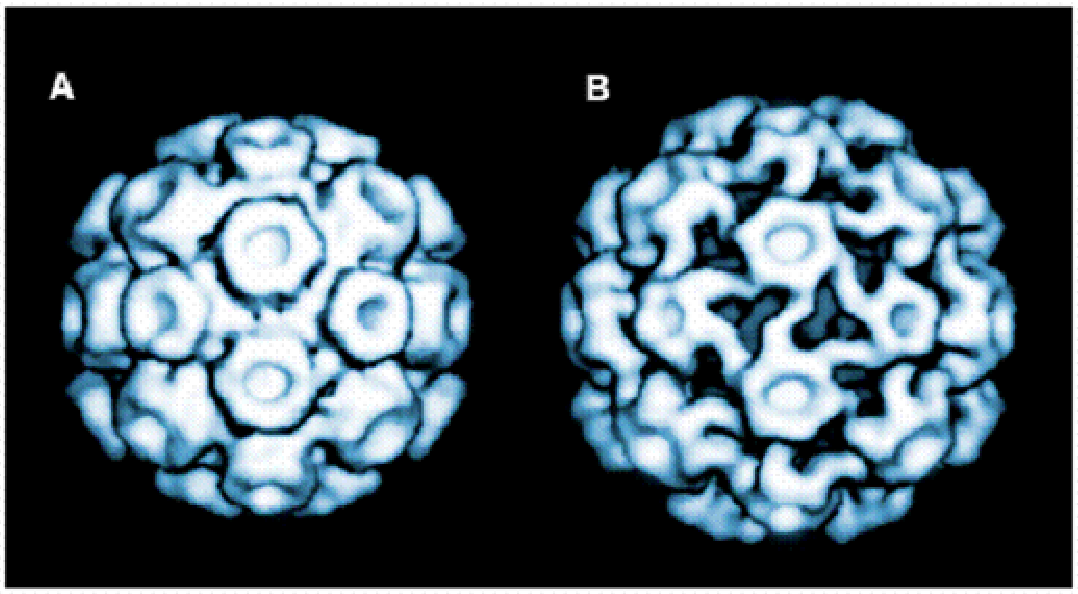

Figure 1.19: 3D cryo electron microscopy reconstruction of A. closed form of CCMV and B. open (swollen) form of CCMV.

CCMV was the first icosahedral virus structure that was reassembled *in vitro* to form empty VLPs with no nucleic acid[99, 100]. Furthermore, the quatenary structure of CCMV is dynamic and undergoes a pH and metal ion dependent swelling of a pore at the quasi-three fold axis which allows molecular access to the interior surface of the protein cage. This process is known as gating or swelling where there is an increase in the overall dimensions of the exterior of the protein cage by about 10 %[25, 101] (Figure 1.19). Though the surface charge on the inside of the assembled virus is the opposite of Fn empty CCMV represents a protein cage with an electrostatically distinct interior surface and with pores in the protean capsid that allow molecular access making it a candidate for materials synthesis. This was first demonstrated in 1998 when purified empty viral capsids were mineralized selectively acquiring polyoxometallate precursors along the interior surface of the protein cage at a high pH (under swollen conditions), then the pH was lowered causing an acid catalyzed polymerization to form a crystalline phase

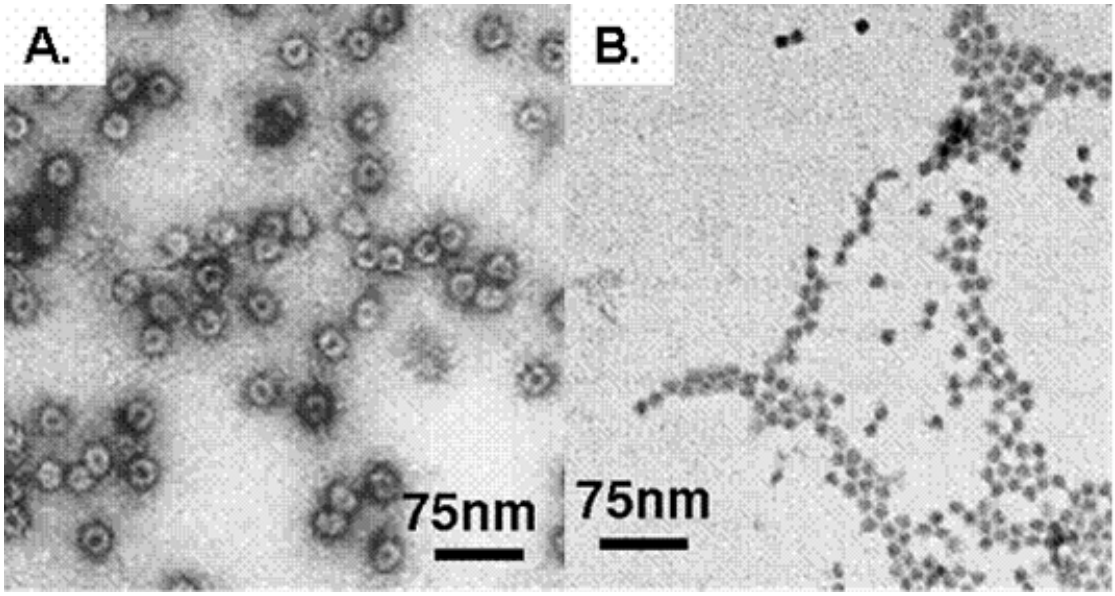

Figure 1.20: A. Stained and B. Unstained image of CCMV mineralized with polyoxotungstate.

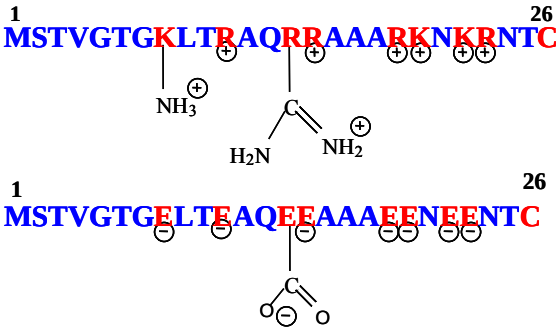

Figure 1.21: N-termini for wtCCMV vs subE mutant.

polyoxotungstate and polyoxovanadate[35] (Figure 1.20). Since this time, more materials have been synthesized inside wtCCMV and mutant CCMV which will be discussed in greater detail in chapter 4.

Redesigning CCMV to Make a Fn Mimic: CCMV is among the first plant viruses that have been prepared from a heterologous expression system (*Pichia pastoris*)[102]. This expression system was necessary in order to perform genetic modifications on CCMV that would make it a non-infectious virus. The desire was to induce a Fn like

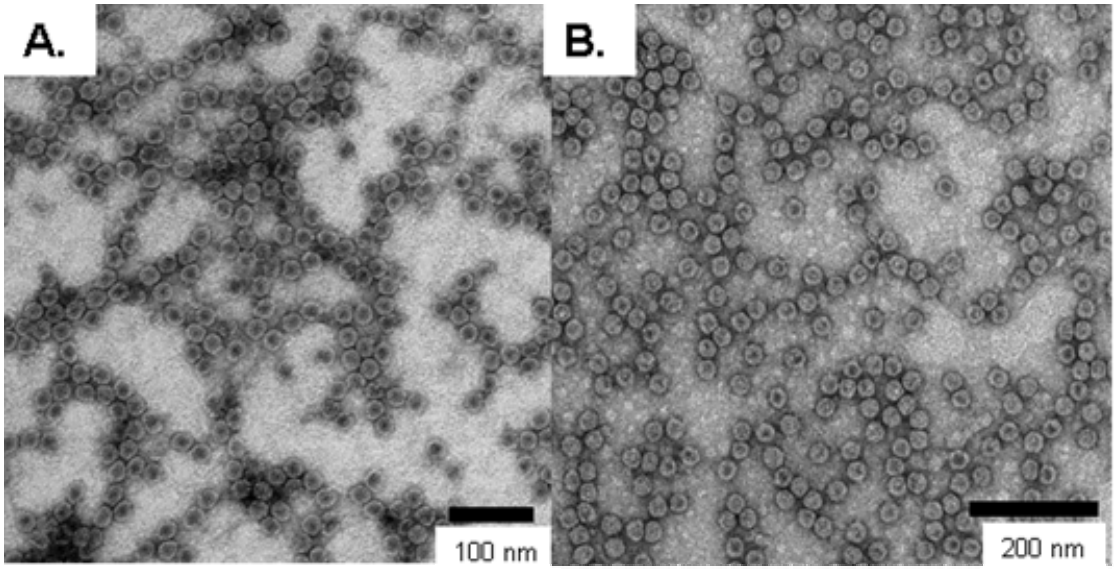

Figure 1.22: Negative stain TEM comparison between the structures of A. wtCCMV and B. SubE.

activity to the assembled virion by completely changing the interior surface charge. PCR mediated site directed mutagenesis was employed in order to change nine positively charged amino acids along the N-terminus to glutamic acid as described in chapter 3 (Figure 1.21). This mutant, termed subE, assembles into a VLP that is morphologically indistinguishable from wild type CCMV as determined by negatively stained TEM (Figure 1.22)[36]. SubE, with its altered interior surface charge, has been shown to act as a Fn mimic for mineralization of iron oxide nano-particles (Figure 1.23). Figure 1.23 shows an image of the mineral core prepared inside SubE as measured by high angle annular dark field imaging, the yellow corresponds specifically to iron while the blue is the image contribution by nitrogen surrounding the iron mineral, 1.23B is a cartoon representation of 1.23A. In addition, SubE has served as a mineralization platform for the formation of ferrimagnetic mineral and will be discussed in chapter 3.

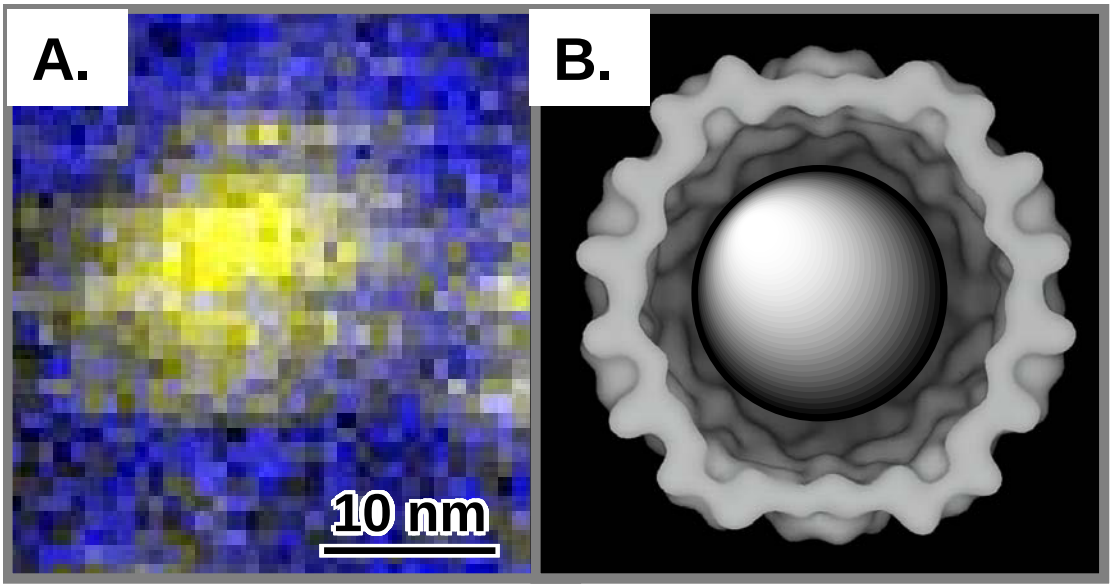

Figure 1.23: A. High angle annular dark field element specific image map showing signal from Fe (Yellow) and N (Blue), B. Cryo-schematic of mineral encapsulated.

Dynamics and Metal Binding

Introduction:

In 1996, it was determined that 52% of all the proteins present in the protein databank contain metals (excluding alkali metals)[103]. Metal binding often plays a role in supramolecular assembly as well as function and stabilization. Many viruses require metal ions to be present in order to drive the assembly of the viral coat protein. Southern bean mosaic virus (SBMV), for instance, requires the presence of relatively high concentrations of both magnesium and calcium in order to assemble the viral capsid and has been isolated from infected southern bean plants coordinating approximately 110-130 Mg^{2+} ions and 75-100 Ca^{2+} ions[104]. If these ions are removed the viral capsid is considerably more susceptible to protease degradation. In this case, among many others, the bound Mg^{2+} and Ca^{2+} plays an essential role in stabilizing protein-protein interactions

that form the SBMV capsid[105]. Two other viruses for which metal binding may play a pivotal role are CCMV and Cucumber mosaic virus (CMV)[24, 25].

It was already mentioned that CCMV undergoes a pH and metal ion dependent structural transition known as gating. When metal ions are released at neutral pH the protein cage swells and becomes destabilized, which may be a mode of inducing the release of nucleic acid and thus infecting the plant cell. CMV has been shown to contain a metal binding site along the exterior surface of the protein[106]. It was found that mutations to this metal binding site caused the virus to be nontransmissible through its aphid vector that typically transfers infection from plant host to plant host[107-110]. Determining the metal binding affinity of these viruses for the biologically relevant metal ions (Ca^{2+}) is necessary to understanding the role that metals play in virus function and structure as discussed in chapters six and seven. In these chapters the technique of fluorescence resonance energy transfer (FRET) is discussed[38, 39].

FRET is an invaluable technique that has been used for determining binding affinities as well as distance relationships between FRET donors and acceptors in several biological systems. The intensity of the energy transfer between FRET donor and acceptor is dependent on the distance between the two molecules. This technique requires an overlap between the emission spectrum of the donor molecule with the absorbance spectrum of the acceptor molecule. These parameters can be satisfied by two organic dyes with complementary spectra or between an organic dye and inorganic ions[111, 112].

Research Goals

In this chapter protein cages were introduced as viable reaction vessels for both size constrained materials synthesis and as platforms on which to measure a metal binding affinity. There is a large focus on Fn because of its biological importance and since it behaves as a model system for the use of protein cages as a platform for materials synthesis as well as metal binding. Two hypotheses were presented, (1), can any protein cage with an electrostatically distinct interior and exterior surface and containing pores in the protein cage shell be used for size constrained material synthesis, and (2), can metal binding affinity be studied to determine a biological role for certain metal ions concentrations with two specific virus systems.

In the next four chapters several protein cage systems will be discussed in detail along with some materials synthesized specifically on the interior of some of these protein cages. The last two chapters focus on a biological role that metal binding may play on the function and dynamics of two virus systems. The goal of this dissertation research is to explore the feasibility of using stable protein cages for material synthesis and to understand the processes involved in biomimetic synthesis so that other protein cages can be either chemically or genetically modified in order to design more functional protein cage platforms. Another goal is to understand the role of metal binding in certain virus systems and possibly draw some relationship between binding affinity and viral infection or transmission. In all of these systems chemical and genetic modifications can be readily performed in order to design functionality. These modifications continue to be expanded by others in the group to include targeted drug delivery, development of MRI

contrast agents, and other magnetic materials synthesis, photocatalytic materials synthesis, as well as starting a path toward developing a keen understanding of oxidative stress and its role on some biological systems.

CONSTRAINED SYNTHESIS OF METAL OXIDES INSIDE A 12-SUBUNIT PROTEIN CAGE FROM *LISTERIA INNOCUA*

Introduction

Nanomaterials are of interest because of their size dependent behavior, which makes their properties vastly different from both bulk and molecular materials. Typically, large scale materials preparation is done by top-down approaches, which usually involve preparing thin films (through sputtering, vapor or thermal deposition) and then milling the film to the desired particulate size by lithography[113-116]. However this is a difficult process when working on the scale of 4-30 nm. Synthesis of this size regime from a bottom-up approach begins with molecular precursors; which form the larger nano-material has been achieved by a number of methods but still lacks properties like biocompatibility and environmentally friendly synthesis[117-121]. Among these techniques are sonochemical and reverse micelle synthesis, both of which involve organic solvents and a complete coating of the material with a passivating layer. The group of Hyeon *et al.* has prepared on large scale exquisite nano-particles with less than 10% size distribution in this size range[118]. Other groups have also prepared materials with control of the shape (cubes, spheres, triangles, shells)[122, 123]. Among the nano-materials that are most interesting are those with magnetic or catalytic properties because they have direct application in technology, imaging and medicine. Toward this end many groups have focused on spinel phase ferrites, particularly magnetite (Fe_3O_4), maghemite (γ-Fe_2O_3), and cobalt dicobalt oxide (Co_3O_4) as well as other metal oxides[117-119, 122, 123].

In biomineralization, organic based molecules self-assemble to provide a scaffold for the controlled aggregation and assembly of inorganic materials[124]. The interaction between organic and inorganic phases relies in part on a molecular recognition between the two phases. A model for this relationship is that of the protein cage ferritin[75, 76, 80]. The host-guest relationship between ferritin and the encapsulated iron oxide mineral is based primarily on a complementary electrostatic interaction. Charged interfaces play important roles in defining electrostatically distinct environments within the protein cage architecture that direct different aspects of the biomineralization reaction. The interaction can be summarized by applying Guoy-Chapman theory of charged surface interfaces, which states that along a charged surface there is a high concentration of counterions which drops off exponentially with distance until reaching bulk concentration[85]. In the

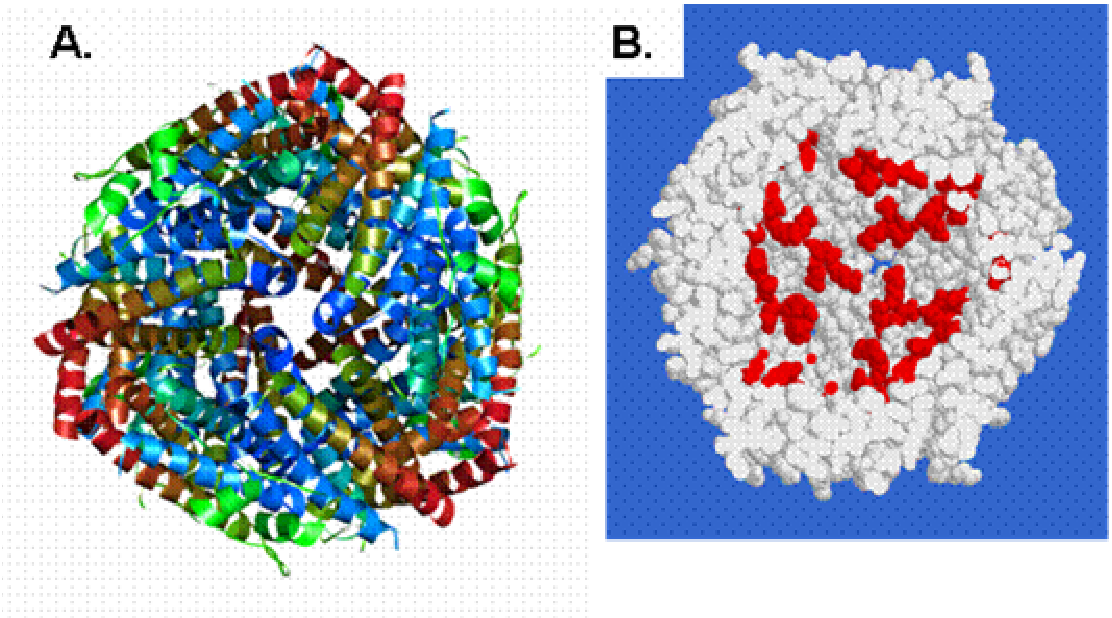

Figure 2.1: A. Ribbon diagram of LDps looking down the three fold channel (pdb file: 1qgh), B. Space filling representation showing the negatively charged residues on the interior of LDps.

case of ferritin these interactions happen specifically on the interior of the protein cage. A minimal set of criteria for spatially constrained nano-particle synthesis includes a cage-like architecture; which serves both as an electrostatically distinct surface and as a size constraining reaction vessel, and pores in the protein cage shell that allow for molecules to access the inside of the cage. In principle, any protein cage with a highly charged interior surface with pores that allow molecular access to the inside of the protein could act as a constrained reaction vessel for directing mineral formation in aqueous solution.

The Dps cage-like protein from the bacteria *Listeria innocua* (LDps) is composed of 12 identical 18 kDa subunits, which self assemble into an empty cage having 23 symmetry (Figure 2.1). Dps has acquired its name (DNA binding protein from nutrient starved cells) because it has been shown in many cases to bind to DNA as a mode of DNA protection. Most of the Dps proteins that have been discovered play some role in preventing oxidative stress by preventing the formation of reactive oxygen species ($HO^{\cdot}$) caused by the Fenton reaction[45]. LDps is part of a larger class of proteins that have been recognized as a "diiron carboxylate super family", which includes ferritins[5, 30]. However the structure of LDps is atypical compared to the majority of structurally characterized ferritins which assemble from 24 subunits to give a cage with outer diameter of 12 nm and an inner diameter of 8 nm (as discussed in chapter 1). The atomic resolution structure of LDps has been solved and structural analysis indicates that LDps satisfies both the requirements of protein cage constrained biomineralization, having clusters of negatively charged amino acids on the interior surface defining an electrostatically distinct interior environment, and also several pores (0.8 nm) at subunit

interfaces in the protein cage which allow molecular access to the interior[30]. The empty protein cage has an outer diameter of 8.5 nm and an inner diameter of 5 nm (Figure 2.1). Thus, LDps has a cavity a little more than half the diameter of the 24 subunit ferritin protein cage.

The electrostatically distinct nature of the interior of LDps, allows for the use of LDps as a Fn like protein cage that can be used for the size constrained synthesis of metal oxides. Here the synthesis and characterization of three different transition metal oxides prepared specifically on the interior of the stable LDps protein cage will be presented. The three mineral systems that are discussed include the ferrimagnetic mineral maghemite (γ-Fe_2O_3)[33], and two cobalt oxides (CoOOH, Co_3O_4)[34]. These materials were selected because of their interesting properties. γ-Fe_2O_3 was also prepared in Fn and a Fn homologue allowing the size dependent properties of this mineral system to be probed as discussed in chapter 5.

Materials and Methods

Materials:

All chemicals were purchased from Sigma-Aldrich and used as received with no further purification. All water used was purified through a Nanopure system to 18MΩ resistivity.

Listeria Dps Expression and Purification

Protein Cloning and Expression: Primers were designed to amplify the coding region of the Dps from *Listeria innocua* (Genbank Accession AJ244014). The forward primer (5' ggaagata**catatg**aaaacaatcaactcag 3') included an *Nde*I restriction endonuclease site directly upstream of the start codon for insertion into a pET-30a(+) expression vector (Novagen, Madison, WI). The reverse primer (5' gat**ggatcc**ttattctaatggagcttttcc 3') included the stop codon for the gene and a *Bam*HI site, again for insertion.

Lyophilized *Listeria innocua* bacteria were purchased from ATCC (#51742). Genomic DNA was extracted from the cells by mechanical lysis of the cells and a routine phenol/chloroform/isoamyl alcohol extraction followed by an ethanol precipitation [33]. The DNA pellet was resuspended in 50µl of sterile ddH_2O and 1µl was used in a standard polymerase chain reaction (PCR) with the primers above to amplify the *Listeria innocua* Dps. The resulting PCR product was digested with *Nde*I and *Bam*HI restriction endonucleases and cleaned up with a Qiaquick PCR purification kit (Qiagen,). This product was ligated into a *Nde*I/*Bam*HI linearized pET30a vector that had been treated with calf-intestinal phosphatase. The ligation was transformed into Xl-2 blue ultracompetent *E. coli* (Stratagene) and screened for the presence of insert. The insert sequence was confirmed by sequencing using Big Dye Termination protocols on an ABI 310 automated capillary sequencer (Applied Biosystems).

The positive DNA was transformed into BL21 *E. coli* (Novagen) for protein expression. Colonies were screened for expression after IPTG induction and analyzed on a Coomassie stained SDS-PAGE gel (Maniatis, et al., 1982). Cultures of *E. coli* were grown, in 1.0L of LB media in the presence of 1µg/mL of the antibiotic kanamycin, to an

optical density (OD_{600nm}) of 0.4 and before protein expression was induced by addition of IPTG. Cells were harvested by centrifugation at 12,000xg for 30 minutes.

Purification: The harvested *E. coli* pellet from 1.0L of culture was suspended in 30mL of lysis buffer (50mM Tris, pH= 8.0). Lysozyme (1mg/ml) and DNAse (1 mg) were added and incubated for 30 minutes at room temperature. The suspension was sonicated for 10 min in 30 sec intervals and then centrifuged at 12,000xg for 20 minutes at 4ºC. The supernatant was heated at 70ºC for 10 minutes then cooled rapidly on ice before centrifuging again at 12,000xg for 30 minutes at 4 ^{o} C. The supernatant was then applied to an anion exchange column (Uno-Q or Mono-Q) equilibrated with the Tris buffer (50mM, pH 8.0) and the protein was eluted using a salt gradient (0 to 1.0 M NaCl in 50mM Tris, pH 8.0). Fractions eluting from the anion exchange column were pooled and loaded onto a size exclusion chromatography column (Superose 6) equilibrated with MES buffer (50mM MES, 50mM NaCl, pH 6.5). Elution of the protein was monitored at 280 nm.

Protein concentration was determined by the biuret method, and confirmed by the molar absorbtivity at 280nm of 2.59 x 10^5 $M^{-1} \cdot cm^{-1}$[30].

γ-Fe_2O_3 Mineralization: A solution of LDps (15 mL, 5mg, $2.3x10^{-5}$ mmoles in 0.1 M NaCl) was added to jacketed reaction vessel under N_2 (to maintain an oxygen free environment). The temperature was brought up to 65 ^{o}C by flowing water through the jacketed flask and the pH was brought to 8.5 using 50 mM NaOH (Brinkmann 718

AutoTitrator). For an iron loading-factor of 400 Fe per protein cage, $8.3x10^{-3}$ mmoles of Fe^{2+} was added to 5mg of the protein in 15 mL reaction volume. Deaerated solutions of $Fe(NH_4)_2(SO_4)_2 \cdot 6H_2O$ (12.5 mM, 0.727 mLs) and the oxidant, H_2O_2, (12.5/5 mM, 0.727 mLs) were added simultaneously and at a constant rate (0.048 mLs/min) using a syringe pump (Kd Scientific). Solutions of H_2O_2 were freshly prepared and the concentration determined using a permanganate titration [125]. The H^+ generated during the reaction was titrated dynamically with a Brinkmann 718 automatic titrator using 50 mM NaOH. The reaction was considered complete 15 minutes after addition.

Co_3O_4 Mineralization: A solution of LDps (15mL, 5mg, $2.3x10^{-5}$ mmoles in 0.1M NaCl) was added to jacketed reaction vessel under N_2 (to maintain an oxygen free environment). The temperature was brought up to 65°C by flowing water through the jacketed flask and the pH was brought to 8.5 using 50 mM NaOH (Brinkmann 718 AutoTitrator). For a cobalt loading-factor of 400 Co per protein cage, $8.3x10^{-3}$ mmoles of Co^{2+} was added to 5 mg of the protein in 15 mL reaction volume. Deaerated solutions of $Co(NO_3)_2 \cdot 6H_2O$ (12.5 mM, 0.727 mLs) and the oxidant, H_2O_2, (12.5/3 mM, 0.727 mLs) were added simultaneously and at a constant rate (0.048 mLs/min) using a syringe pump (Kd Scientific). Solutions of H_2O_2 were freshly prepared and the concentration determined using a permanganate titration. The H^+ generated during the reaction was titrated dynamically with a Brinkmann 718 automatic titrator using 50 mM NaOH. Metal ion and oxidant solutions were added over various time periods including 1, 5, 10, and 15 minutes, and the reaction was considered complete 15 minutes after addition.

Co(O)OH Mineralization: A solution of the *L. innocua* Dps (15 mL, 5 mg, $2.3x10^{-5}$ mmoles in 0.1 M NaCl) was adjusted to pH 8.5 with 0.05 M NaOH. At room temperature (22ºC) solutions of $Co(NO_3)_2 \cdot 6H_2O$ (12.5 mM, 727 μL, $8.3x10^{-3}$ mmoles) and H_2O_2 (12.5/2 mM 727 μL, $4.15x10^{-3}$ mmol) were added via syringe pump over a 2 hour period. The reaction was run unbuffered at pH 8.5 and the H^+ generated during hydrolysis was titrated dynamically with a Metrohm 718 STAT autotitrator (50 mM NaOH).

Characterization:

Transmission Electron Microscopy (TEM): TEM data was collected on a Leo 912 with omega filter operating at 80keV. Samples were concentrated and transferred into ddi H_2O using microcon ultrafilters (Microcon YM-100) with 100kDa M_w cut-off and transferred to carbon coated copper grids. Samples were imaged stained with 0.8 % uranyl acetate and unstained. Electron diffraction data were collected on these samples and d-spacing calculated and compared to powder diffraction files for γ-Fe_2O_3, Co(O)OH, and Co_3O_4 after calibration of the camera with a Au standard. Electron energy loss spectroscopy (EELS) was measured in order to measure elemental composition of samples and compared to reference spectra in order to measure the presence of cobalt in mineralized samples.

Dynamic Light Scattering (DLS) and Zeta Potential: Dynamic light scattering (DLS) and zeta potential measurements were made on a Brookhaven Instruments *ZetaPals* (phase analysis light scattering) particle size/zeta potential analyzer. DLS was

measured at 90^{o} using a 661 nm diode laser, and the correlation functions were fit using a non-negatively constrained least-squares analysis[126]. Zeta potential was measured by applying a 7.10 V/cm AC field and measuring sample mobility at 25^{o}C. The data were fit using a Smoluchowski data analysis.

Polyacrylamide Gel Electrophoresis (PAGE): PAGE was performed under native non-denaturing conditions using a 5% native polyacrylamide gel. Gels were stained for protein using Coomassie blue and stained for Co using 1-nitroso-naphthol. The 1-nitroso-naphthol stain solution was prepared by making a 25 mM solution of 1-nitroso-naphthol in 1:1 ddi H_2O/MeOH. Staining was performed by incubating the PAGE gel in the stain solution and micro waving for 20 seconds, distaining of the gels involved incubation in a solution of acetic acid and methanol overnight.

Native Agarose Gel Electrophoresis: Agarose gel electrophoresis was performed on magnetite mineralized LDps under non-denaturing conditions using a 1% agarose solution at pH 8.3. LDps and mineralized LDps were run in duplicate on the same gel. The gel was cut in half with one lane of each sample on each half. Half the gel was stained for protein using Coomassie blue and the other half was stained for iron mineral with Prussian blue. The Prussian blue stain solution was prepared by dissolving 1 g of $KFe(CN)_6 \cdot 3H_2O$ in 50 mLs of ddi H_2O, then the solution was acidified to less than pH 2 by the addition of 3 mL of concentrated HCl. Staining the gels was performed by incubating the gels in the stain solution for 30 minutes, followed by incubating in a solution of acetic acid and methanol overnight.

Size Exclusion Chromatography (SEC): SEC was performed on a Biologic Duo-Flow fast protein liquid chromatography system equipped with a quad-tech UV-Vis detector and using a superose 6 (Amersham Pharmacia) size exclusion chromatography column.

UV-Vis Spectroscopy: UV-Vis absorbance data was measured on an Agilent 8453 spectrophotometer equipped with a diode array detector.

Results and Discussion

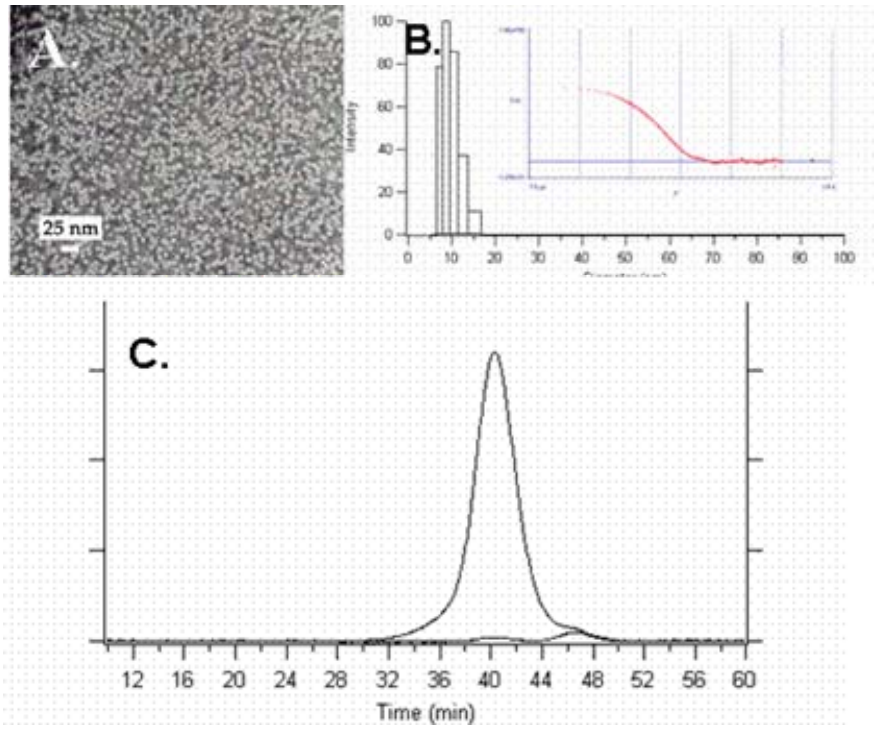

Figure 2.2: A. Negatively stained TEM of LDps, B. DLS of empty LDps indicating a hydrodynamic diameter of 9 nm (inset is the corresponding correlation function), C. SEC of empty LDps measuring absorbance at 280 nm and 350 nm.

Purified LDps provides a unique size constrained reaction environment for the synthesis of Fe-oxide and Co-oxide based nanomaterials. The purified, recombinant protein self-assembled readily into the 8.5 nm cage-like architecture particles indistinguishable from the native protein. This was confirmed by transmission electron microscopy, which revealed protein cages of 8.5 nm diameter (Figure 2.2A). Dynamic light scattering indicated a particle size of 9.2 ±0.4 nm diameter (Figure 2.2B), and elution from size exclusion chromatography (Figure 2.2C) was consistent with a protein of approximately 220kDa. The formation of this monodispersed cage-like architecture is required for the size constrained encapsulation of the metal oxide particles. Typically, the purified Dps cages were treated with aliquots of Fe^{2+} or Co^{2+}, under an atmosphere of N_2, at pH 8.5 and oxidized with H_2O_2 under either room temperature (22ºC) or elevated temperature (65ºC). In the presence of the empty Dps cages, both ambient and high temperature reactions proceeded to form homogeneous brown or olive green solutions for the maghemite or cobalt oxide reactions respectively. In contrast, reactions in the absence of the Dps cages resulted in the bulk precipitation of solids. The lack of precipitate in the reactions containing the Dps cage, and the strong color present in these solutions suggested that the oxidative hydrolysis of Co(II) occurred in a spatially selective manner within the confines of the protein cage.

The mineralization reactions were monitored by several methods including the change in the visible absorbance (Figure 2.3) and by dynamic titration of H^+ generated during the oxidative hydrolysis (Rxn. 1, 2, and 3). When focusing on the Co_3O_4 reaction the rate of Co^{2+} oxidation in the presence of protein was limited by the rate of substrate

addition at both temperatures tested (Figure 2.3 inset). It is clear that after all metal solution is added, the absorbance at 350 nm levels off and no longer changes upon further annealing. The rate of Co^{2+} and oxidant addition (ranging from 0.6-9 μmoles/min) also did not have an impact on the crystalline phase of the material. Titration of H^{+} generated during the reaction revealed an identical behavior, confirming that mineral formation is directly coupled to the oxidative hydrolysis and the rate of reaction is limited by substrate addition.

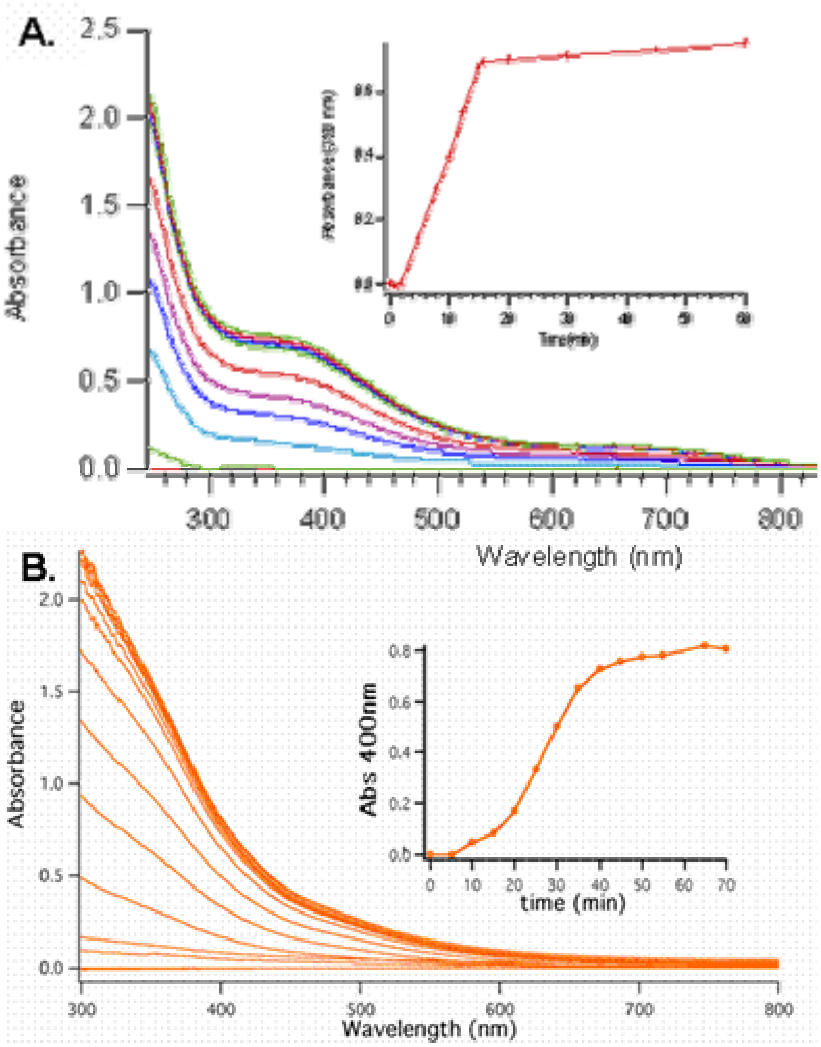

Figure 2.3: Reactions were monitored by UV-Vis spectroscopy over the entire course of reaction, A. Time course for Co_3O_4-LDps, and B. For γ-Fe_2O_3-LDps, the insets are the absorbances at 350 nm and 400 nm respectively.

$$2Fe^{2+} + H_2O_2 \rightarrow Fe_2O_3 + 4H^+ + 2H_2O \quad (2.1)$$

$$3Co^{2+}{}_{(aq)} + H_2O_{2(aq)} + 2H_2O \xrightarrow{65^oC} Co_3O_{4(s)} + 6H^+ \quad (2.2)$$

$$2Co^{2+}{}_{(aq)} + H_2O_{2(aq)} + 2H_2O \xrightarrow{25^oC} 2Co(O)OH_{(s)} + 4H^+{}_{(aq)} \quad (2.3)$$

The products of mineralization were characterized by transmission electron microscopy (TEM), electron diffraction, electron energy loss spectroscopy (EELS), dynamic light scattering (DLS), zeta potential, size exclusion chromatography (SEC), UV/Vis spectroscopy, and native polyacrylamide gel electrophoresis (PAGE). For all characterizations, the mineralized protein was directly compared with the unmineralized protein to assess the spatial selectivity of the mineralization reactions. Together, these characterizations have allowed us to answer the question of whether mineralization occurred on the inside or outside of the protein cage.

All preparations of mineralized Dps protein cages were visualized by TEM after being transferred into ddi H_2O by either dialysis or microcon ultra-concentration. When negatively stained with 0.8 % uranyl acetate the mineralized cages showed an intact LDps protein cage (Figure 2.4A and C). Mineralization of γ-Fe_2O_3 or Co_3O_4 performed at elevated temperatures yielded clear electron dense cores of a size consistent with the interior dimensions of the protein cage were observed (Figure 2.4D). The particle sizes were measured for several hundred particles of both γ-Fe_2O_3 and Co_3O_4 and were found to be quite monodisperse with an average diameter of 3.75 ±0.88 nm for γ-Fe_2O_3 and 4.34 ±0.55 nm for Co_3O_4. This is consistent with the interior dimensions of the Dps cage, which defines an interior cavity of approximately 5 nm diameter. The product of the

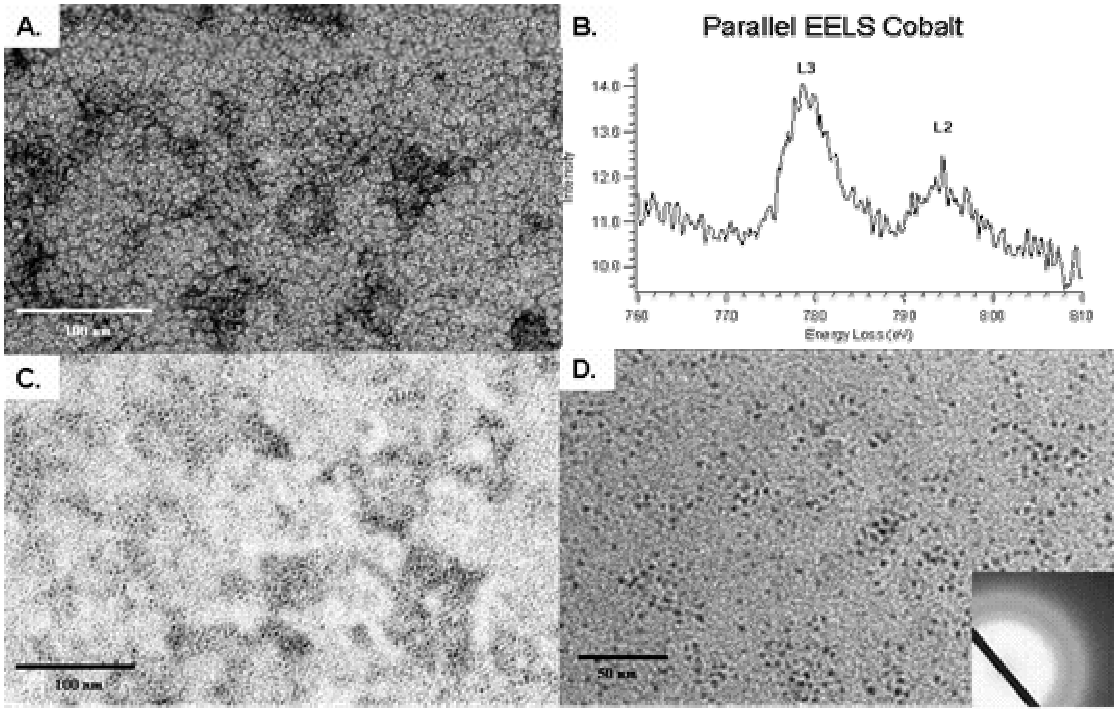

Figure 2.4: A. Negatively stained TEM of Co(O)OH-LDps, B. Electron energy loss spectrum of Co_3O_4-LDps showing the L3 and L2 edges of Cobalt, C. Negatively stained TEM of Co_3O_4-LDps, D. Unstained image of Co_3O_4-LDps with selected area electron diffraction image in the inset.

CoOOH synthesis, performed at room temperature, did not show clear electron dense particles by TEM. The difference between particles synthesized at room temperature syntheses and the 65 ^{o}C syntheses is likely the result of a difference in particle crystallinity, which would result in differences in the Bragg scattering and subsequent contrast between the samples. A higher temperature synthesis is likely to facilitate the removal of structural waters that would be found prevalently in the room temperature synthesis. Selected area diffraction on the two oxides prepared at 65 ^{o}C inside LDps revealed a powder pattern consistent with reported values for the spinel phase of cobalt oxide Co_3O_4 (Table 1) as well as for γ-Fe_2O_3 (ICSD file #39-1346) or Fe_3O_4 (ICSD file #19-0629).[3] It is not surprising that we can not distinguish between γ-Fe_2O_3 and Fe_3O_4 since γ-Fe_2O_3 is a fully oxidized phase of Fe_3O_4 and their crystal structures and d-spacing

measurements are nearly identical. No diffraction pattern could be distinguished from the product of the room temperature synthesis of Co(O)OH. This is similar to the Co(O)OH mineralization of the 24 subunit ferritin under similar conditions which showed very weak diffraction and poorly defined mineral cores[71]. Control reactions, run in the absence of protein cage resulted in the bulk precipitation of black crystals of magnetite or dark green solids of cobalt oxides at either low or high temperature. The bulk precipitate from the reaction at elevated temperature showed a powder diffraction pattern (electron diffraction, d spacings =0.243 nm, 0.203 nm, 0.146 nm) consistent with the spinel phase, Co_3O_4,[127] while that of the low temperature reaction gave a broad diffraction with d spacings of 0.44, 0.24, and 0.182 nm consistent with Co(O)OH, the mineral heterogenite[128]. Electron energy loss spectroscopy was performed on mineralized samples and confirmed the presence of either iron in the γ-Fe_2O_3 synthesis or cobalt in the CoOOH and Co_3O_4 syntheses (Fig. 2.4B) as clearly evidenced by the 786 eV L3,2 absorption for cobalt.

The composite nature of the mineralized protein cage was analyzed by UV/Vis spectroscopy, size exclusion chromatography, dynamic light scattering, and gel electrophoresis. The UV/Vis spectrum of the Co_3O_4 mineralized protein revealed broad absorption centered at 350nm consistent with O–>Co (III) charge transfer band (Figure 2.3A), which is similar to the spectra collected for γ-Fe_2O_3 synthesis (Figure 2.3B). This was in addition to strong absorption at 280nm due to the protein. Size exclusion chromatography (SEC) of both the mineralized and non-mineralized LDps indicated co-elution of the mineral with the protein cage as determined by monitoring for the protein

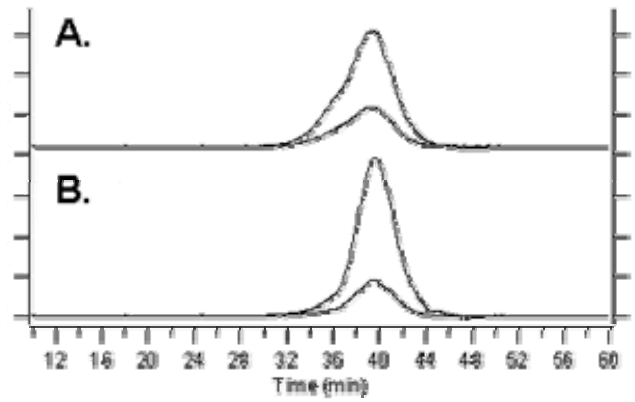

Figure 2.5: SEC of mineralized LDps cages, Elutions monitored at 280 nm for protein and 350 nm for Cobalt oxide mineral. Elution profiles do not change for A. Co(O)OH mineralized LDps and B. Co_3O_4-LDps.

at 280 nm and for the mineral at 350 nm. SEC is sensitive to changes in size, since the mineralized protein cage elutes at the same volume as apo-LDps there does not appear to be any change in size of the mineralized cage, which is consistent to the mineral forming specifically on the interior of the protein cage (Figure 2.5). This co-elution indicates the composite (protein-mineral) nature of the product and also suggests that the overall structure of the protein cage has not been significantly perturbed by the synthesis. Size exclusion chromatography is sensitive to relatively small differences in particle size and this data suggests that the mineral and protein phases are intimately associated. This also indicates that in both reactions the protein cage architecture encapsulates the mineral particle illustrating the spatial selectivity of these reactions.

Dynamic light scattering of the unmineralized Dps indicated a cage of 9.2 ±0.4 nm diameter with a narrow size distribution (Figure 2.2B). After mineralization at either room temperature or elevated temperature there was no significant difference in the observed correlation function. When fit using a nonnegatively constrained least squares

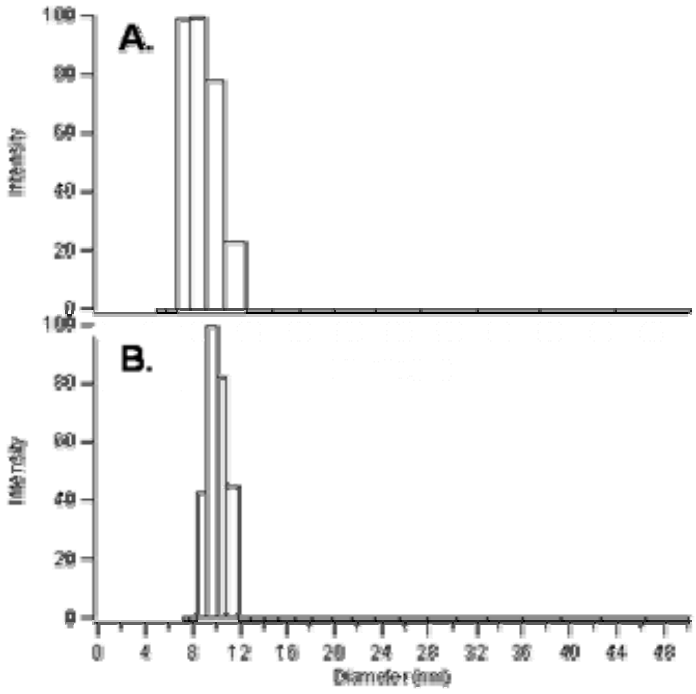

Figure 2.6: DLS for mineralized LDps protein cages, A. Co(O)OH-LDps, B. Co_3O_4-LDps.

(NNLS) analysis, these data indicated a population with mean diameter of 9.3 ± 0.6 nm for the room temperature CoOOH reaction and 9.2 ± 0.8 nm for the Co_3O_4 reaction at elevated temperature (Figure 2.6). γ-Fe_2O_3 synthesized LDps yielded a nearly identical DLS hydrodynamic diameter of 9.2 ± 0.2 nm. Within the limits of this technique, it appears that the diameter of the cage remained unaltered during these reactions suggesting that all mineralization had occurred within the confines of the protein cage.

While both SEC and DLS are sensitive to changes in the size of mineralized

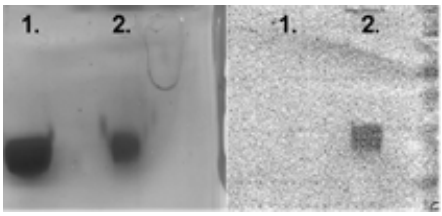

Figure 2.7: Native 0.5% agarose gel electrophoresis lane 1 corresponds to ApoLDps while lane 2 is γ-Fe_2O_3-LDps stained for protein with Coomassie Blue and for iron with Prussian blue.

protein cages, electrophoresis is sensitive to both size and surface charge. In order to determine that upon mineralization there was no measurable change in surface charge electrophoresis and zeta potential measurements were used. For the γ-Fe_2O_3 mineralized LDps an agarose gel was run under non-denaturing conditions. The lanes labeled "1" in figure 2.7 indicate apo-LDps while the lane labeled "2" is the γ-Fe_2O_3 mineralized LDps. Figure 2.7A is the gel stained for protein using Coomassie blue while figure 2.7B is stained for iron using Prussian blue stain. The data indicate that there is a co-migration of the apo-LDps and the γ-Fe_2O_3 mineralized LDps. An electrophoresis experiment was run on both the empty *L. innocua* protein cage and preparations of Co- oxide mineralized protein cages using a 5% polyacrylamide gels under native (non-denaturing) conditions. Gels were selectively stained for Co using 1-nitrosonapthol (25mM in 1:1 H_2O:MeOH)[71] and for protein using Coomassie Blue. Both preparations of the mineralized LDps cages stained with 1-nitrosonapthol and with Coomassie Blue, while the empty protein cage stained only with the Coomassie Blue (Figure 2.8). The co-migration of the assembled LDps cage in both mineralized samples and in the empty LDps cage samples indicated that the mineralized cage remained intact. These electrophoresis data indicate both that the size of the mineralized protein cage does not change and that the exterior surface charge on the protein also does not change during mineralization. This supports our assertion that mineralization occurred in a spatially selective manner and that insignificant amounts of either iron or cobalt deposited on the outer surface of the protein.

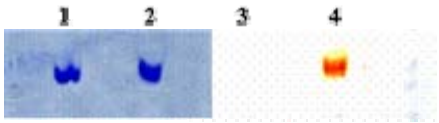

Figure 2.8: Native 5% polyacrylamide gel electrophoresis, Lane 1: ApoLDps stained with Coomassie Blue, Lane 2: Co_3O_4-LDps stained for protein with Coomassie Blue, Lane 3: ApoLDps stained with 1-nitroso-naphthol, and Lane 4: Co_3O_4-LDps stained for cobalt with 1-nitroso-naphthol.

The electrostatic character of the mineralized vs. unmineralized protein cages was additionally measured with a technique called zeta potential by phase analysis light scattering (zetaPALS), which was measured on the Dps before and after cobalt oxide mineralization. ZetaPALS is a light scattering technique where sample is placed in a cuvet and an zeta potential electrode is placed in the solution, a voltage is applied across the electrode with an AC field, and the movement of the particles are measured. Depending on how quickly the particles move and whether the particles move toward the positive electrode or negative electrode gives the analyst an idea of the magnitude of charge on the surface[126]. At pH 8.5, the zeta potential of the unmineralized protein was measured to be – 30 ± 0.6 mV while the Co_3O_4 mineralized Dps had a zeta potential of – 31 ± 0.8 mV. The accuracy of a typical zeta potential measurement is ± 2 %. If cobalt ions were attached to the outside of the protein, a more positive zeta potential would be expected. The fact that the zeta potential is slightly more negative in the mineralized protein may be due to the fact that at pH 8.5, the surface of the mineral has a net negative charge, being above the pH_{zpc} of Co_3O_4, which is reported to be 7.3.

Conclusions

Our data suggest that LDps can be used as a constraining reaction environment for the synthesis of nanomaterials using non-native substrates. Under a range of synthetic

conditions, including elevated temperatures, the protein cage remains unaltered. At both room temperatures and elevated temperatures the oxidation of Co(II) results in mineral particles which are encapsulated within the assembled protein cage as confirmed by several different analytical techniques. Conclusions are never drawn based on a single technique, but rather a suite of techniques must always be applied in order to truly verify the composite nature of the protein encapsulated materials. A single technique may give a false result, for instance, SEC analysis alone may not confirm that the minerals are encacapsulated inside the protein, however TEM verifies the particulate nature of the minerals as fitting inside the protein cage, and electrophoretic mobility confirms that the exterior surface charge is not altered in the reaction.

After confirming the encapsulated nature of the minerals it is possible to speculate that the high degree of spatial compartmentalization is the result of very different electrostatic interfaces present at the interior versus exterior of this protein cage. This confirms the prediction made in chapter one that states that the electrostatic characteristics of the interior surface directs the mineralization of transition metal oxides and oxyhydroxides. This serves to further confirm the model proposed by Gouy-Chapman theory and allows the rationalization of mineral encapsulation based on the aggregation of counter ions at the interior protein interface. This suggests that in the LDps cage, cations, such as Co(II), will aggregate along the charged interior of the protein resulting in a nucleation event by clustering Co(II/III) cations at the interface. It is also possible that this high local concentration at the protein-solution interface lowers the redox potential of Co(II) oxidation and thus facilitates spatially selective oxidation.

As in mammalian ferritin biomineralization, after nucleation, the initially formed crystallite can act as a catalytic site for further oxidative hydrolysis. Therefore, the mineralization process within the protein cage is autocatalytic for mineralization of the mineral oxide and affords a high level of control in the synthesis of size constrained particles.

The synthesized materials are both size and shape constrained by the inner volume of the protein cage. Clearly, small molecules must have access from the bulk to the interior of the protein cage through pores at the subunit interfaces. Oxidative hydrolysis selectively entraps the mineral product within the protein cage. This spatial isolation within the protein cage prevents bulk aggregation of the mineral particles and results in a stable, mono-disperse colloid. These results mimic the reactivity of mammalian ferritin, in which it was previously demonstrated the spatially selective mineralization of amorphous Co(O)OH nano-particles were achieved. The results of LDps mineralization suggest that an increasingly diverse library of protein cages can be used as size constrained reaction templates for many different material syntheses. The current work illustrates this synthetic approach using a uniquely sized cage that approaches the dimensions of large molecules rather than small materials. The LDps allows synthesis of nanomaterials having properties different from larger protein-encapsulated materials with potential application in electronics and catalysis.

SYNTHESIS AND CHARACTERIZATION OF FERRIMAGNETIC NANO-PARTICLES INSIDE A GENETICALLY AND CHEMICALLY MODIFIED VIRAL PROTEIN CAGE

Introduction

Protein cages similar in structure to the iron sequestering protein ferritin have been used for some time as size constrained reaction vessels for the biomimetic synthesis of nano-materials[11, 33, 34, 36, 129-131]. Biomimetic synthesis relies on an interaction between inorganic precursor ions and some biological interface at which mineralization occurs. Phage display techniques have shown that this interaction sometimes relies on very specific amino acids that are required for binding to the inorganic precursor[132-134]. Phage display is a technique used for determine peptide sequences that have a specific interaction with some desired surface. The technique relies on the pIII protein fibers at one end of M13 bacteriophage, these protein fibers are versatile and prone to mutations. When M13 bacteriophage are exposed to a surface, random mutations to pIII proteins will sometime induce an attraction to the mineral surface allowing the isolation of mineral specific peptide chains. The interaction between protein is often not as clear as that presented in phage display, but rather can be a simple electrostatic nature as modeled by Gouy-Chapman theory of charged interfaces as discussed in more detail in chapter 1. When the electrostatic potential is high there is an exponential decay of the concentration of oppositely charged ions with respect to distance from the interface[85]. Protein cages like ferritin, ferritin like proteins, and some spherical viruses, have high charge density

along the interior surface of the protein cage making them ideal candidates for the study of interactions between the protein and inorganic precursor ions. These interactions have been shown previously to facilitate mineralization inside the protein cage in a spatially selective manner. The coat protein of the plant virus, Cowpea chlorotic mottle virus (CCMV) has been used for the size constrained encapsulation of non-native materials[35]. In this chapter a strategy of genetic modification followed by chemical stabilization has been employed to convert the native CCMV into a stable ferritin mimic for the synthesis and characterization of magnetite or maghemite nano-particles.

CCMV is composed of 180 identical 19,500 Da subunits that self assemble into an icosahedral protein cage. The N-terminal of each subunit includes nine positively charged arginine and lysine amino acids that have been modeled to project into the interior of the protein cage. The wild type virus, devoid of its nucleic acid, has previously been used for the size constrained synthesis of polyoxometallate minerals through the interaction of the positively charged N-terminus and the negatively charged precursor ions of the metallate[35]. PCR mediated site-directed mutagenesis was used to change the positively charged amino acids on the N-terminus to negatively charged glutamic acids (E) and thus completely alter the electrostatic character of the interior of CCMV.

The SubE mutant has been shown to be similar to L chain ferritin in function and has been used for the size constrained synthesis of the iron oxide ferrihydrite[36]. Ferrihydrite mineralization was demonstrated as a ‘proof of concept’ for determining that a virus protein can be genetically engineered to induce a completely non-native

functionality to the coat protein. While the mineral ferrihydrite has little material significance, other iron oxides (magnetite and maghemite) are of interest for their magnetic behavior. In this chapter the chemical stabilization of SubE is presented and the synthesis of a ferrimagnetic phase of iron oxide is performed. The materials prepared are characterized for both structural and magnetic properties and the data are presented. The material synthesis involved chemically stabilizing SubE by cross-linking the protein subunits with a bifunctional cross-linker gluteraldehyde. The cross-linked protein is stable to conditions that allow the synthesis of magnetite (Fe_3O_4) or maghemite (γ-Fe_2O_3).

Materials and Methods

Chemicals

Ferrous ammonium sulfate ($Fe(NH_4)_2(SO_4)_2 \cdot 6H_2O$) and 30% hydrogen peroxide as well as all buffers were purchased from Sigma-Aldrich and used as received with filtering each solution prepared. Gluteraldehyde (5 %) was purchased from Amersham Biosciences and used as received. All water used was purified through a nanopure system to 18 MΩ resistivity.

Protein Purification

The SubE coat protein construct was expressed in the *Pichia pastoris* heterologous expression system (Invitrogen) and purified as reported previously[36, 102]. Briefly, *P. pastoris* cells were lysed using glass beads and spun slowly in a centrifuge to remove most of the cells. The supernatant was then spun at 25000 X g to pellet the virus. The virus was resuspended and purified using a 39% (w/v) CsCl density gradient

spinning at 38000 X g and the virus band was collected and dialyzed into acetate buffer (100 mM acetate, 10 mM EDTA pH 4.8). Further purification was accomplished by size exclusion chromatography (SEC) (ÄKTA 900) using a gel filtration column (Amersham Biosciences Superose 6 10/300). Purity was confirmed by SDS-polyacrylamide gel electrophoresis.

Chemical Stabilization of the Protein Cage

SubE was chemically stabilized for the purpose of performing synthesis of ferrimagnetic particles at elevated temperatures and pH by cross-linking the protein subunits using gluteraldehyde. Gluteraldehyde has been shown to form polymers in solution, at neutral pH, these α-β-unsaturated polymers react with surface exposed amines nearly irreversibly [135, 136]. For cross-linking SubE the protein solution was diluted to a concentration of 0.5 mg/mL (25.6 μM) in 100 mM HEPES buffer at pH 7.0. Gluteraldehyde was added to a final concentration of 10 mM from a 5% stock solution (499 mM). The reaction was stirred continuously at room temperature for 20 hours. After 20 hours, the reaction was quenched by dialyzing into an excess of primary amine (100 mM HEPES 40 mM ammonium acetate pH 7). This was stirred at room temperature for 4 hours and the protein solution was concentrated using an ultra filtration device (Millipore stirred cell Amicon Bioseparator) with 100 kMW cutoff membranes (Millipore regenerated cellulose) before being re-purified by size exclusion chromatography.

Synthesis of Mineralized SubE

After purification, the protein concentration was determined by UV-Vis spectroscopy ($\varepsilon_{280\ nm}$ = 24,075 $M^{-1}cm^{-1}$) and verified using a Bradford protein assay. The virus was shown to be intact by negatively stained TEM and DLS. Mineralization of magneto XSubE was performed similar to the method used previously[33]. Typically, 2 mg of the protein (5.7 X 10^{-10} moles) were added to the reaction vessel. For an iron loading factor of 10,000 Fe per protein cage, 5.7 μmoles of Fe^{2+} (10 mM deaerated $(NH_4)_2Fe(SO_4)_2 \cdot 6H_2O$) were added to the protein solution over 45 minutes at a constant rate. After all the iron solution was added, a 1/5 equivalent of H_2O_2 was added immediately (2 mM H_2O_2). The reaction was considered complete when the pH no longer changed (i.e. NaOH was no longer being added by the automatic titrator (Metrohm Titrino 718). After the reaction was complete it was dialyzed into 25 mM NaCl in order to remove any unreacted Fe^{2+} and oxidant.

Characterization

Dynamic Light Scattering Analysis: Dynamic light scattering (DLS) was used to determine the hydrodynamic diameter of the protein cage before and after the reaction. DLS was performed on a Brookhaven Instruments Corporation ZetaPALS particle size analyzer equipped with a 661 nm diode laser and monitoring the scattered light at 90° with an avalanche photodiode detector. The acquired correlation functions were then fit using a non-negatively constrained least squares analysis to report a hydrodynamic diameter.

Size Exclusion Chromatography: Before and after the reaction, the protein was passed over size exclusion chromatography as both a purification and a characterization of the mineral protein relationship. The chromatography system used was an ÄKTA Pharmacia 900 with a superose 6 SEC column (Amersham Pharmacia).

Transmission Electron Microscopy (TEM), Electron Diffraction, Negative Stain Reconstruction and Electron Energy Loss Spectroscopy: TEM, electron diffraction, and electron energy loss spectroscopy (EELS) were performed on a Leo 912 AB electron microscope equipped with an omega energy filter. Samples were prepared for TEM by depositing 5 μL of Magneto-XSubE on 300 mesh copper grids with a 15 nm thin carbon film (Ted Pella). HRTEM was performed on a Philips CM300FEG operating at 300 kV with a spherical aberration setting of 0.65 mm.

3D Image Reconstruction: Aliquots of unmineralized heated XSubE (~5μL) were stained for 30 s with 2% uranyl acetate. Images were recorded using a LEO 912 AB electron microscope (Zeiss, Germany) operated at 100 kV at a magnification of 50,000 and focal pairs with a range of ~0.40-1.2 μm under focus. All images were recorded digitally with a Proscan HSC2 (2048 x 2048 pixel) CCD camera with a scan step of 14μm, and corresponding pixel size of 2.63 angstroms on the object scale,

Image processing was performed with polar Fourier transform (PFT) methods, with imposed icosahedral symmetry[137]. Approximately 200 viral capsid particles were manually selected using the program X3D, and images were scaled to the mean and SD for all images[137]. The x,y origin as well as rotational orientation of the particles were

determined and refined by an iterative process. Three cycles of iteration were performed with a beginning accepted deviation of 0.9 below average, and the following iterations with an accepted deviation of 0.7 each. This process resulted in about two-thirds of the initial viral particles being rejected. Three-dimensional particle map was generated iteratively as well in comparison to a standard wild type CCMV map[96]. The 3D map and image were generated using RobEM to 30 angstrom resolution from 77 total particles[137].

Alternating Current Magnetic Susceptibility (ACMS) and Vibrating Sample Magnetometry (VSM) Measurements: ACMS and VSM were measured separately on a physical properties measurement system (Quantum Design). Sample preparation for both

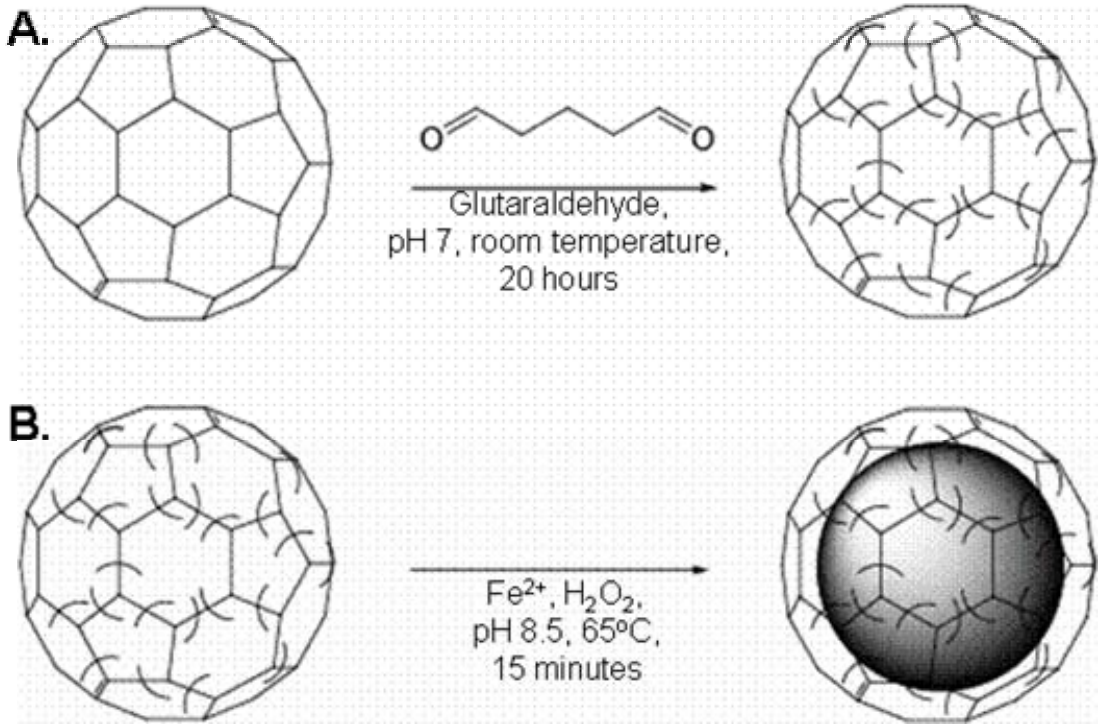

Figure 3.1: A. Schematic of crosslinking reaction using gluteraldehyde as the bifunctional crosslinker, B. Schematic of synthesis of ferrimagnetic nano-particles inside crosslinked SubE.

measurements was identical and involved purifying the γ-Fe_2O_3 synthesized XSubE by SEC, then dialyzing the purified magneto XSubE into pure water followed by lyophilizing the material to form a solid pellet. The pellet was weighed to an accuracy of 0.01 mg on an analytical balance and mounted for measurement. For ACMS the sample was placed in an ACMS straw and immobilized using Duco cement. ACMS were measured at 100, 500, 1000, 2500, 5000, 7500, and 10000 Hz while alternating a field of 10 Oe and sweeping the temperature from 300 K to 5 K. For VSM the sample was immobilized onto a quartz paddle using Duco cement and placed in the VSM, sample measurements were made at several temperatures (300 K, 200 K, 100 K, 50 K, 25 K, 5 K) and the field was swept from 8 T to -8 T while vibrating at a frequency of 40 Hz.

Results and Discussion

Genetic modification of the CCMV protein cage for the purpose of altering the electrostatic nature of the interior of the protein cage has been described previously [36]. The wild type CCMV protein has nine positively charged amino acids on its N-terminus, which are thought to project into the interior of the assembled protein cage architecture. Thus, the wild type CCMV capsid has a high positive charge density on the inside surface. The highly positive interior interface is thought to be critical for the interaction of the protein cage with native viral nucleic acid. If the first 25 amino acids are removed the virus is no longer infectious and must be isolated from a heterologous expression system[102]. Using PCR mediated site directed mutagenesis, the nine arginine and lysine amino acids on the N-terminus of each of the 180 subunits were changed to glutamic acid

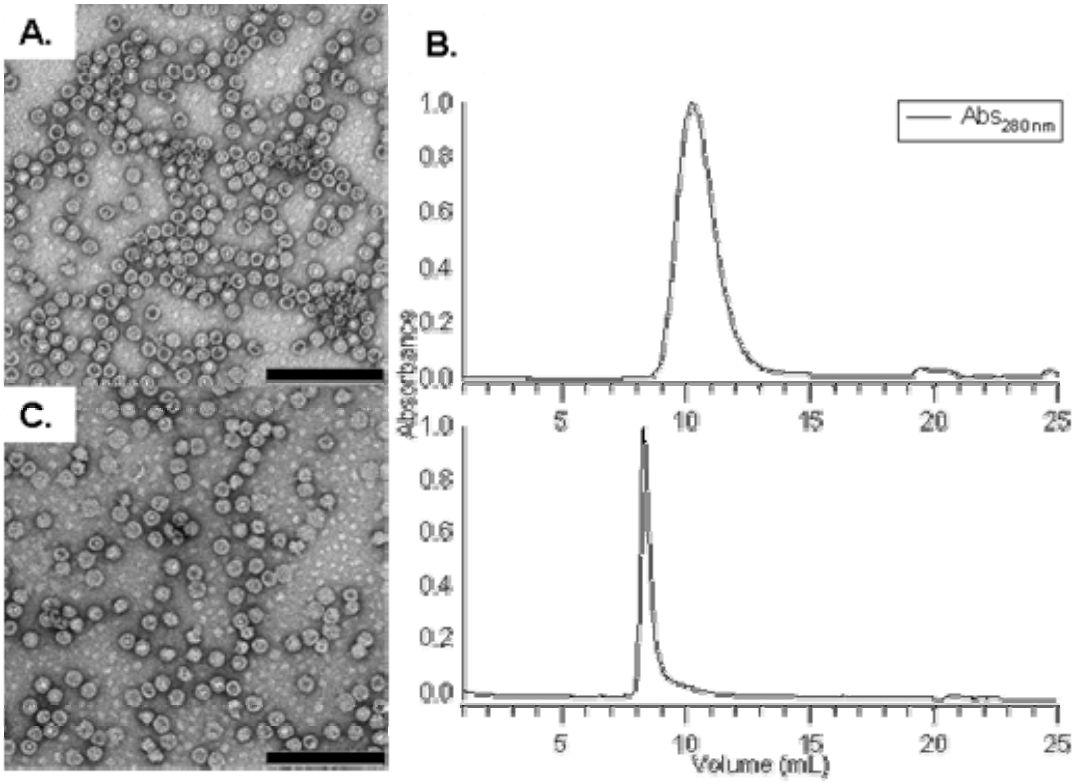

Figure 3.2: A. Negatively stained TEM of crosslinked SubE (XSubE), B. Comparison of SEC profiles of XSubE with heated XSubE, C. Negatively stained TEM of heated XSubE scalebars are 200 nm.

making the SubE mutant that assembles into a virus like particle (VLP) that is morphologically indistinguishable from the wild type virus. Because of the negative charge density (1620 negative amino acids on the interior of the assembled VLP), the SubE mutant is not capable of packaging viral RNA and is not infectious to the cowpea plant host. The SubE mutant is heterologously expressed in *Pichia pastoris* and is isolated as an assembled capsid with 180 subunits from cell preparations by centrifugation in a CsCl gradient with ultracentrifugation.

Previously, the SubE mutant was shown to be an effective template for the size constrained synthesis of the ferrihydrite polymorph of Fe_2O_3. However, for the synthesis of magnetically interesting iron oxides such as magnetite (Fe_3O_4) or maghemite (γ-Fe_2O_3)

elevated temperature and pH conditions are required and under these conditions the SubE construct is not sufficiently stable. Enhanced stability of the SubE mutant was achieved by crosslinking the subunits of the protein cage architecture using the bifunctional crosslinker gluteraldehyde (Figure 3.1A). Gluteraldehyde reacts with primary amines over a wide range of pH but nearly irreversibly at pH 7[136] and forms an intersubunit link that covalently locks the protein cage and dramatically enhances the range of temperature and pH stability of the capsid. The crosslinked SubE (XSubE) (Figure 3.2A) is a protein cage architecture that is 30 nm in exterior diameter and roughly 24 nm in interior diameter and appears identical to SubE by TEM, dynamic light scattering, and size exclusion chromatography. When XSubE was heated to 65^{o}C at pH 8.5, prior to Fe_3O_4 mineralization, the protein cage eluted slightly earlier than the unheated XSubE or SubE protein cages (Figure 3.2B). The elution of the heated XSubE is consistent with a slightly larger particle (but not an aggregated sample) but this was not corroborated by the data from the negatively stained TEM sample (Figure 3.2C). Since there was some uncertainty as to the changes in structure of the heated XSubE, a three dimensional reconstruction was performed using TEM data from negatively stained samples. Three-dimensional image reconstruction of the heated XSubE capsid reveals no significant structural alterations as compared to the structure of wild type or SubE CCMV capsids at the resolution of reconstruction (30Å) (Figure 3.3). The external diameter of 29.5 nm and internal cavity size of 21.5 nm from the reconstruction of heated XSubE strongly suggest that there are no dramatic size changes to the capsid upon heating and we conclude therefore that the altered elution profile of the sample was due to altered

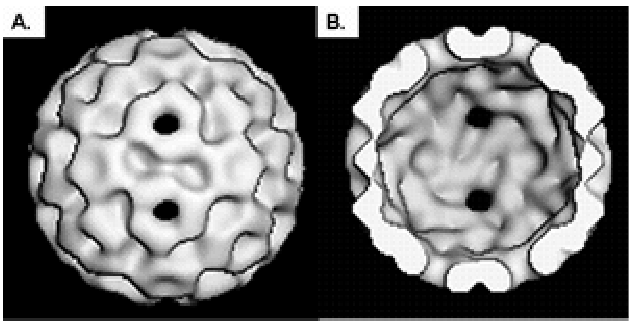

Figure 3.3: Negative stain 3D reconstruction of heated XSubE, A. Entire viral capsid, B. Slab cutaway viewing the inside.

interactions between the capsid and the resin. Most significantly, it is important to note that after heating for two hours at 65 ^{o}C, the protein capsid remains intact with a minimally altered geometric architecture.

TEM and three-dimensional reconstruction of heated XSubE confirmed that the VLP maintained its cage-like properties under the conditions necessary for mineralization (Figure 3.2). The XSubE was subsequently used as a constrained reaction vessel for mineralization of the ferrimagnetic iron oxide γ-Fe_2O_3 (Figure 3.1B). The synthetic method is similar to those reported for mineralization of other protein cages[33]. Briefly outlined, a solution of Fe(II) was added (via syringe pump) to the XSubE over 15 minutes. This was followed by the addition of a substoichiometric amount (1/5 of an equivalent) of H_2O_2 and the reaction was allowed to proceed for 30 minutes to 1 hour. The synthesis resulted in the formation of a brown colored solution of γ-Fe_2O_3 (maghemite) nano-particles encapsulated within the XSubE (magneto XSubE). DLS and SEC measurements were performed immediately after the reaction and the protein cage composite appeared similar in size to the heated XSubE (Figure 3.4). SEC shows a coelution of the mineral (absorbance 350 nm) with the assembled protein cage

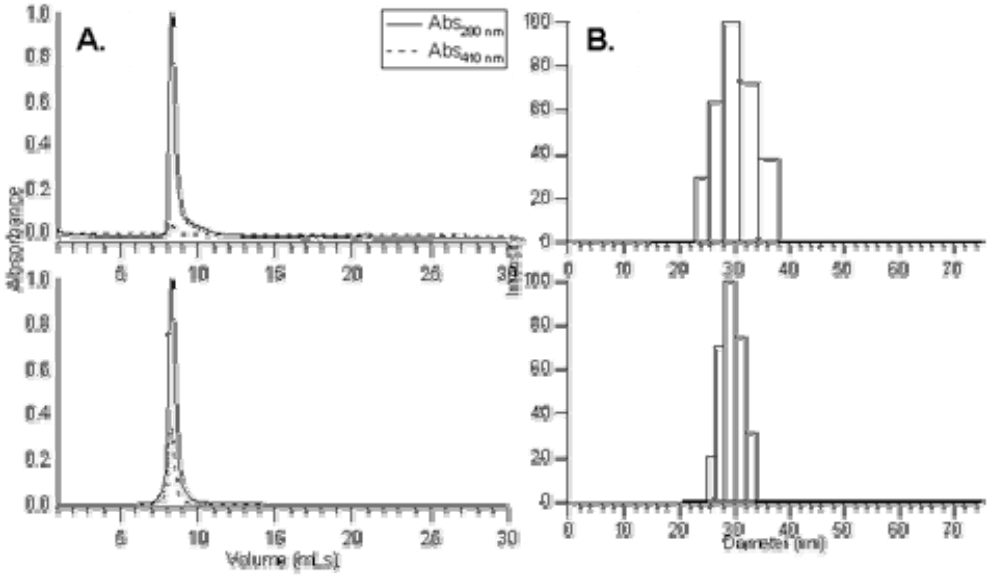

Figure 3.4: Comparison of A. SEC and B. DLS of heated XSubE with γ-Fe_2O_3-XSubE.

(absorbance 280 nm) suggesting that mineral is entirely encapsulated within the protein cage (Figure 3.4A). DLS indicates that before and after reaction the external hydrodynamic diameter does not change, further indicating that the mineral is encapsulated inside an unaltered VLP (Figure 3.4B).

The mineralized sample was imaged directly by TEM; negative staining of magneto-XSubE shows a capsid protein "halo" around an electron dense core (Figure 3.5A). Unstained TEM revealed electron dense cores that correspond to the maghemite nano-particles (Figure 3.5B). The mineralized maghemite nano-particles exhibited a distribution of sizes (mean diam. 16.5 ±5.18 nm) but were all constrained within the XSubE cage. Electron diffraction confirmed the mineral phase to be the cubic iron oxide, either magnetite or maghemite (Figure 3.5C). Further characterization of these particles by high resolution electron microscopy (HRTEM) confirmed the mineral structure and

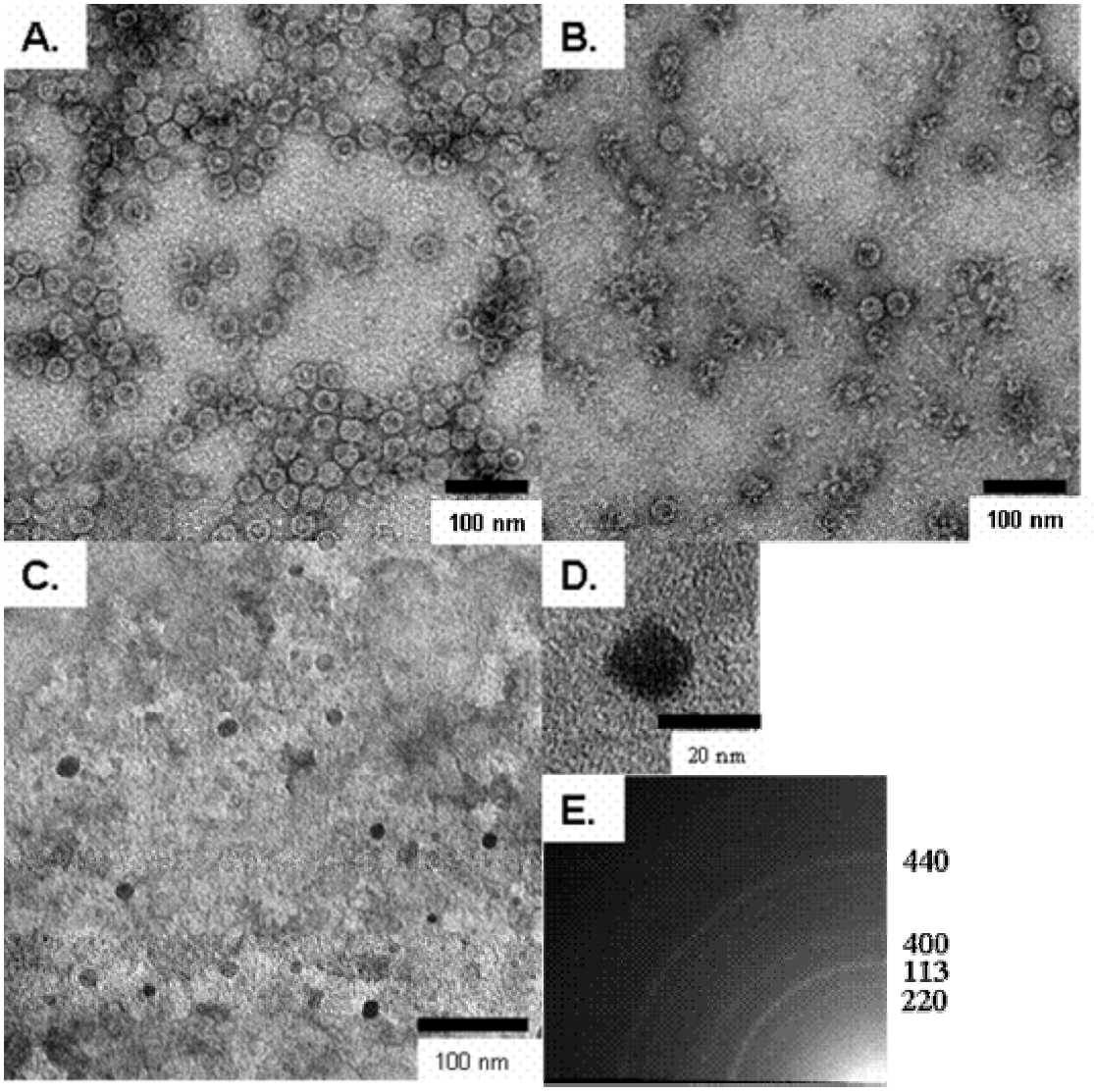

Figure 3.5: A. Negative stain TEM of heated XSubE, B. negative stain TEM of γ-Fe_2O_3-XSubE, C. Unstained TEM of γ-Fe_2O_3-XSubE, D. Single particle of γ-Fe_2O_3 inside XSubE, E. Electron diffraction of γ-Fe_2O_3-XSubE with indexed d-spacings.

indicated single crystal particles of maghemite with lattice spacing corresponding to the 113 zone axis (Figure 3.6A) and the 220 lattice planes (Figure 3.6B).

Magnetic characterization was performed using alternating current magnetic susceptibility (ACMS) in order to determine a blocking temperature of the material and

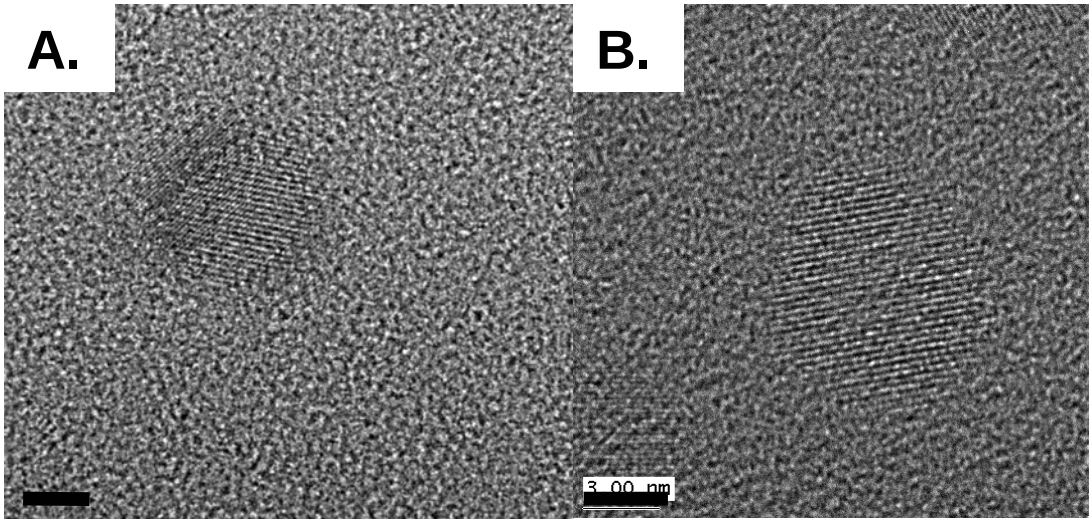

Figure 3.6: HRTEM of γ-Fe_2O_3-XSubE looking down the A. 113 zone axis and the B. 220 plane (scalebar is 3 nm).

vibrating sample magnetometry (VSM) in order to determine hysteresis of the particles close to the blocking temperature[138]. AC magnetic susceptibility is a measure of how likely a material is to align with an alternating magnetic field of 10 Oe amplitude. The measurement is based on an energy barrier between aligning with the field vs. aligning against the field when the 10 Oe field is applied. ACMS is a measurement of dynamic magnetic properties and changes with respect to temperature and measurement frequency. The blocking temperature T_b is the temperature where the energy barrier (E_a) between flipping spins (magnetic anisotropy energy) is equal to the thermal energy of the system. In order to determine the T_b, approximately 1 mg of material was prepared as a lyophilized powder and placed into the ACMS. The initial temperature was set to 300 K and taken down to 5 K while measuring ACMS at several different frequencies (Figure 3.7). In Figure 3.7 both the real and imaginary components of the magnetic susceptibility are plotted as a function of both frequency and temperature. The intensities of all frequencies have been normalized to 1 and the T_b of maghemite nano-particles prepared

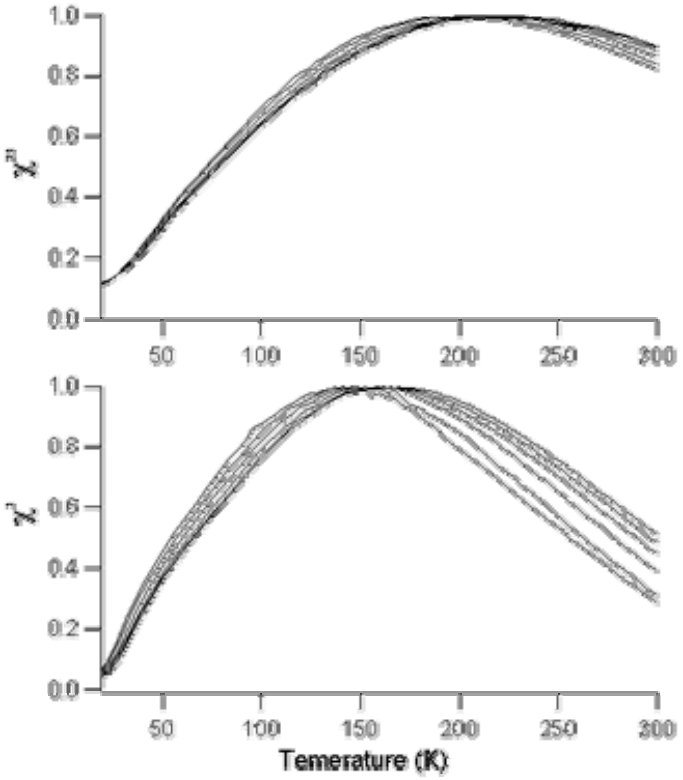

Figure 3.7: Normalized real and imaginary components to the ACMS of γ-Fe_2O_3-XSubE, frequencies represented are 500, 1000, 2500, 5000, 7500, and 10000 Hz.

inside XSubE was determined to be 152 K when measuring at 1000 Hz and using a Gaussian fit to the imaginary component of the susceptibility. The imaginary component does give a broad signal verifying, as TEM has, that there is a wide distribution of sizes of maghemite particles. While the peak is broad, there does appear to be only one peak with no shoulder indicating that very few particles are outside the range of particle size. One of the advantages to synthesizing maghemite inside the viral protein cage is that the particles are completely isolated from each other as determined by a Nėel-Arrhenius plot of ln $(\text{frequency})^{-1}$ vs. $1/T_b$ (Figure 3.8)[139]. The Neel-Arrhenius plot gives a relationship between the blocking temperature and the frequency of measurement and the linear shape to this plot indicates that the protein cage isolates the magnetic particles from each other

preventing any interaction. This is important if these nano-particles are used in a device so that the spin of one particle will have no effect on the spin of a neighboring particle.

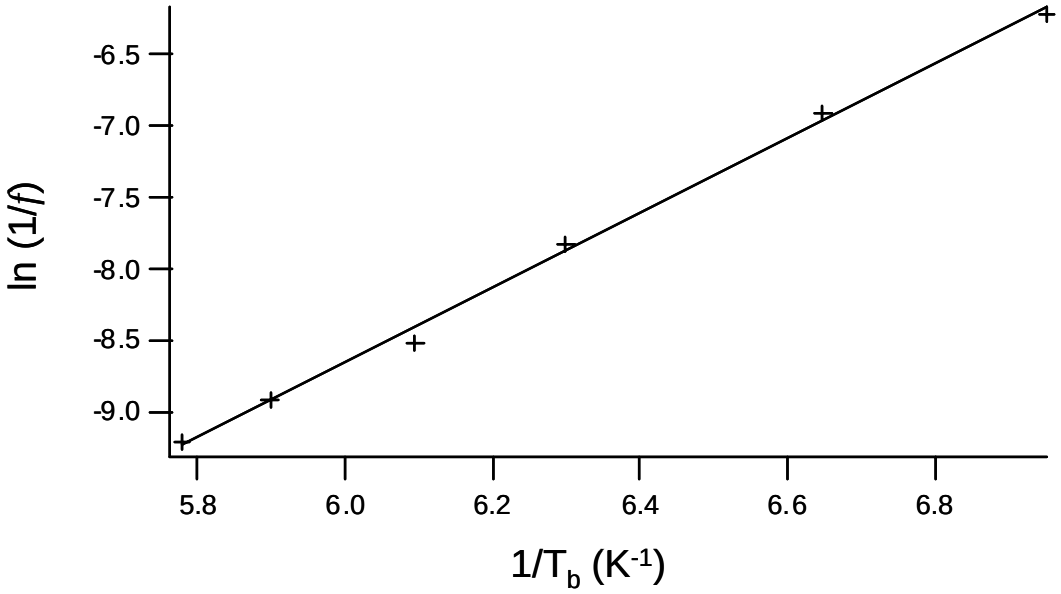

Figure 3.8: Neel-Arrhenius plot of γ-Fe_2O_3-XSubE.

Vibrating sample magnetometry is used for the measurement of two properties, saturation magnetization, and hysteresis. Hysteresis, meaning "to lag behind" is a term first introduced by Ewing to describe how a ferromagnetic material behaves when the applied magnetic field (H) is switched. Before applying a field, the material (ferromagnetic, ferrimagnetic, or superparamagnetic) is in its initial state (no magnetic moment), as an H field is applied in a particular direction the magnetic induction of the material begins to increase in the same direction as H. After magnetizing the sample with an applied magnetic field in one direction, if the magnetic field is gradually switched to the opposite direction the ferromagnetic material will maintain some of the initial magnetization until a critical field is reached (Coercive field) causing for the overall spin

moment of the material to switch[138]. While ACMS at 1000 Hz gives a T_b of 150 K, it would be expected that magneto-XSubE would have a hysteresis loop close to this temperature, however, blocking temperature is dependent on the frequency of measurement and while ACMS is measured at 1000 Hz, VSM analysis is measured over the course of a couple of hours. For this experiment VSM was measured over 335 minutes, which if converted to a frequency would correspond to a frequency of 4.98 $_E$-5 Hz. If this is plotted on the Neel-Arrhenius plot it would correspond to a blocking temperature of about 76 K indicating that in VSM above 76 K there is an overall superparamagnetic behavior and that the superparamagnetic behavior is not blocked until measuring at a lower temperature than 76 K. A hysteresis loop measured at 50 K shows a coercive force of about 75 Oe (Figure 3.9). As the temperature is lowered to 5 K the coercive force goes up to ~400 Oe.

The measured saturation magnetic moment at 50 K for the magneto XSubE was measured to be 8.97 e 10^{-18} emu/particle. Magnetite has been synthesized inside other protein cages including mammalian ferritin[80] and also *Listeria* dps[33]. We have synthesized magnetite inside horse spleen ferritin in a way similar to that reported[33] and measured the saturation magnetic moment to be 3.00 e 10^{-18} emu/particle at 50 K. So the moment per particle for magneto XSubE is about three times larger than that measured for magneto ferritin. This is rather interesting and shows the size dependent nature of the mineralized protein cages, it would be expected that the increase in magnetic moment would scale with the volume of the particle, however this is not the case when discussing this size of mineral. These size dependent properties are discussed in detail in chapter 5.

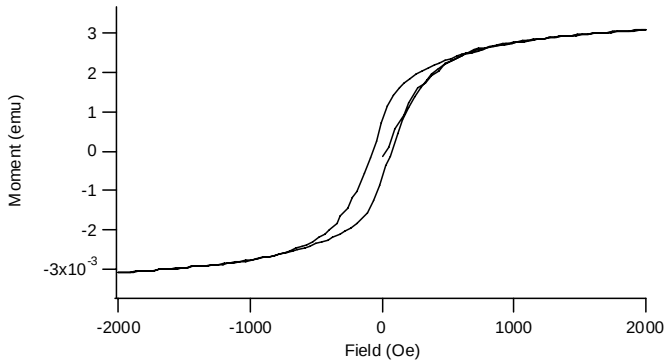

Figure 3.9: VSM hysteresis loop of γ-Fe_2O_3-XSubE measured at 50 K.

Conclusion

Cross-linked subE represents a viral protein cage that has been designed to perform biomimetic synthesis that is not naturally achieved in any other viral protein. This required genetic manipulation of the wild type virus along with isolation of the virus from an expression system that also would not normally be used for virus isolation. Once the protein is isolated it was chemically modified by a very simple cross-linking reaction. The cross-linked protein is stable to a variety of conditions that would cause most proteins to lose structure, disassemble, or aggregate. Upon heating the XSubE 3-D negative stain reconstruction indicates that there is no apparent change in the overall morphology of heated XSubE. The modified viral protein cage has been used as a template for the mineralization of a ferrimagnetic iron oxide magnetite or maghemite making magneto-XSubE. The phase of this material was verified to be either Fe_3O_4 or γ-Fe_2O_3 by selected area electron diffraction as well as high resolution TEM. Unstained TEM imaging shows a size polydispersity of about 25 %. This broad dispersity represents the dynamic nature of proteins, which are soft and can expand and contract

around the stable nano-particle. Magneto-XSubE is a biological protein cage that is compatible to biological systems, these particles could be applied in the future as a dark field MRI contrast agent and possibly as a therapeutic agent for magnetic hyperthermia.

MATERIAL SYNTHESIS INSIDE COWPEA CHLOROTIC MOTTLE VIRUS (CCMV)

Introduction

In chapters two and three the synthesis of transition metal oxides were discussed. These materials can have interesting magnetic properties that are worth pursuing in order to gain further insight into the magnetic behavior of noninteracting magnetic particles. With a current push toward the development of an alternative to the hydrocarbon based fossil fuels there has been a renewed interest in the development of catalytic systems that can efficiently and cheaply produce $H_{2(g)}$. H_2 is a desirable fuel because it burns cleanly with the only biproduct of combustion being H_2O. The synthesis of photocatalytic nano-particles has largely been directing the synthesis of noble metal colloids by various techniques. Varpness *et al.* has developed a protein cage based synthetic approach for mineralization of Pt colloidal particles for the purpose of photocatalytic production of $H_{2(g)}$[131]. The H_2 production capacity was measured for Pt mineralized protein cages and the maximum efficiency was on the order of some of the best systems available including the enzymatic reduction of water through hydrogenase. Other materials that are of some interest are tungsten and molybdenum sulfides[140-142]. Hinnemann *et al.* have determined that MoS_2 can potentially serve as a photocatalyst for the reduction of H_2O to $H_{2(g)}$ based on density functional theory (DFT) calculations[143].

In chapter one, CCMV was introduced as a viral protein cage that has been used for the synthesis of crystalline polyoxometallates[35]. In this chapter the synthesis of

polyoxomolybdate inside of CCMV will be discussed along with the formation of either MoS_2, or reduced forms of Mo_xO_y. These materials were probed for their use specifically in the photocatalytic evolution of $H_{2(g)}$ based on the one electron reduction of H^+. Furthermore, these materials formed very monodisperse particles that fit the interior dimensions of CCMV making them interesting from a structural perspective for the purpose of probing the protein/mineral interface. The materials were thoroughly characterized using high resolution TEM, electron spectroscopic imaging, and electron diffraction. Material synthesis took place in two different forms of CCMV, wild type and a mutant form (K42R) which has an added stability due to the presence of a salt bridge between E34 and R42[144]. After stabilizing the protein cage by chemically crosslinking the subunits as reported in chapter 3, these two forms of CCMV behave identically to each other and will just be discussed crosslinked CCMV (XCCMV).

Materials and Methods

Chemicals

Ammonium molybdate (NH_4MoO_4), $Na_2S{\cdot}9H_2O$, dimethyl amine borane, and most buffers were purchased from Sigma-Aldrich and used as received with filtering each solution prepared. Sodium hydrosulfite, hydroxyl amine, and Hepes buffer were purchased from Fisher Scientific and used as received. All water used was purified through a nanopure system to 18 MΩ resistivity.

Protein Purification

Formation of the salt stable mutant of CCMV (SSCCMV) has been reported previously[144]. Both wild type CCMV and SSCCMV are infectious to their plant host and were isolated by homogenization of plant leaves followed by low speed (6000 rpm) centrifugation for 20 minutes to remove the plant material. The supernatant was centrifuged at 25000 rcf for two hours to pellet the virus, which was then resuspended in a minimal amount of virus buffer (50 mM acetate 300 mM NaCl pH 4.8) before being purified by a CsCl gradient using a solution of 39 % CsCl and spinning at 38000 rcf to band the virus in the gradient. After dialysis into virus buffer, further purification was accomplished by size exclusion chromatography (SEC) (ÄKTA 900) using a gel filtration column (Amersham Biosciences Superose 6 10/300).

Chemical Stabilization of the Protein Cage

The protein subunits of CCMV were chemically cross-linked in order to increase their stability. Chemical crosslinking was performed using gluteraldehyde in a method equivalent to that discussed in chapter 3.

Molybdenum Mineral Synthesis

The synthesis of polyoxomolybdate was undertaken by a modified technique to that reported for polyoxotungstate [35]. Dialysis was used for the synthesis of all the Mo_xO_y species, in these reactions purified crosslinked CCMV (XCCMV) or SSCCMV (XSSCCMV) were dialyzed into pH 7 buffer (50 mM Hepes 100 mM NaCl). The dialysis buffer was then changed to pH 7 buffer with 25 mM NH_4MoO_4 (50 mM Hepes

100 mM NaCl). After dialyzing for two hours the buffer was again changed to pH 4.5 (50 mM acetate 100 mM NaCl). The resulting material is the polyoxomolybdate CCMV.

Many of the syntheses involved further reduction of the polyoxomolybdate material to a reduced phase of Mo_xO_y. This involved either dialysis into pH 4.5 buffer containing reducing agent, or the direct addition of four equivalents of reducing agent. The reducing agents used were dimethyl amine borane (DMA) and hydroxyl amine.

In order to transform the polyoxomolybdate CCMV to MoS_2-CCMV, mineralized samples of either XCCMV or XSSCCMV were placed in several wells of a 96 well plate (200 μL in each well). The 96 well plate was then placed in a vacuum dessicator in the presence of a solution of 50 mM Na_2S freshly prepared in water and acidified to pH 1 with 2 M HCl. The vacuum dessicator was then sealed and the vacuum pump was turned on in order to cause $H_2S_{(g)}$ to fill the dessicator and diffuse into the mineral containing solutions. The reaction was considered complete after four hours in the dessicator.

Characterization

Characterization of the products were performed using dynamic light scattering (DLS), size exclusion chromatography (SEC), transmission electron microscopy (TEM), electron diffraction, positive stain 3D image reconstruction and high resolution TEM (HRTEM) were all performed as reported in chapter three with the exception that 3D image reconstruction was not performed by staining the protein cage, but rather by using the mineral as a positive stain and still looking at the area around the mineral to determine electron density that could be added together in order to gain an image corresponding to the protein cage.

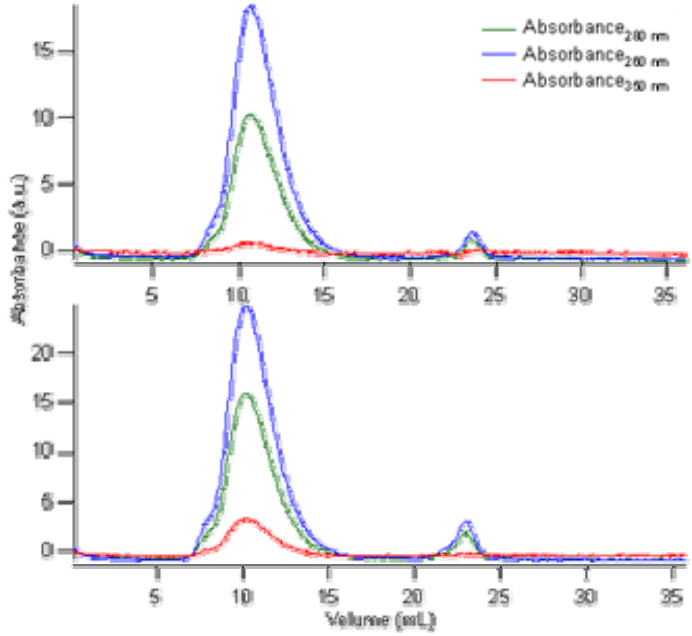

Figure 4.1: SEC of polyoxomolybdate and MoS_2-XCCMV monitoring at 260 nm, 280 nm, and 350 nm.

Photocatalysis and H_2 Production

Photocatalysis and H_2 production were measured using the technique reported by Varpness *et al.* with a few variations[131]. Briefly, a solution of 0.08 mg/mL mineralized protein was prepared in either pH 2 buffer (200 mM formate) in a sealable vial, EDTA was added to a concentration of 25 mM, then ruthenium bipyridine ($Ru(bpy)_3$) (.5 mM), and finally methyl viologen (0.5 mM). The vial was sealed and degassed under vacuum for 20 minutes, then backfilled with $N_{2(g)}$. Photolysis was performed for one hour at various temperatures using a xenon arc lamp (150 W) and experiments were performed with an IR filter and with and without a UV filtering glass in place. $H_{2(g)}$ production was measured using GC according to the method reported by Varpness *et al.* In some experiments nickel bipyridine ($Ni(bpy)_2$) was used as the photoactivator, this had to be

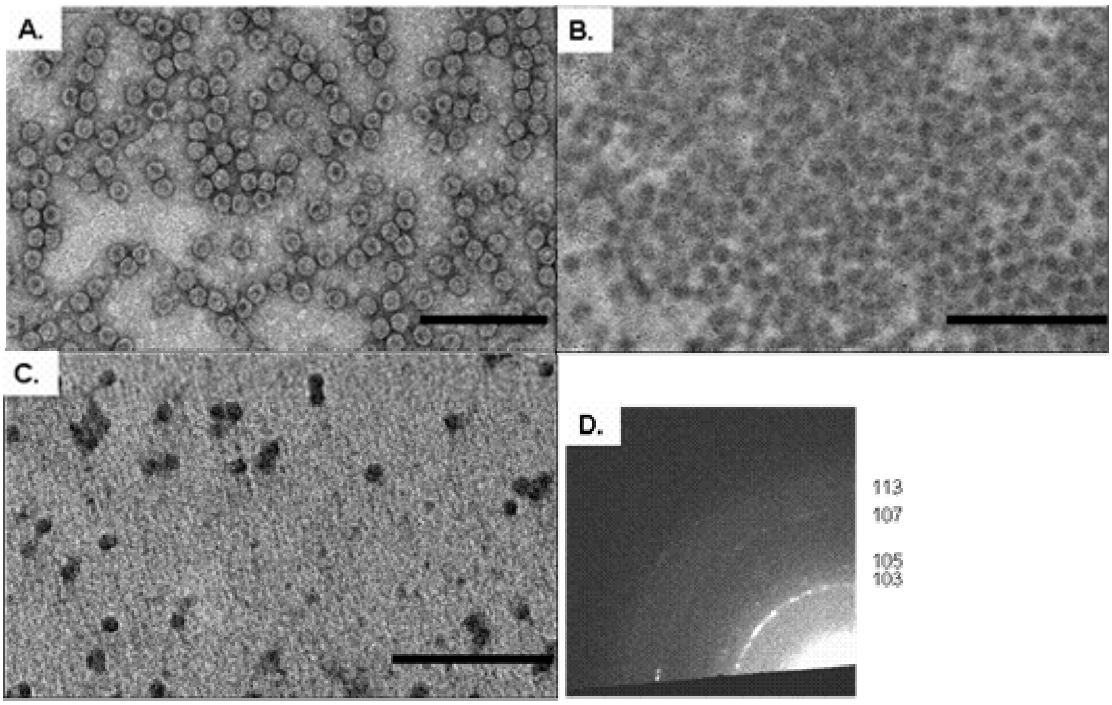

Figure 4.2: A. Negatively stained TEM of polyoxomolybdate mineralized XCCMV, B. Unstained TEM of polyoxomolybdate-XCCMV, C. Unstained TEM of MoS_2-XCCMV (scalebars are 200 nm), D. Electron diffraction of MoS_2-XCCMV with the most intense circles indexed to the corresponding lattice planes.

synthesized by preparing 25 mM $Ni(NO_3)\cdot 6H_2O$ and 50 mM 2,2'-dipyridyl in acetonitryl and allowing it to react for two hours.

Results and Discussion

Wild type CCMV and a mutant (K42R) termed salt stable CCMV (SSCCMV) were used as size constraining reaction vessels for the synthesis of a polyoxomolybdate mineral. The reaction involved in making the molybdate involves incubating at pH 7 for an extended period of time, during this time CCMV is in its swollen conformation (chapter 1). While in a swollen state the virus is destabilized and has a tendency to fall apart under these conditions. In order to prevent this from happening both CCMV and SSCCMV were chemically stabilized according to scheme 3.1A presented in the last

chapter. After crosslinking, the protein cages (termed XCCMV and XSSCCMV) were stable to pH 7 for an indeterminate amount of time.

CCMV has been shown previously to be a viable container for the size constrained synthesis of polyoxometallates[35]. These reactions rely on the complimentary electrostatic charge with the interior of the virus have a large positive charge, which interacts with the negatively charged metallate precursor ions. Presumably swollen conditions are also a benefit, since at pH 7.0 the virus has large .8-1.2 nm pores open around the quasi-three fold axes. These pores would direct the precursor ions to concentrate on the interior of the virus. In the present research, cross-linked CCMV (XCCMV) was used for the mineralization of polyoxomolybdates. After forming the initial mineral inside the protein cage a solid state transformation was initiated by adding a S^{2-} atmosphere to the mineral, thus forming a crystalline form of MoS_2. The products of mineralization were characterized by size exclusion chromatography (SEC) (Figure 4.1). The elution profiles for mineralized cages are identical to unmineralized protein with the exception that there is an increase in the absorbance at 350 nm for the MoS_2 mineralized XCCMV due to the orange color of the mineral (Figure 4.1B). All preparations were visualized by TEM (Figure 4.2 A, B, and C) and by electron diffraction (Figure 4.2D). Negatively stained images of the mineralized XCCMV indicate that the protein is still intact (Figure 4.2A) while unstained images of the polyoxomolybdate mineralized XCCMV show poorly crystalline electron dense cores (Figure 4.2B). Figure 4.2C is MoS_2-XCCMV after performing the transformation of polyoxomolybdate core, these particles appear darker which would either imply that they are more electron dense,

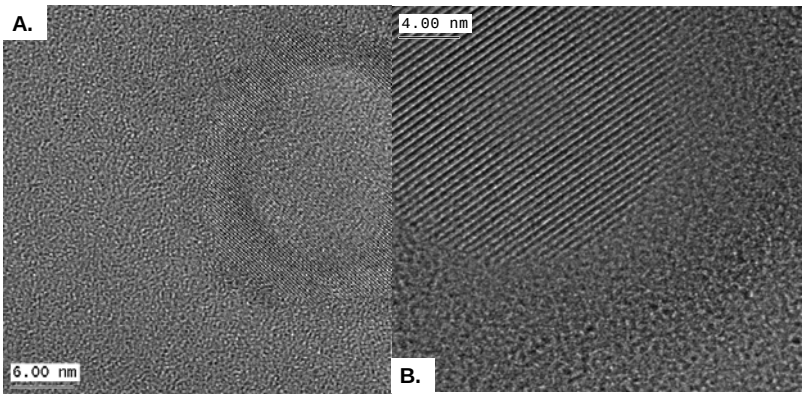

Figure 4.3: HRTEM of two different samples of MoS_2-XCCMV, A. Hollow single crystal particle of mineral, B. Another single crystal particle that may be hollow, each particle is 24 nm in diameter.

or that they are more crystalline. Electron diffraction was attempted on polyoxomolybdate-XCCMV, however, no powder pattern was seen. After transforming to the more electron dense MoS_2 phase an electron diffraction powder pattern was visible (Figure 4.2D) indicating that these particles are more crystalline than the molybdate precursor. The powder pattern was indexed to a mineral phase of MoS_2 (molybdenite)[145].

High resolution TEM was performed in order to further characterize the MoS_2-XCCMV crystalline material. Figure 4.3 shows two collected images of MoS_2-XCCMV and it is clear from the images that the mineral is single crystalline and fills the dimensions of the protein cage. While electron diffraction indicated that the mineral phase that is being prepared is that of MoS_2, the lattice spacing does not index to the structure of Molybdenite. This may be due to the fact that electron diffraction is looking at a collection of mineralized particles while HRTEM only looks at one particle at a time. More apparent than this is that the overall structure of the mineral does not correspond to that reported by other groups (Figure 4.4)[146].

An interesting facet of the structure of the mineral inside CCMV is that it matches well to the interior dimesions of CCMV. This allows the study of the protein/mineral interface. In an initial attempt to study how the protein interacts with the mineral 3D-image reconstruction was performed similar to how it was reported in chapter 3 only in this experiment the mineral served as a type of positive stain. The electron density belonging to the protein is still present in an unstained TEM, however it is difficult to see. If all particles can be imaged with the assumption that there is a protein cage coating them then the structure of the protein cage can then be elucidated by measuring hundreds of particles and averaging to accumulate the electron density coating the particles that would add up to a protein cage. Figure 4.5 is a 3D image reconstruction of the mineral encapsulated protein cage. This was observed without any staining done and with icosahedral symmetry imposed on the volume surrounding the mineral particles.

The MoS_2-XCCMV particles were tested for their ability to produce $H_{2(g)}$

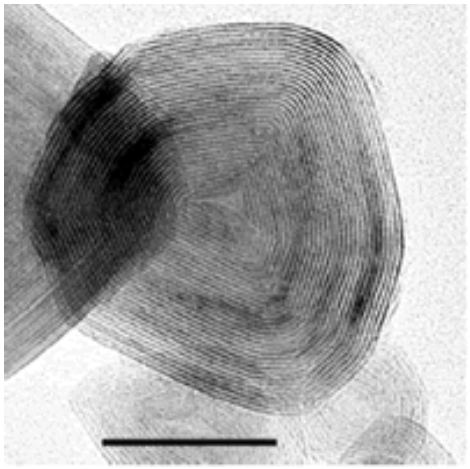

Figure 4.4: HRTEM of MoS_2 from Tenne *et al.* This shows a layered structure with hexagonal symmetry.

photocatalytically. These experiments relied on the catalytic function of a material to

accept an electron from a sacrificial electron donor (some organic species) and transfer that electron to H^+ either in solution or bound to the material. This process is completed using a photo-activator and an electron shuttle. For the electron donor EDTA was used similar to experiments performed by Varpness *et al.* The pH of the solution was varied between pH 2 to 4.5, under the lower pH conditions there is a greater likelihood that H^+ will bind to the mineral and make it more likely to be reduced, however lower pH makes it difficult to keep the electron donor in solution. The photo-activator was typically $Ru(bpy)_3^{2+}$, which very efficiently gets excited to the 3+ state in giving up an electron to the electron mediator (methyl viologen). In some cases $Ni(byp)_2^{2+}$ was synthesized and used as a different photoactivator. Extensive experiments were performed under several conditions by varying pH, reducing agents, photo-activators, and electron donors. In all of these experiments no reduction of H^+ to $H_{2(g)}$ was measured above background. There are multiple explanations for this observation. It is possible that while MoS_2 may have some activity for reduction of H^+ electrochemically, there may not be any photocatalytic function. Also the HRTEM indicates that the phase of mineral does not correspond to MoS_2 though electron diffraction data indicated that it did. These are questions that still need to be answered.

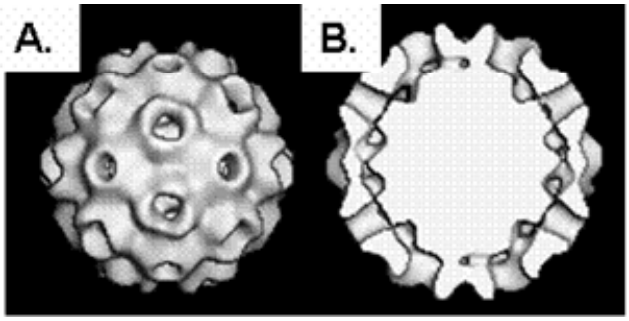

Figure 4.5: 3D positive stain reconstruction of XCCMV with reduced Mo_xO_y synthesized inside the protein cage.

Conclusion

A molybdenum containing mineral has been synthesized inside a chemically stabilized viral protein cage. The synthesis resulted in very monodisperse particles that match well the interior dimensions of the virus. While the mineral that was prepared showed no photocatalytic activity for the production of H_2, there may be some other function for these mineralized protein cage systems.

From a fundamental scientific perspective, these particles offer a vast realm of possibility at studying biomineralization by allowing a direct measurement of the mineral surface with the 3D reconstruction of the protein cage. Future work will include further analysis of the minerals by HRTEM for the purpose of doing a through focal series reconstruction. This technique will give an exact surface representation of the inorganic mineral and may enable probing very small deviations in the mineral surface to within 0.1 nm[147]. This combined with the 3D reconstruction will allow direct observation of the protein mineral interface.

SIZE DEPENDENT BEHAVIOR OF THE FERRIMAGNETIC MINERAL MAGHEMITE SYNTHESIZED INSIDE DIFFERENT SIZES OF PROTEIN CAGES

Introduction

Part of the reason why nano-materials are of such interest is that materials prepared in the size regime of four to 30 nm have properties that are different from molecular materials as well as from bulk materials. In this size range there are drastic changes in electronic, catalytic and magnetic properties that vary widely with relatively small changes in particle diameter. A clear example of this is the electronic properties of quantum dots (Qdot)[148-150]. A Qdot serves as an adequate mode of storing reactive electrons by delocalizing them over the surface of an entire particle. Qdots are typically 12-14 or 11-15 semiconductors that form nano-particles which hold a discreet number of electrons and can easily stabilize electron/hole pairs and are typically pursued for optical and fluorescent properties[151, 152]. As the size of these particles change by as little as

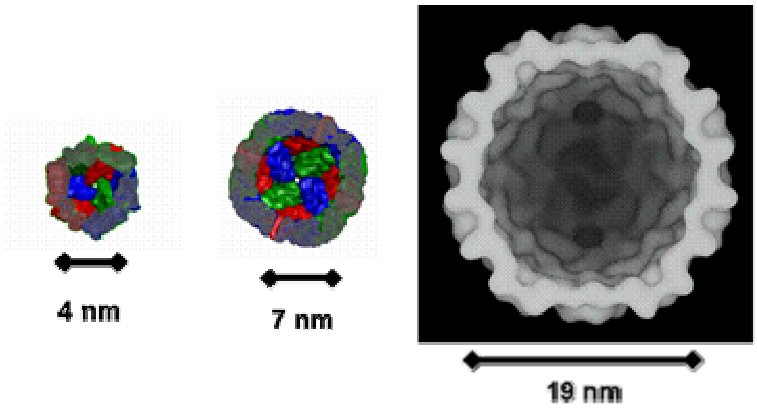

Figure 5.1: Surface model or cryo electron reconstruction of the interior of, A. LDps, B. Fn, C. SubE.

nanometer increments, the properties drastically change. The magnetic properties of magnetite or maghemite particles also change with respect to the particle size. In this chapter many of the size dependent properties of maghemite synthesized in three different protein cage systems *Listeria innocua* Dps (LDps), horse spleen ferritin (Fn), and the ferritin mimic mutant of CCMV (SubE) will be discussed (Figure 5.1). Since this chapter is strictly discussing size dependent parameters, the particles prepared inside these three protein cages will be distinguished as 4 nm, 7 nm, and 19 nm in reference to magneto LDps, magneto Fn, and magneto XSubE respectively. Four techniques will be discussed to compare the different sizes of maghemite particles; X-ray absorption spectroscopy (XAS), which probes the detailed electronic structure of the material, vibrating sample magnetometry (VSM), which probes the static magnetic nature of the material, and two dynamic measurements; alternating current magnetic susceptibility (ACMS) and electron magnetic resonance spectroscopy (EMR). A detailed understanding of the measurements performed will not be described here, but rather an intuitive observation of differences in the spectral measurements of the particles will be made.

Materials and Methods

Materials Synthesized

Samples of maghemite or magnetite synthesized in horse spleen ferritin (Fn) and *Listeria innocua* dps (LDps) were synthesized as described in chapter 2 for the preparation of γ-Fe_2O_3, the sample prepared in cross-linked SubE (XSubE) was described

in chapter 3. After synthesis the particles were purified by size exclusion chromatography and dialyzed into pure ddi (Nanopure 18 MΩ resistivity).

Sample Preparation

All samples were prepared nearly the same as reported in chapter three. Briefly; purified mineralized cages were dialyzed into water or precipitated by the addition of ethanol. The solid material was isolated, either by lyophilization or by centrifugal isolation of precipitate.

Characterization

X-ray Absorption Spectroscopy: All XAS spectra were collected using beam-line U4B at the national synchrotron light source (NSLS); part of Brookhaven national laboratory (BNL). Spectra were collected in electron yield mode. Electron yield measurements were collected by precipitating the mineralized protein cages and placing the solid material on a copper sample paddle for measurement.

Vibrating Sample Magnetometry (VSM) and Alternating Current Magnetic Susceptibility (ACMS): VSM and ACMS were measured separately on a physical properties measurement system (PPMS, Quantum Design). Sample preparation for both measurements was identical and involved lyophilizing the purified mineralized protein cages into a solid pellet, the pellet was weighed to an accuracy of 0.01 mg on an analytical balance and mounted for measurement. For VSM the sample was immobilized

onto a quartz paddle using Duco® cement and placed in the VSM, sample measurements were made at several temperatures (300 K, 200 K, 100 K, 50 K, 25 K, 5 K) and the field was swept from 8 T to -8 T while vibrating at a frequency of 40 Hz. For ACMS the sample was placed in an ACMS straw and immobilized using Duco® cement. ACMS were measured at 100, 500, 1000, 2500, 5000, 7500, and 10000 Hz while alternating a field of 10 Oe and sweeping the temperature from 300 K to 5 K.

Electron Magnetic Resonance (EMR): Sample preparation involved lyophilizing the purified protein cages to a powder and placing the samples in fused silica sample tubes (0.3 mm internal diameter). EMR spectra were obtained at ambient temperature at microwave frequencies of S-band (4.0 GHz), X-band (9.8 GHz), Q-band (4.6 GHz), and W-band (94.9 GHz). The X-and S-band measurements were obtained on a Bruker EMX EPR (electron paramagnetic resonance) instrument, the Q-band on a Bruker Elexsys instrument, and the W-band on an instrument described previously. Spectra were taken in conventional, continuous wave mode of operation with 100 kHz field modulation and lock-in detection. Modulation amplitude was 10 G and microwave power of 1.0 mW were used for multifrequency EMR.

Table 5.1: D-Spacing comparison between magnetite, maghemite and protein encapsulated minerals

Magnetite	Maghemite	LDps	Fn	XSubE
2.967	2.953	2.95	2.98	2.98
2.532	2.518	2.51	2.54	2.54
2.099	2.089	2.09	2.11	2.11
1.485	1.476	1.45	1.49	1.49

Results and Discussion

All mineralized protein cages were synthesized and characterized by the standard methods as discussed in chapters two and three. Electron diffraction was measured on all three samples and compared to the most intense d-spacings of both magnetite (Fe_3O_4) and maghemite (γ-Fe_2O_3). These values are reported in table 6.1. It clear that there is no noticeable difference between the samples based on this technique and the values line up well with those calculated for the bulk values of each phase.

X-ray Absorption Spectroscopy (XAS)

XAS is a technique used to determine the electronic and structural characteristics

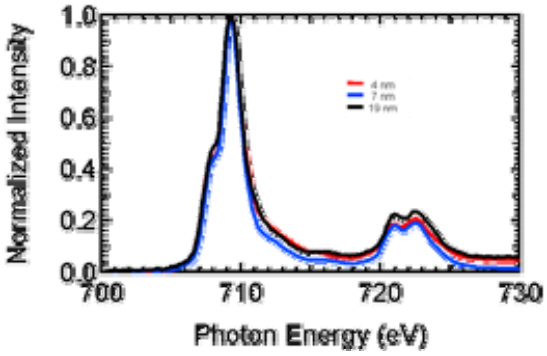

Figure 5.2: Iron L-edge XAS spectra of the three sizes of γ-Fe_2O_3-mineralized protein cages.

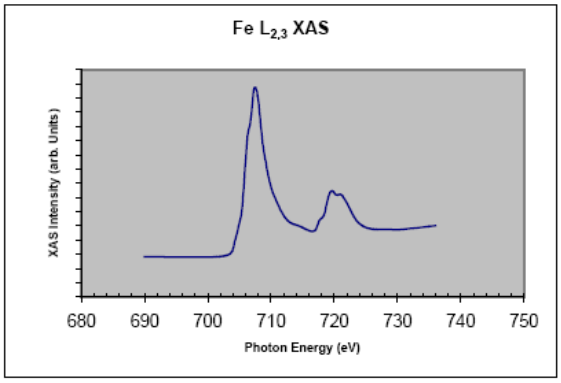

Figure 5.3: Iron L-edge XAS spectrum of bulk magnetite.

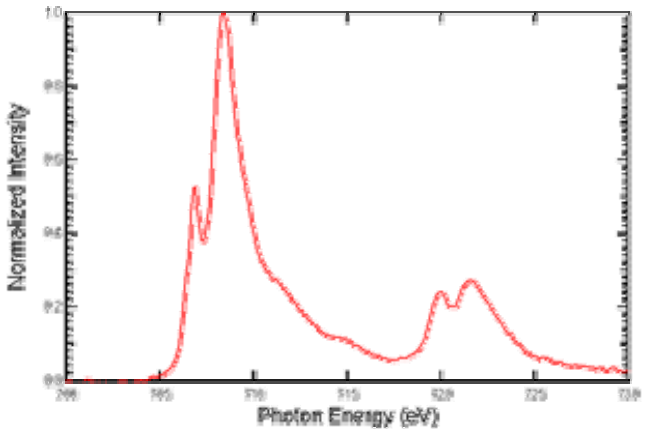

Figure 5.4: Iron L-edge XAS spectrum of native cow spleen Fn.

of hard materials. Scans were done in electron yield after precipitating samples and placing them on a copper paddle. Each sample was scanned multiple times while observing the Fe L3 and L2 edges in a range from 700 to 730 eV. Figure 5.2 shows the spectra obtained for the three samples, in these scans there are no glaring differences between the three different sizes of particles[153]. An interesting feature to note is the pre L3 edge feature, which appears as a shoulder. This feature is not present in bulk magnetite (Figure 5.3) however has been seen in ferrihydrite samples prepared in native ferritin (Figure 5.4).

Vibrating Sample Magnetometry

VSM probes how a material responds to a magnetic field. As a DC magnetic field is applied, the sample is magnetized and vibrated relative to a detection coil which measures variations in flux of the magnetized particles. Among the properties that can be measured using this technique are saturation magnetization M_s and coercive fields. Coercive fields vary drastically with respect to temperature. For the smallest 4 nm particle, the blocking temperature is around 5 K (measured at 1000 Hz), so in order for

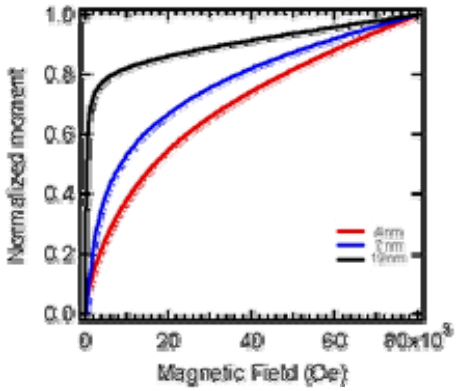

Figure 5.5: Initial magnetization curves for 4, 7, and 19 nm γ-Fe_2O_3-mineralized protein cages.

there to be any coercive force the hysteresis loop would have to be measured at less than 5 K. This is not feasible, but sufficed to say that the coercive field of magneto LDps is always less than the 7 and 19 nm systems. The saturation magnetic moments can be measured and adequately compared for these three sizes of systems, but the results are still poorly understood due to the small size of these particles and the potentially non-Langevin behavior of the systems[154]. The magnetic moment is considered to be saturated when the entire particle behaves as a single domain magnet[138]. Figure 5.5 displays the normalized saturation magnetic moments of these three sizes of systems. The unnormalized M_s moments per particle differ by less than expected. If these particles behaved with bulk properties, it would be expected that the M_s would increase with volume (radius cubed), however in these systems, the smaller particles actually have a larger surface contribution to the M_s thus making them have a larger M_s with respect to the larger particles. While the overall M_s per particle increases for the three sizes of particles, the moment per iron atom decreases; probably due to a decrease in the uncompensated spins that are present along the surface of the particles.

Alternating Current Magnetic Susceptibility (ACMS)

AC magnetic susceptibility is a dynamic measurement that is used to probe the susceptibility of a material to align with an alternating magnetic field (amplitude = 10 Oe). The measurement is based on an energy barrier between aligning with the field vs. aligning against the field when the 10 Oe field is applied. ACMS is a measurement of dynamic magnetic properties and changes with respect to temperature and measurement frequency. The blocking temperature T_b is the temperature where the energy barrier (E_a) between flipping spins (magnetic anisotropy energy) is equal to the thermal energy of the system. In all scans the initial temperature was set to well above the T_b, usually 300 K and taken down to 5 K while measuring ACMS at several different frequencies, the 4 nm sample was measured down to 3 K since the T_b is so low (Figure 5.6). In Figure 5.6 the imaginary component of the magnetic susceptibility (this is the out of phase susceptibility) is plotted as a function of temperature for the three mineralized cages. The

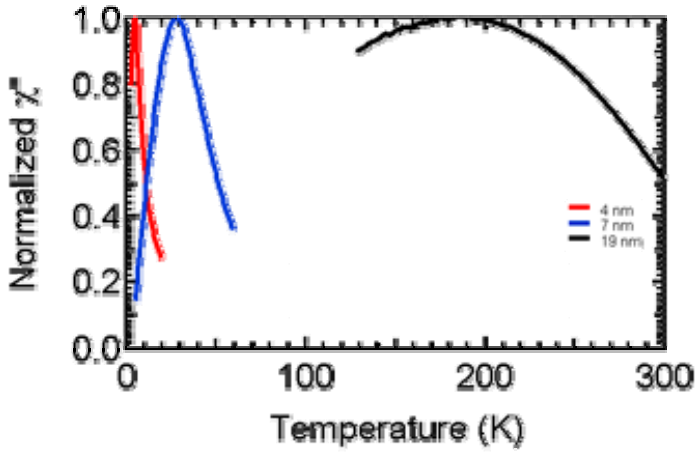

Figure 5.6: Comparison of the normalized imaginary components to the susceptibility of the different sizes of mineralized protein cages.

intensities of all three measurements were normalized to one and the frequency of measurement was 1000 Hz. For these mineralized protein cage samples the blocking temperatures were determined to be 5 K for LDps (4 nm), 29.5 K for Fn (7 nm) and 183

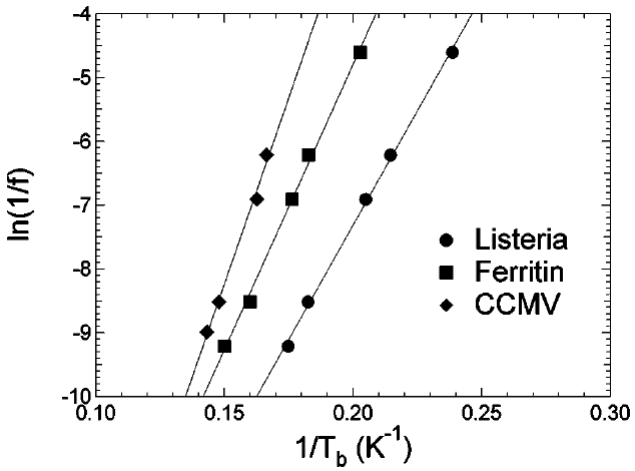

Figure 5.7: Neel-Arrhenius plots showing the frequency dependence (1/n) vs. blocking temperature ($1/T_b$) of the mineralized protein cages [154].

K for XSubE (19 nm)[154]. One of the advantages to synthesizing maghemite inside the protein cage systems is that the particles are completely isolated from each other as determined by a Néel-Arrhenius (NA) plot of ln (frequency)$^{-1}$ vs. $1/T_b$ (Figure 5.7)[139]. The equation for the NA plot is given in equation 5.1:

$$Ln(1/f) = (1/\Gamma_0) + \frac{E_a}{k_b T_b} \tag{5.1}$$

Where f is the frequency of ACMS measurement, Γ_0 is the average attempt frequency, $\frac{E_a}{k_b}$ is the average anisotropy energy, and T_b is the blocking temperature. The NA plot gives a relationship between the blocking temperature and the frequency of measurement and the linear shape to this plot indicates that the protein cage isolates the magnetic

particles from each other preventing any interaction. The y intercept of the NA plot corresponds to the average attempt frequency (a component of the material synthesized) and the slope of the line gives a value to the average anisotropy energy (E_a) (a size dependent component of the material synthesized) [139, 154]. The average anisotropy energy of the material can be related to the volume of the material synthesized and can further be broken down to two components that contribute to the anisotropy energy, a bulk component and a surface component using equation 5.2:

$$E_a = K^{eff}V = K_bV + K_s(d)A \quad (5.2)$$

Where E_a is the activation energy, $K^{eff}V$ is the effective anisotropy energy * volume, K_bV is the value of anisotropy energy for bulk magnetite * volume, and $K_s(d)A$ is the surface component, dependent on the diameter and surface area of the particles. Figure 5.8 shows a plot of anisotropy energy density as a function of the surface of the materials, it is clear that as the particles decrease in size (increase in curvature) there is a deviation from bulk properties.

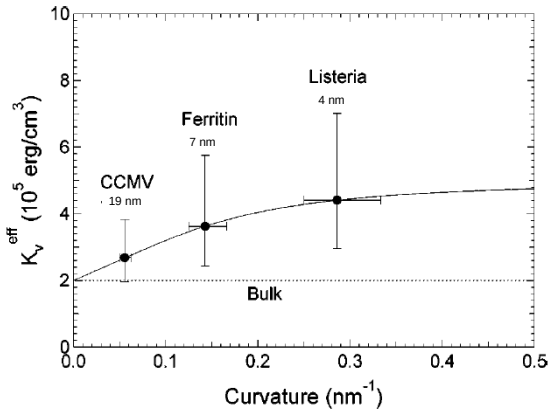

Figure 5.8: Plot of average particle anisotropy density (K_{eff}) vs. particle curvature [154].

Electron Magnetic Resonance (EMR)

Electron paramagnetic resonance spectroscopy (EPR) is a dynamic measurement similar to ACMS and probes the resonance energy of a free electron in a magnetic field. Typically electrons in a system have no preference for pointing in one direction or another (spin up or spin down), however as an external magnetic field is applied there is a separation in the population of states and it becomes favorable for the electrons in a system to point in either the same direction as the applied magnetic field, or to point in the opposite direction. Much like in NMR there is a slight favorability of the electron spin to align with the applied magnetic field. This difference in energy between causes two populations of states (either aligned or anti-aligned with magnetic field) which is separated by a resonance energy. The resonance energy can be overcome by a very small

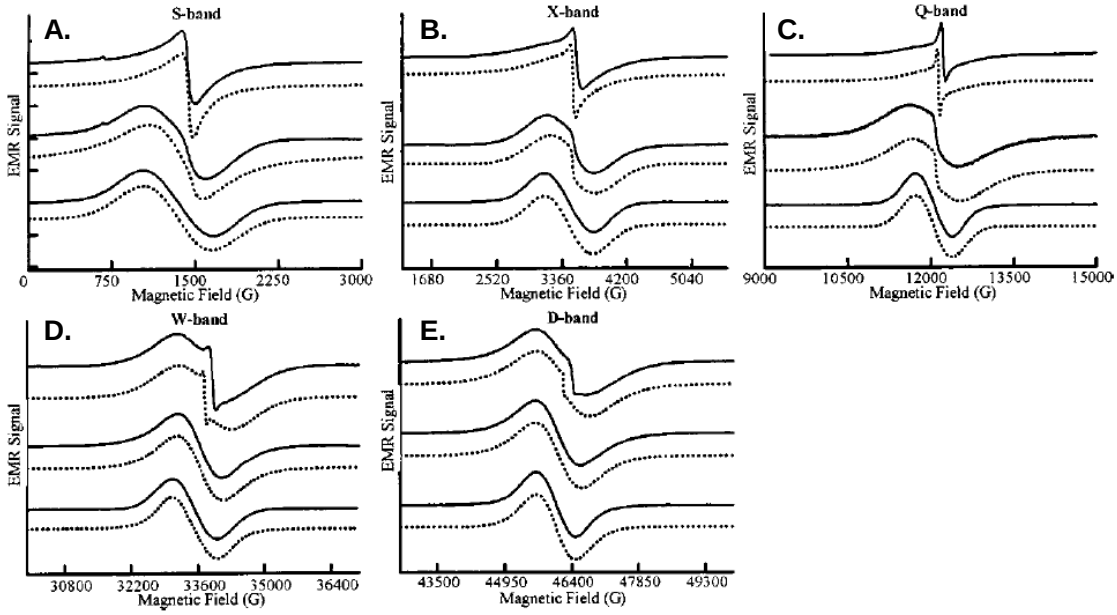

Figure 5.9: EMR spectra of the three sizes of protein cages (top = 4 nm (LDps), middle = 7 nm (Fn), bottom 19 nm (SubE)) plotted at five different frequency bands A. S-band (4 GHz), B. X-band (9.8 GHz), C. Q-band (34.6 GHz), D. W-band (94.9 GHz), E. D-band (130 GHz) [155].

amount of radio or microwave radiation that can be used to excite the electron from aligning with the field to the slightly higher anti-aligned state. When EPR is measured on a material based system that has a group of unpaired electrons (i.e. a ferromagnetic, ferrimagnetic, or superparamagnetic material) the technique is known as electron magnetic resonance (EMR) but can still be used as a dynamic measurement that probes the overall spin of the material. For the mineralized protein cages there is a spin component to each particle because of the favored directionality of the ferrimagnetic particle.

The research of Usselman *et al.* has reported a detailed modeling study of the size dependent magnetic behavior of the maghemite mineralized protein cages[155]. The current discussion will be limited to two components of each EMR spectrum, a broad component (corresponding to bulk magnetic properties) and a narrow component (corresponding to surface properties). The EMR line shape is dependent on several components, most commonly probed are temperature, frequency of measurement, and material size (volume). Figure 5.9 shows a comparison of room temperature EMR measurements taken at several different frequencies[155]. Each plot corresponds to the three sizes of minerals studied, 4 nm, 7 nm, and 19 nm. Each line shape indicates a strong dependence on the size of the particle measured as well as the frequency measured. The narrow component to each spectrum increases as the size of the particles decrease, or as the frequency of measurement decreases. This further confirms the results of the ACMS size comparison of surface anisotropy energy density as shown in figure 5.8, the

larger particles behave more like bulk materials, while the smaller ferrimagnetic particles show greater deviation from bulk while maintaining a smaller bulk component.

Conclusion

The size dependent characteristics for three different protein cages mineralized with ferrimagnetic nano-particles of maghemite or magnetite show similarities and differences. The structural and electronic properties of the minerals showed identical results within the limits of measurement. Electron diffraction measurements indicate that the structural phase of the minerals inside the three protein cages is identical and indistinguishable from the calculated d-spacing values for Fe_3O_4 and γ-Fe_2O_3. XAS shows no significant difference between the electronic properties of the three sizes of minerals when probing the iron L edge. All magnetic characterizations performed show that the nano-particle based systems diverge from properties of bulk materials and that the divergence increases as particle size decreases. These divergences are probably due to the fact that most iron incorporated into nano-particles in this size regime (4-20 nm) are at the surface and their properties can not be approximated by bulk measurements.

METAL BINDING TO COWPEA CHLOROTIC MOTTLE VIRUS PROBED BY FLUORESENCE RESONANCE ENERGY TRANFER (FRET)

Introduction

In biological systems metals are known to play multiple roles for enzymatic activity, electron transport, signaling and structure, among other functions. The assembly of supramolecules is often mediated through direct binding of metal ions at some intersubunit interface in order to enable favorable interaction to form the noncovalent bonds that hold multiple subunit structures together. Many viruses require metal ions to be present in order to drive the assembly of the viral coat protein. Southern bean mosaic virus (SBMV), for instance, requires the presence of relatively high concentrations of both magnesium and calcium in order to assemble the viral capsid and has been isolated from infected southern bean plants coordinating approximately 110-130 Mg^{2+} ions and 75-100 Ca^{2+} ions. If these ions are removed the viral capsid is considerably more susceptible to protease degradation. The bound Mg^{2+} and Ca^{2+} ions play an essential role in stabilizing protein-protein interactions that form the SBMV capsid[105]. In many viruses bound metal ions (Ca^{2+} or Mg^{2+}) may mediate processes of infection, controlled disassembly, assembly, and many structural transitions in the viral capsid. Many viruses have shown discreet structural transition in the assembled virion that are caused either by changes in pH or by metal ion concentration. As mentioned in chapter one, CCMV undergoes a process of swelling that is pH and metal ion dependent. This phenomenon of virus swelling was first observed in the bromegrass mosaic bromovirus[156], but has been

observed in many other viruses since[99, 157-159]. Since viruses, in general, are metastable structures that are designed to transport nucleic acid through many different environments, metal binding and the associated structural transitions that go along with those may be a way of coping with those environments.

Many proteins that require binding of metal ions, either for structure or functional purposes, have properties that can be studied using spectroscopic techniques. For instance metallo proteins that perform enzymatic or redox function usually have excited states that can be accessed spectroscopically or by using other techniques. Proteins that bind alkali earth metals do not have the advantage to be probed using these techniques because of the lack of valence electrons, which makes them magnetically and spectroscopically silent. A way around this fact is to isomorphously replace the endogenous metal ion with one of similar ionic radius and bonding properties which will have spectroscopic signatures that can be probed. Ca^{2+} and Mg^{2+} are similar in that they are hard ions with similar ionic radii, they both prefer oxygen ligands (either charged or uncharged) to nitrogen and sulfur ligands and they both have the capacity to have multiple coordination numbers (typically between six and eight coordinate). Ca^{2+} binding proteins are of particular interest because of their commonality and the universal presence of Ca^{2+} *in vivo*.

The effective ionic radius of Ca^{2+} varies between 1.00 Å to 1.12 Å for six and eight coordinate environments (Table 6.1)[111, 112]. This is similar to the ionic radii of the lanthanides which vary across the row from 0.85-1.06 Å for six coordinate to 0.97-1.18 Å for eight coordinate environments. One obvious difference between Ca^{2+} and Ln^{3+} is that

Table 6.1: Effective ionic radii of various metals in Å.

Atomic number	Ion	Coordination	Number
		6	8
47	La3+	1.06	1.18
60	Nd3+	1	1.12
20	Ca2+	1	1.12
65	Tb3+	0.92	1.04
71	Lu3+	0.85	0.97
12	Mg2+	0.72	0.89

there is the clear charge difference, which typically causes Ln^{3+} to substitute into Ca^{2+} binding proteins with a higher affinity. Apart from La^{3+} and Lu^{3+}, all other lanthanides have unpaired f electrons that allow for the possibility of probing their properties using spectroscopic methods. One Ln^{3+} that has gained particular interest for studying Ca^{2+} binding is the ion Tb^{3+} through a luminescent technique called Forster or fluorescence resonance energy transfer (FRET). As can be seen in table 3.1, the ionic radius of Tb^{3+} differs from Ca^{2+} by 0.08 Å for both six and eight coordinate. This small difference in ionic radius has been shown to not be significant to metal binding to protein and has been confirmed to bind isomorphously the Ca^{2+} ion in a number of Ca^{2+} binding protein systems by X-ray diffraction studies[111].

It would be expected that all of the lanthanides with free f electrons could be used as a probe using absorbance spectroscopy, however the molar absorbtivities (ε) of all the lanthanides is so small that changes in the ligand field is only detectable by most absorbance spectrophotometers at concentration greater than 10 mM[111]. The technique of FRET; however, allows for the study of metal binding in the nM - μM range. FRET requires the absorbance by the aromatic sidechain of the FRET donor molecule in the near UV region followed by the non-radiative energy transfer from the donor molecule in close proximity to the Tb^{3+} accepter ion through either a Forster or Dexter type

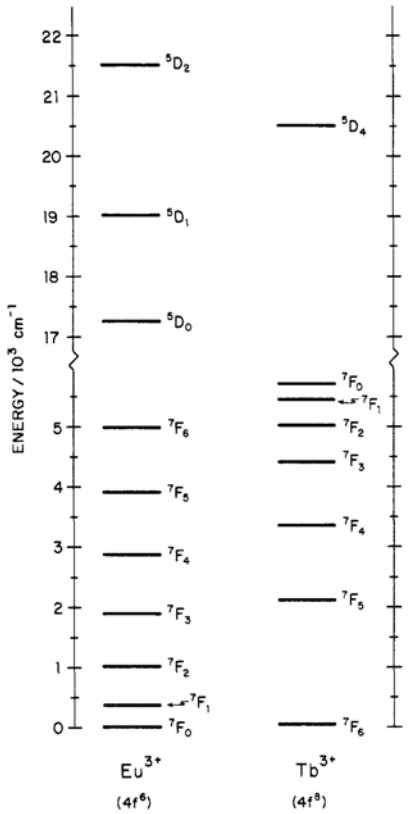

Figure 6.1: Energy level diagram for the excited states of two luminescent lanthanides, Eu^{3+} and Tb^{3+} [112].

mechanism (depending on the energy transfer distance)[160] then the emission of the Tb^{3+} ion in the region of 535-555 nm which is assigned to the $^5D_4$-$^7F_5$ phosphorescence transition (Figure 6.1)[112]. Several different donor molecules have been used for studying FRET to Tb^{3+} ranging from the aromatic amino acids of proteins to several aromatic chelating molecules[161]. Of the aromatic amino acids that can be used as donor molecules, Tryptophan has been shown to give the most efficient energy transfer to Tb^{3+} in close proximity to the Trp molecule followed by Tyr, then Phe[161].

Brittain *et al.* have used Tb^{3+} to probe the Ca^{2+} binding affinity of 36 different Ca^{2+} binding proteins. In their study they confirmed that of the 36 proteins were

investigated, only four of them did not yield an observable FRET when Tb^{3+} was bound[111]. Other studies have been performed on the Ca^{2+} binding motifs (EF and CD hand motifs) from different oncomodulin and calmodulin proteins[161, 162] in order to engineer proteins with high affinities for Ca^{2+} or lanthanides with desirable magnetic

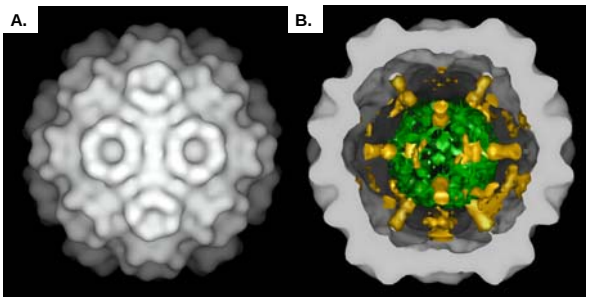

Figure 6.2: A. 3D Cryo EM reconstruction of CCMV, B. Cutaway showing the interior of CCMV with nucleic acid packaged [25].

properties. Most Ca^{2+} binding protein systems are adequately studied by exciting the endogenous aromatic amino acids in the near UV range (260-300 nm) and observing the loss of either Trp, Tyr, or Phe fluorescence (300-350 nm) as Tb^{3+} is titrated in and binds in close proximity to these amino acids and fluoresces in the green area of the spectrum (535-555 nm).

Although viruses often require metals, particularly for virus assembly, there are very few studies that have quantitatively determined the metal binding affinity of the virus for metal ions. We have used FRET as a probe the metal binding affinity of three forms of CCMV. CCMV is a small plant virus that is a member of the *Bromoviridae***.** Among the attributes that distinguish this class of plant viruses is that they encapsulate a tripartite genome that consists of three unique, single-stranded, positive-sense RNA molecules that are encapsulated independently of each other in separate viral capsids[97]. The total size of the genome is about 3.2 MDa and is composed of RNA 1 (1.1 MDa),

RNA 2 (1.0 MDa), and RNA 3 (0.75 MDa); there is a fourth RNA molecule that is packaged in the same capsid as a subgenomic RNA of RNA 3 called RNA 4 (0.35 MDa)[163]. The viral capsid (Figure 6.2A) that encapsulates these RNA molecules (figure 6.2B) is composed of 180 chemically identical subunits with a molecular mass of 20.2 KDa (figure 6.2C). These 180 subunits self-assemble both *in vivo* and *in vitro* to form a 28-30 nm exterior diameter protein cage with icosahedral (532) symmetry. It has been shown that the positively charged N-terminus of the virus is responsible for encapsulating the viral nucleic acid. If the first 25 amino acids (containing several positively charged lysine and arginine amino acids) are deleted from the viral capsid, it is not capable of encapsulating viral nucleic acid however if only the first seven amino acids (not containing positive charge) are deleted the virus still forms infectious particles that exhibit symptoms of the native virus infection in the plant host[97].

CCMV was the first icosahedral virus reassembled *in vitro* from purified virus subunits and RNA to form infectious virus particles[99]. CCMV has been the focus of multiple biochemical studies for nearly 40 years for the purpose of determining protein/RNA interactions[164, 165], supramolecular self-assembly[166, 167], X-ray structure determination and cryo-electron microscopy three dimensional reconstruction[25, 97], as a mode of studying heterologous expression[102], and more recently as a scaffold for chemical modification for material synthesis, cell targeting, drug and therapeutic delivery, and organic marker functionalization[168].

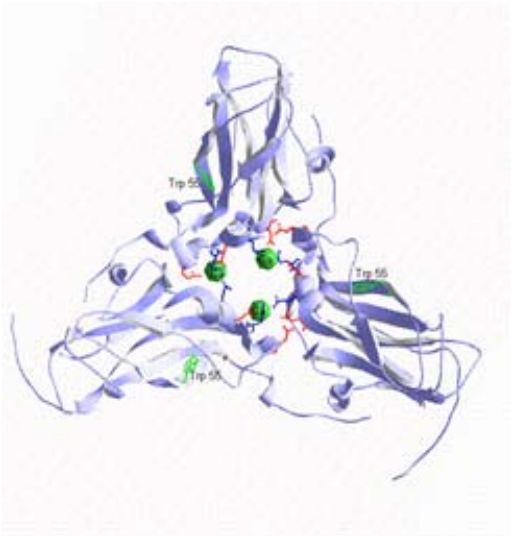

Figure 6.3: Metal binding site, E81, E148, D153 sidechains shown in red, Q85, Q149 shown in blue and the FRET donor W55 shown in green, Ca^{2+} ions are modeled into the binding site.

CCMV has been shown to require the presence of divalent cations for assembly and infection. The quasi three-fold axis is clearly where the largest structural change occurs in the pH and metal ion dependent mechanism of virus swelling as determined by cryo-electron microscopy[25]. This quasi three-fold axis contains three intersubunit clusters of acidic amino acids. When the pH is taken above 7 and there are no metal ions around then the entire virus undergoes a structural transition where the structure swells by roughly 10 percent linearly. This swelling is a reversible process that is caused by the electrostatic repulsion of these clusters of acidic residues when they are either deprotonated and when there are no metals bound to these sites. If the pH is taken above 7 and Ca^{2+} is added to the solution then the structure will relax back to its stable unswollen state caused by a shielding or removal of the negative charge at the quasi three-fold axis. The swollen virus is more susceptible to protease and RNAse degradation due to the large pores in the capsid giving free molecular access to the

genome. The structure of these swollen viral capsids and the metal ion dependent swelling indicates that the metal binding site is at this cluster of negatively charged amino acids. The presence of these metal binding sites were postulated after solving the structure of the virus in 1995[25, 101]. The metals were not observed in the X-ray structure of the virus due to the crystallization conditions (pH 3.3 and in the presence of EDTA)[25]. From the structure Ca^{2+} ions were modeld to bind at the quasi three-fold axis to five proposed amino acids (E81, Q85, E148, Q149, D153) making the metal binding site (Figure 6.3)[39]. These amino acids are located on two different subunits but since there are three binding sites at the quasi three-fold axis, there is one metal binding site per virus subunit.

Three forms of CCMV were studied by FRET in order to gain insight into the metal binding affinity as well as modes of metal binding. Wild type CCMV (wtCCMV) was studied with viral nucleic acid packaged inside the virus, the metal binding affinity of wtCCMV was determined for the spectroscopically relevant Tb^{3+}, the biologically relevant Ca^{2+}, and potentially medically relevant Gd^{3+}. These studies were done both under metal free buffer conditions as well as under biologically relevant [Ca^{2+}] concentrations of 1.5 mM. The wtCCMV bound to Gd^{3+} was also pursued as a potential high contrast MRI agent. Two mutant forms of CCMV were analyzed in order to gain insight into the mode of metal binding, these two mutants are not capable of packaging nucleic acid; which is known to have an interaction with Ca^{2+}. One mutant, termed subE, has had eight basic amino acids on the N-terminus (K8, K20, K22, R11, R14, R15, R19, R23) changed to glutamic acid[36]. These changes made for the interior surface of the

assembled virus like particle (VLP) to have an overall negative charge making it incapable of packaging viral nucleic acid but can be isolated as a self assembled virus like particle from a heterologous expression system of *Pichia pastoris*. The second mutant that was studied is one that has had the five amino acids (E81, Q85, E148, Q149, D153) changed to threonine termed the metal binding site deletion mutant (mbsD). mbsD is also not infectious so can not package native nucleic acid, but can be isolated from the same *Pichia pastoris* system as subE.

Materials and Methods

Making the Mutations to Form SubE and MbsD

Site directed mutagenesis was performed on CCMV nucleic acid in order to form the two mutants of interest, in subE eight N-terminal amino acids (K8, K20, K22, R11, R14, R15, R19, and R23) were altered to the acidic glutamic acid (E), for the mbsD five amino acids (E81, E143, D153, Q84, and Q149) were altered to threonine. These mutations were done using QuikChange site-directed mutagenesis (Stratagene, La Jolla, CA).

Isolation of VLPs

Since wtCCMV contains viral nucleic acid and is infectious, it was isolated from infected cowpea plants using methods published previously. Briefly outlined, 100 g of infected cowpea leaves were ground in a blender then the virus was purified. After breaking up leaves using a blender wtCCMV was purified using the same method as the other mutants. The subE and mbsD mutants were isolated from a heterologous yeast

expression system[102]. 100 g of yeast containing the VLPs were homogenized in a bead beater before being isolated similar to the wtCCMV.

Purification of the VLPs

After lysing both the cowpea plant cells and the yeast cells containing VLPs the cells were spun slowly in a centrifuge to remove most of the cell material. The supernatant was then spun at 25000 X g to pellet the virus. The virus was resuspended and purified using a 39% (w/v) CsCl density gradient spinning at 38000 X g and the virus band was collected and dialyzed into acetate buffer (100 mM acetate, 10 mM EDTA pH 4.8). Further purification was accomplished by size exclusion chromatography (SEC) (ÄKTA 900) using a gel filtration column (Amersham Biosciences Superose 6 10/300). Purity was confirmed by SDS-polyacrylamide gel electrophoresis. The VLP were confirmed to be assembled using dynamic light scattering (DLS) (ZetaPALS, Brookhaven instruments), and negatively stained (1% uranyl acetate) TEM. The protein concentrations were determined by biuret and Bradford protein assays.

Fluorescence

All fluorescence experiments were performed on a SPEX Fluorolog spectrophotometer at 25 ^{o}C. Excitation and emission slit widths were set to 4 and 8 nm respectively. The excitation wavelength was set to 295 nm and the fluorescence was measured from 308 nm to 580 nm at 1 nm resolution with 0.5 seconds integration time on each point and another scan was done from 520-570 nm at 0.2 nm resolution and 0.5 seconds integration time. The λ_{max} for Trp emission is 330-342 nm, after the Tb^{3+} binds

to the virus the λ_{max} for Tb^{3+} is 542-544 nm. Before running fluorescence stock solutions of Tb^{3+} were prepared either from $Tb(NO_3)_3$ in doubly deionized water prepared through a nanopure system to (18 MΩ resistivity) or by diluting a purchased ICP standard into pH 6.5 buffer (50 mM MES 100 mM NaCl). The concentrations of stock solutions as well as the working solutions of Tb^{3+} were confirmed using inductively coupled plasma atomic emission spectroscopy (ICP AE). The fluorescence experiments were performed on 2 mLs of purified VLP prepared in pH 6.5 buffer (50 mM MES 100 mM NaCl) at concentrations of 2 μM and 5 μM of virus subunit. Several aliquots of metal were added to the virus solutions in order to probe the Tb^{3+} binding affinity of the virus. FRET from tryptophan to bound Tb^{3+} resulted in a typical Tb^{3+} emission where the 544 peak ($^5D_4 \rightarrow {}^7F_5$) was monitored.

For competitive binding experiments stock solutions of Ca^{2+} and Gd^{3+} were prepared either from salts of $CaCl_2$ and $GdCl_3$ prepared in doubly deionized water to (18 MΩ resistivity) or from purchased ICP standards (Aldrich) prepared in pH 6.5 buffer (50 mM MES 100 mM NaCl).

For binding experiments in the presence of biologically relevant concentration of Ca^{2+} the buffer used in the experiment was 50 mM MES, 100 mM NaCl, and 1.5 mM $CaCl_2$ at pH 6.5.

Data Analysis and Determination of Dissociation Constants

After collecting the fluorescence spectra, the spectra were baseline corrected using Igor pro (Wavemetrics corporation) by applying a poly fit to the graphs after deleting points that contained peaks and curvature. After baseline correcting the data and

peaks were fit using a Gaussian line shape around the 342 nm peak for Trp fluorescence and the 544 peak for Tb^{3+} fluorescence. We have made the underlying assumption that all 180 sites are invariant, with identical affinities and that upon saturating the metal binding sites there is one metal per VLP subunit. This allows us to use a simple single-site model to determine the fraction of CCMV that had bound Tb^{3+} (ϕ) where ϕ is related to the Tb^{3+} fluorescence intensity by the formula $\phi = I_{545} / I_{545}^{\max}$ or to the decrease in Trp fluorescence by the formula $\phi = (I_{342}^{0} - I_{342}) / (I_{342}^{0} - I_{342}^{\min})$ where I_{545}, I_{342} are the fluorescence at 545 nm and 342 nm respectively, $I_{545}^{\max}$, I_{342}^{0}, and $I_{342}^{\min}$ are the highest fluorescence of Tb^{3+} after saturating the metal binding sites with Tb^{3+}, the initial Trp fluorescence before adding Tb^{3+}, and the minimum Trp fluorescence after saturating the metal binding sites with Tb^{3+}. After seeing these relationships the dissociation constant can be determined using equation 6.1:

$$I = \frac{I_{545}^{\max}[Tb^{3+}]_F}{[Tb^{3+}]_F + K_d^{Tb^{3+}}} \quad \text{(Eq 6.1)}$$

Where I is the Tb^{3+} emission at a particular Tb^{3+} concentration, $I_{545}^{\max}$ is the maximum limit of Tb^{3+} emission after saturating all metal binding sites with Tb^{3+}, $[Tb^{3+}]_F$ is the nonbound Tb^{3+} concentration after each addition and $K_d^{Tb^{3+}}$ is the equilibrium dissociation constant for Tb^{3+} binding.

After performing the metal binding experiment with Tb^{3+} a competition experiment was performed in order to determine the dissociation constant for either Ca^{2+} or Gd^{3+}. Aliquots of either Ca^{2+} or Gd^{3+} were added to the Tb^{3+} saturated virus solution

and the apparent dissociation constants for the competing metal ions were determined using equation 6.2[38]:

$$I = \frac{I_{\max} K_{app}^{xx}}{K_{app}^{xx} + [XX]} + I_0 \quad \text{(Eq. 6.2)}$$

Where K_{app}^{xx} is the apparent equilibrium dissociation constant for the competing metal either Ca^{2+} or Gd^{3+} in the presence of Tb^{3+}, $[XX]$ is the concentration of either Ca^{2+} or Gd^{3+} concentration and I_0 is the Tb^{3+} fluorescence at infinite concentration of the competing metal ion. The equilibrium dissociation constant for the competing metal was determined by applying equation 6.3:

$$K_d^{xx} = \frac{K_{app}^{xx}}{1 + \frac{[Tb^{3+}]}{K_d^{Tb^{3+}}}} \quad \text{(Eq. 6.3)}$$

Relaxivity Measurements on Gd^{3+} CCMV

After determining the dissociation constant for Gd^{3+} using competitive binding experiments solutions of wtCCMV were saturated with Gd^{3+} and relaxometry measurements were performed[38, 169]. A solution of 200 μM Gd3+ (from $GdCl_3$) and 114 μM (2.3 mg/mL) CCMV subunit were prepared in pH 6.5 buffer (50 mM Hepes, 150 mM NaCl). As a control 200 μM Gd^{3+} was prepared and run in the same buffer. Using a custom-designed variable field relaxometer, the T_1 was measured using a saturation recovery pulse sequence with 32 incremental τ values. T_2 was measured using a CPMG pulse sequence with 500 echoes and an interecho time of 2 msec. The range of Larmor

frequencies was 2-62 MHz (H = 0.05 - 1.5 Tesla) and the measurement temperature was 23 °C.

Since the T_1 and T_2 relaxivities are expressed in units of $mM^{-1}s^{-1}$ it was necessary to determine the fraction of CCMV that had bound Gd^{3+}. Toward this end, two methods were used. One method determined the fraction bound using a calculation involving the concentrations of CCMV and Gd^{3+} and the dissociation constant for Gd^{3+} determined by FRET experiments. The second method is a colorimetric Gd^{3+} assay[170] that allowed for the independent quantification of Gd^{3+} that was bound to the CCMV after separating the Gd^{3+}-CCMV from free Gd^{3+} using a Micro Bio-Spin column.

The concentration of Gd^{3+} bound to CCMV in the relaxivity experiment was calculated by determining the fraction of CCMV that had bound Gd^{3+} (θ) using equation 6.4[162]:

$$\theta = \frac{[(K_d^{Gd^{3+}} + [site] + [Gd^{3+}]) - \sqrt{(K_d^{Gd^{3+}} + [site] + [Gd^{3+}])^2 - (4 * [site] * [Gd^{3+}])}]}{(2[site])} \quad \text{(Eq 6.4)}$$

Where $K_d^{Gd^{3+}}$ is determined from equation 6.3, [*site*] is the concentration of metal binding sites (114 μM) and the $[Gd^{3+}]$ is 200 μM. In close agreement to this calculation, the colorimetric assay for detection of Gd^{3+} used the chemical arsenazo III[170]. In order to perform this measurement, Gd^{3+}-CCMV was separated from free Gd^{3+} using a Micro Bio-Spin 30 chromatography column (BioRad). A solution of 114 μM CCMV was incubated in 200 μM Gd^{3+} for 30 minutes in pH 6.5 buffer (40 mM Hepes, 150 mM NaCl). The Micro Bio-Spin 30 columns were buffer exchanged into this same pH 6.5 buffer according to the method provided. 60 mL of each sample (Gd^{3+}-CCMV

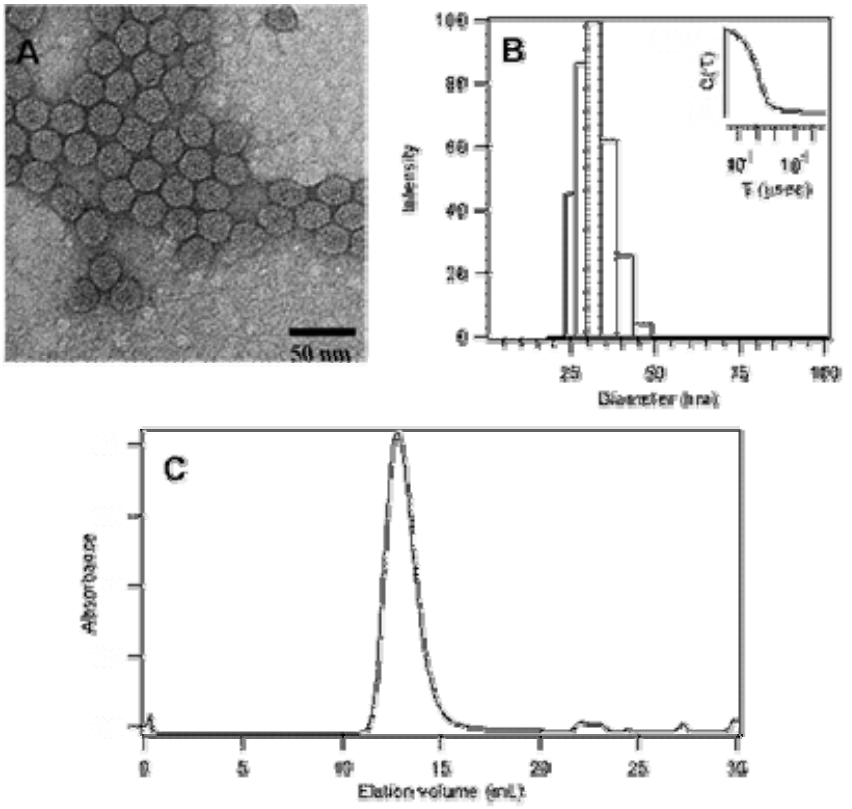

Figure 6.4: A. Negative stain TEM, B. SEC, and C. DLS of assembled wtCCMV.

and a protein free control) were loaded onto each of two columns and the Gd^{3+}-CCMV was separated from free Gd^{3+} by spinning the columns at 1000 X g for 4 minutes. After separation, the flow-through volume was determined and the concentration of Gd^{3+} was checked using a colorimetric assay (0.005% Arsenazo III pH 3.0) (Aldrich). This was done by first adding 5 μL of 50 mM HCl to each flow-through in order to confirm that the Gd^{3+} was released by the CCMV. The CCMV containing solutions were diluted 10 and 20 fold in pH 3.0 buffer (100 mM formate). The [Gd^{3+}] was then determined colorimetrically (50 μL sample, 50 μL color reagent). After the test, the solutions were confirmed to be pH 3 with pH paper.

Results and Discussion

All metal binding studies were performed on purified wild type virus and VLPs that were assembled into 28 nm protein cages as determined by negatively stained TEM, DLS, and SEC (Figure 6.4). WtCCMV, subE and mbsD all have an endogenous tryptophan residue (W55) that is located approximately 1.5 nm from the putative metal binding site. This provides an ideal geometry for using FRET to probe metal binding at this site (Figure 6.3). Upon excitation of W55 at 295nm, energy transfer to the fluorescent lanthanide ion, Tb^{3+}, was observed when it occupied the metal binding site. Thus, by monitoring the increase in Tb^{3+} fluorescence (545 nm), and concomitant loss of Trp fluorescence (350 nm), as a function of added Tb^{3+}, we have probed the metal binding characteristics of this site. The resulting hyperbolic binding isotherms have been modeled to yield a dissociation constant for Tb^{3+} binding to the putative binding sites. On the wtCCMV system, after determining the K_d for Tb^{3+} binding at the metal binding site other cations were added to competitively bind to the metal binding site; these gave apparent binding constants for Ca^{2+} and also for Gd^{3+}.

WtCCMV has two potential modes of metal binding; including the metal binding site at the quasi-three fold axis and the phosphate backbone of the viral nucleic acid. Tb^{3+} binding to wtCCMV was measured at pH 6.5 with a protein concentration that varied from 2-7 μM subunit. Upon exciting the solution at 295 nm the fluorescence spectrum was measured from 308 to 580 nm. Fluorescence of the endogenous Trp was monitored at 340nm after adding aliquots of Tb^{3+} there was a decrease in the emission at 350 nm while there was an increase in a peak due to Tb^{3+} bound at the metal binding site that was monitored at 545 nm (Figure 6.5). Eventually the metal binding sites are saturated with Tb^{3+} and the emission spectra no longer change. The decrease in emission at 340nm as well as a concomitant increase in the emission at 545nm was monitored as a function of total Tb^{3+} added to the solution. The emission intensities at 340 nm and 545

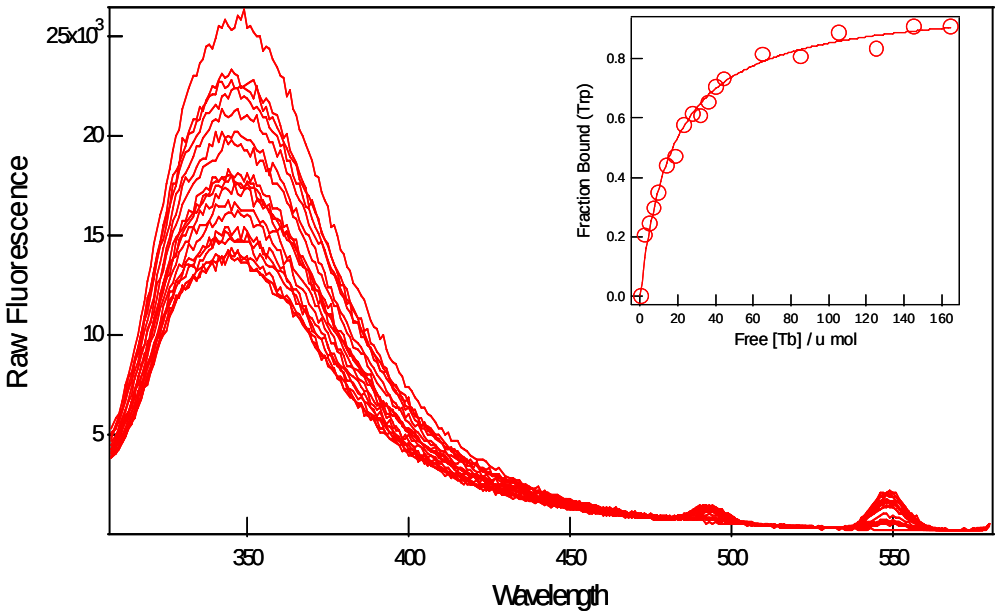

Figure 6.5: Fluorescence spectra from ranging from 308-580 for wtCCMV, the Trp fluorescence (340 nm) decreases as Tb^{3+} is titrated in and binds to the metal binding site, Inset: Binding isotherm showing the normalized increase in Tb^{3+} fluorescence.

nm were then fit to a rectangular hyperbolic curve to yield binding isotherms depicting the fraction of Tb^{3+} bound at the metal binding site for both the decrease in emission intensity for 340 nm and the increase in 545 nm (Figure 6.5B). Using equation 6.1 it was determined that the K_d for Tb^{3+} is 19 μM.

To separate the contribution of the protein binding sites from the nucleic acid binding sites, we examined the Tb^{3+} binding in the absence of any viral nucleic acid. This was accomplished by taking advantage of the subE mutant. The subE VLP is indistinguishable from wtCCMV by TEM, SEC and DLS and still assembles into 28 nm diameter T=3 particles (Figure 6.6). The lack of nucleic acid was confirmed by comparing the ratio of 260 nm to 280 nm absorbance. Since nucleic acid has a higher absorbance at 260 nm the wtCCMV ratio is about 1.2 while the subE ratio is about 0.7.

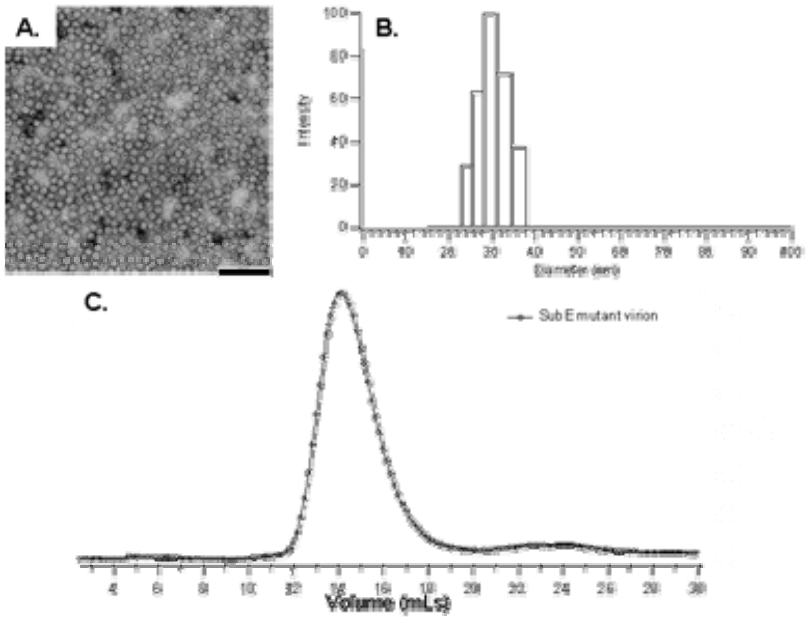

Figure 6.6: A. Negative stain TEM, B. DLS, and C. SEC of assembled SubE.

Cryo electron microscopy reconstruction has also been used to confirm that the subE does form an empty VLP since there was no electron density visible on the inside of the protein cage (Figure 6.7). Metal binding to subE was measured under the same conditions as the studies of wtCCMV and fit by the same methods. The K_d for Tb^{3+} was

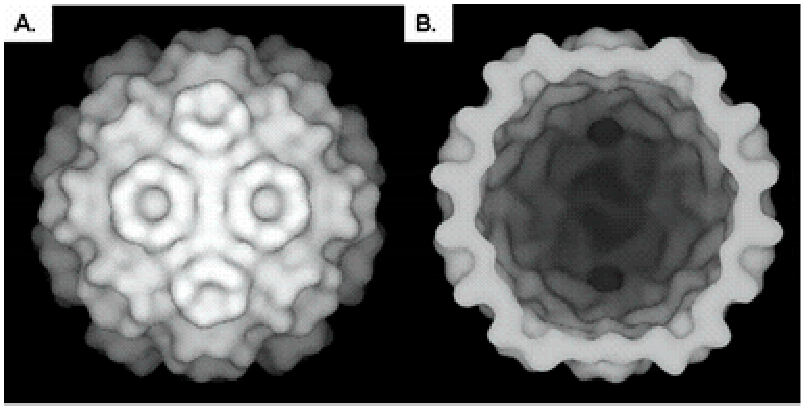

Figure 6.7: 3D cryo electron reconstruction of subE A. Entire capsid, B. Interior view.

determined to be 17 μM (Figure 6.8) as clearly seen from the binding isotherm for subE focusing on the 545 nm emission peak. This is similar to the K_d for wtCCMV indicating that viral nucleic acid has a relatively small effect on the binding of metal ions to the protein cage.

The putative metal binding site that involves amino acids (E81, Q85, E148, Q149, and D153) was first speculated in the structure paper by Speir *et al.* by comparing the cryo-reconstruction data for the swollen and closed forms of CCMV. To establish that Tb^{3+} binds specifically at these sites the Tb^{3+} dissociation constant was measured for a mutant that had all five of these amino acids changed to threonine. This metal binding site deletion mutant (mbsD) was purified and confirmed to be an intact 28 nm VLP that is indistinguishable from wtCCMV by TEM, SEC, and DLS (data not shown). The

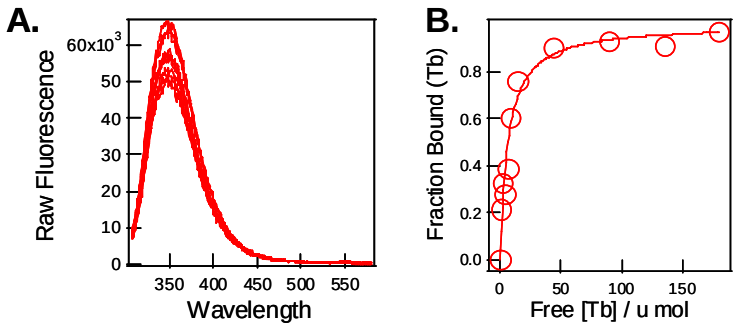

Figure 6.8: A. Fluorescence spectra and B. Binding isotherm for Tb^{3+} binding to SubE.

conditions for FRET were identical to those of both wtCCMV and subE using a virus concentration of 3 mM subunit and pH 6.5 (50 mM MES 100 mM NaCl) and FRET was measured from the energy transfer from W55 (344 nm) to bound Tb (545 nm). Binding isotherms were calculated (Figure 6.9) and from the fit we calculate a dissociation constant of 67 ± 23 μM. This decrease in binding substantiates that the Tb^{3+} is binding at the metal binding site, but there may be other amino acids involved in metal binding at that site.

Several competitive binding experiments were performed on wtCCMV for the purpose of quantifying the binding affinity of the native virus for Ca^{2+} and Gd^{3+}. All competitive binding experiments were done by saturating the metal binding sites with Tb^{3+} and then adding aliquots of either Ca^{2+} or Gd^{3+} to a final ratio of 500 cation/Tb^{3+}. As competing cation is added there is a decrease in the fluorescence from bound Tb^{3+} and the Trp fluorescence begins to increase back to the intrinsic fluorescence before adding any Tb^{3+}; this is the result of metal exchange at the metal binding site (Figure 6.10). As was expected the binding affinity was considerably lower for Ca^{2+} than for Tb^{3+} largely due to the difference in charge. After doing the competitive binding experiment we determined the K_d for Ca^{2+} to be 1.97 mM or about 100 times less than the K_d for Tb^{3+}

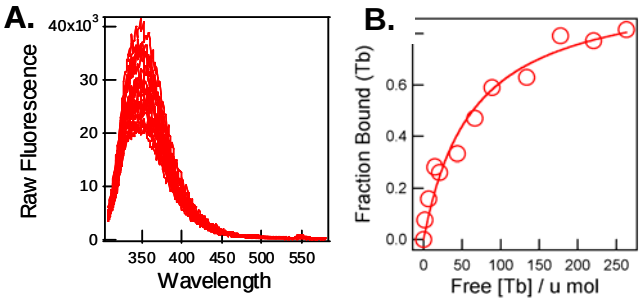

Figure 6.9: A. Fluorescence spectra and B. Binding isotherm for Tb^{3+} binding to mbsD.

(Figure 6.10B). The K_d for Gd^{3+} is nearly the same as that of Tb^{3+} at about 31 μM, which is expected based on the same charge and similar ionic radius (Figure 6.10C). Since we were studying Gd^{3+} binding for the purpose of evaluating its potential as an MR contrast agent we also performed the competitive binding experiments in the presence of a cellular concentration of Ca^{2+} (1.5 mM). The $K_d^{Tb^{3+}}$ of Tb^{3+} was determined by fitting the binding isotherm and measuring the value of 50% saturation to give a dissociation constant of 19 μM and a value of 30 μM in the presence of 1.5 mM Ca^{2+}. An equilibrium dissociation constant for Gd^{3+} binding to CCMV was determined as 31 μM by analyzing the decrease in Tb^{3+} fluorescence intensity upon addition of Gd^{3+}, the $K_d^{Gd^{3+}}$ for Gd^{3+} in the presence of Ca^{2+} was measured to be 32 μM. Since the trivalent lanthanides have a considerably higher binding affinity for CCMV than Ca^{2+} the presence of 1.5 mM Ca^{2+} had relatively little effect on the dissociation constants.

Following the metal binding studies, we measured the T1 and T2 relaxivities of Gd^{3+}-CCMV particles as function of the Larmor frequency over a range of 2 to 62 MHz

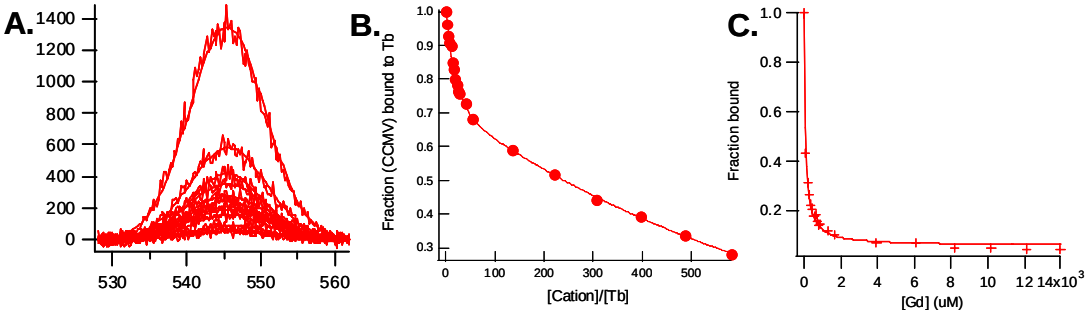

Figure 6.10: A. Fluorescence spectra for competitive binding to CCMV (520-570 nm), B. Fluorescence isotherms for competitive binding experiment to CCMV as Ca^{2+} is added, and C. As Gd^{3+} is added to a final ratio of 500 cations/Tb^{3+}.

(H = 0.05 – 1.5 Tesla) (Figures 6.11). For comparison, $GdCl_3$ samples of equimolar concentration were measured in parallel. The data are expressed as 1/T1 and 1/T2 per mM of bound Gd^{3+}, with the buffer contribution subtracted. According to equation 2.1, 78% of the metal binding sites of CCMV had bound Gd^{3+} at 200 μM Gd^{3+} and 114 μM CCMV subunit corresponding to 89 μM bound Gd^{3+}. This value was confirmed by the arsenazo III colorimetric assay to be 72.6 % bound or 82.5 μM of bound Gd^{3+}. Our custom-built relaxometer has been validated as having an absolute accuracy of 5% (compared with literature values) and a reproducibility of 1% for a number of standard solutions. For Gd^{3+}-CCMV, the T1 relaxivity ranged from 86 $mM^{-1}s^{-1}$ at 2 MHz (0.05 Tesla) to 202 $mM^{-1}s^{-1}$ at the highest field measured after subtracting the contribution of free Gd^{3+} at the same total Gd^{3+} concentration. The T2 relaxivities were even larger, ranging from 81 to 376 $mM^{-1}s^{-1}$ after subtracting the signal of free Gd^{3+}. In contrast, the T1 values for the $GdCl_3$ showed significantly lower relaxivities ranging from 29 $mM^{-1}s^{-1}$ at 2 MHz to 20 $mM^{-1}s^{-1}$ at 62 MHz, while the T2 relaxivities ranged from 32 to 21 $mM^{-1}s^{-1}$. When comparing Figs 5A and 5B, it is evident that for Gd^{3+}-CCMV both the 1/T1

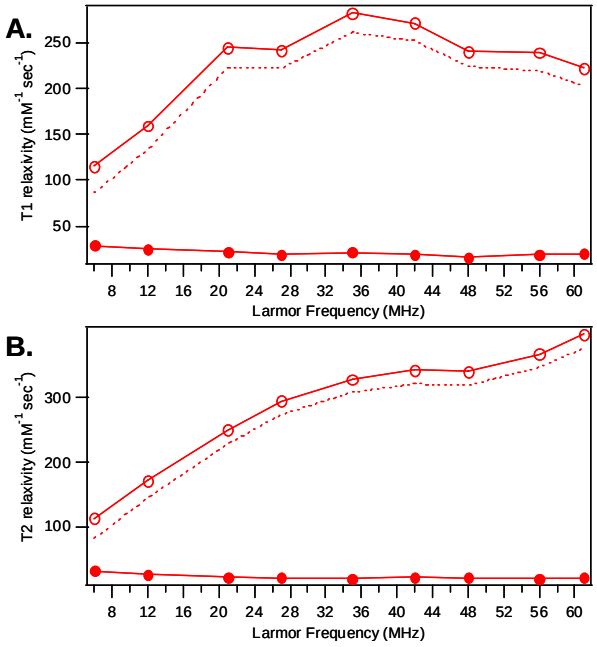

Figure 6.11: A. Relaxivity data for T1 and T2 relaxivities plotted as a function of Larmor frequency.

and 1/T2 curves must be dominated by the very long correlation time (τ_c) of the large, slowly tumbling virions.

The measured Gd^{3+}-CCMV relaxivities represented the highest values for paramagnetic species and has only recently been surpassed with another viral protein cage system[171]. With approaching 180 Gd^{3+} ions per virion, a total T1 relaxivity of roughly 3.6 x 10^4 mM^{-1} of virus particle s^{-1} can be obtained. These very high values make the Gd^{3+}-CCMV complex an excellent candidate for further study as an MR contrast agent. However, for biological applications in molecular imaging, the *in vivo* stability of the metal binding in the Gd^{3+}-CCMV complex will need to be further addressed, as well as its potential immunogenicity. It is at present not known if, *in vivo*, local high concentrations of Ca^{2+} could compete for metal binding on the virus surface and destabilize the complex. However, under the conditions of our binding studies 1.5

mM Ca^{2+} had very little effect on the stability of the Gd^{3+}-CCMV complex. Also, as compared to chelated Gd^{3+}-containing macromolecules, the unusually high relaxivity values of Gd^{3+}-CCMV likely reflects a combination of possibly have a larger number of waters bound to Gd^{3+} in conjunction to the very large size of the particle (lower Brownian frequency), and the fact that 3 Gd^{3+} ions bind in a fairly small metal binding pocket of CCMV. In light of considering the fairly high dissociation constants compared to chelated Gd^{3+} contrast agents, modifications to the CCMV protein cage are under investigation that will increase Gd^{3+} binding. In the meantime, the observed high relaxivities of the Gd^{3+}-CCMV system are an indication that viral protein cages may be considered as candidates for the development of a new platform for combined drug delivery and MR imaging .

Conclusion

The metal binding affinity has been measured for three forms of CCMV including wtCCMV, subE and mbsD. This was the first quantitative study of metal binding to a plant virus. Genetic engineering has allowed us to compare contributions of the metal binding site in the protein shell to that of a metal nucleic acid interaction. In the subE mutant the ability of the particle to bind nucleic acid was removed with no significant change in the metal binding affinity. All data were effectively modeled by a single site model. This is consistent with the CCMV crystal structure which suggested the presence of 180 quasi-equivalent metal binding sites located at the 60 pseudo three-fold axes of the T=3 icosahedral particles. Metal binding at this putative site was further confirmed by

our studies with a metal binding site deletion mutant where the apparent K_d was observed to increase significantly. In this mutant the coordinating amino acids at the putative metal binding sites were genetically replaced with non-coordinating residues. It is curious that the protein cage of this metal binding site deletion mutant still shows affinity for Tb^{3+} though to a considerably lower degree. This suggests that the metal coordination at the site has not been completely eliminated or that other lower affinity sites on the protein exist. There are two other Trp residues in the protein cage that could contribute to metals bound either at the metal binding site, or at other sites unrecognized sites in the protein structure.

WtCCMV was probed for its affinity for both Ca^{2+} and for Gd^{3+}. Competitive binding experiments with Ca^{2+} indicate that there is about a 100 fold decrease in binding affinity for the divalent cation than for Tb^{3+}. Gd^{3+} adequately displaces the Tb^{3+} from the metal binding sites with a similar dissociation constant. The dissociation constant for Gd^{3+} binding to CCMV in the presence of 1.5 mM Ca^{2+} does not change by much indicating that Ca^{2+} does not interfere with Ln^{3+} binding under a cellularly relevant concentration of Ca^{2+}.

When Gd-CCMV is probed for potential use as an MRI contrast agent it was shown that proton relaxivity is much quicker for this paramagnetic species than for all small molecule chelate systems including those that are commercially available and regularly used in MRI [38].

The biological role of metal binding to virus structure, assembly, disassembly, infection and replication are not yet fully understood. Many viruses require the presence

of metals, while others do not require any metals to be present. Metal concentration has been used in CCMV as a mode of building hierarchical structures that range in diversity from 60 subunit protein cages with icosahedral symmetry to thousands of subunits coming together to form sheets and tubes [99, 100]. The role of metal binding to virus infection has been shown for some systems but most systems have not yet been studied. Future studies should focus on developing an understanding of the biological role of metal binding by comparing mutants of CCMV and looking at phenotype changes, ranging from viral infection and transmission to the structure of the virus. Since the size of the virus contributes to a favorable T1 relaxation time when Gd^{3+} ions are bound to the virus it is critical to use chemical means to attach chelate molecules that bind Gd^{3+} to a higher affinity so that the best parts of each system can be exploited to use CCMV as a viable contrast agent.

METAL BINDING TO CUCUMBER MOSAIC VIRUS (CMV) PROBED BY FLUORESENCE RESONANCE ENERGY TRANSFER (FRET)

Introduction

In chapter 6 it was clearly introduced that metal binding plays an important role in the assembly, function and stability of many supramolecular assemblies with an emphasis on Cowpea chlorotic mottle virus (CCMV). Another virus that is structurally similar to CCMV and has been compared to CCMV is another member of the *Bromoviridae*, Cucumber mosaic virus (CMV), specifically the Fny strain[24].

CMV is a plant virus that infects over 800 species of plant hosts ranging from tomatoes to cucumbers[172]. CMV is a member of the *Cucumovirus* genus (part of the *Bomoviridae* family) and is unique in that it is transmitted from host to host through an

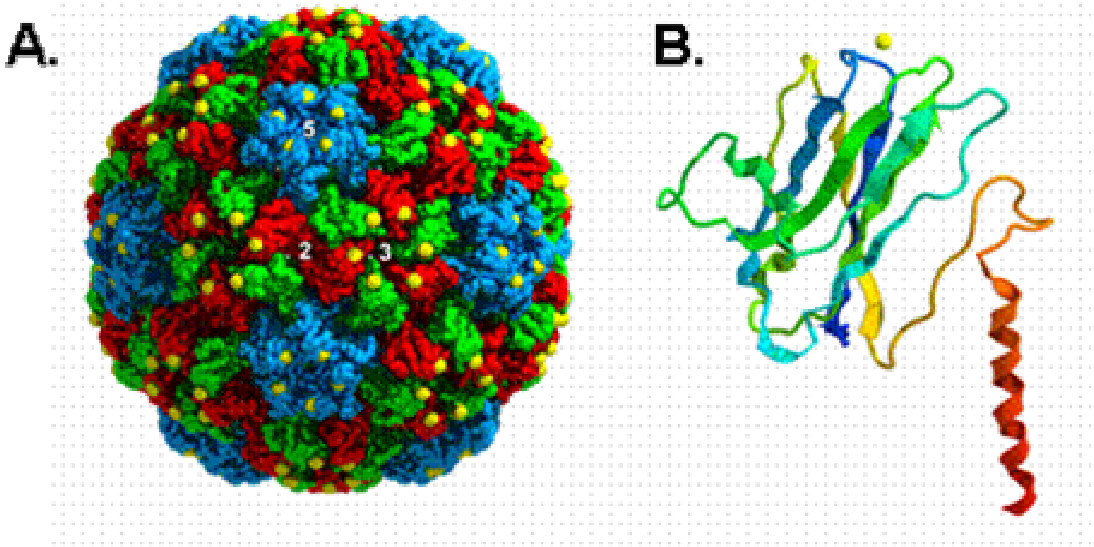

Figure 7.1: A. Assembled virus showing metal bound to the putative metal binding site, B. Subunit structure showing the outer loop that binds metal [106].

aphid mediator. Several strains of the virus have been isolated and grouped into two sub-groups (I and II) that are distinct in their transmission epitopes. The structure of CMV has been determined to 3.2 Å resolution using both high resolution 3-D cryo electron microscopy and image reconstruction as well as X-ray crystallography[24, 173]. While the Fny strain of CMV is similar to CCMV there are many notable differences. Among the similarities are structural morphology (size and orientation of β-barrels), the interactions that form the hexamer at the three-fold axis, and some primary sequence similarity. Some notable differences are that CMV has a unique fold that makes up the β-annulus, the subunits that make up the T=3 asymmetric unit are not chemically identical, and most importantly for this study is that CMV does not undergo the pH and metal ion dependent swelling described previously for CCMV.

The aphid transmission of CMV has been well studied and it has been determined that on the exterior surface multiple aphid specific binding motifs exist that are thought to interact with a part of the aphid's mouth. Many mutants have been prepared that have impaired transmission. Keith Perry and Tom Smith have focused on a putative metal binding site as being the site that causes the greatest disruption to aphid transmission.

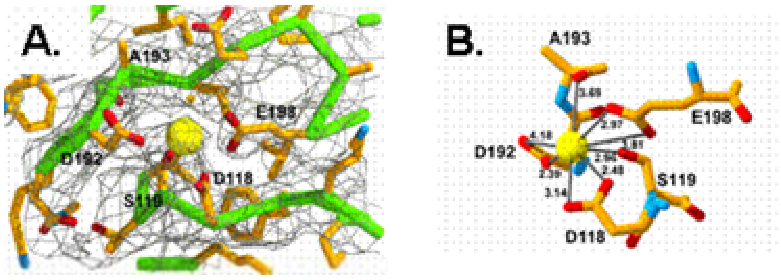

Figure 7.2: A. Close up view of the putative metal binding site, B. Metal binding site with D118, S119, D192, A193, and E198 in a geometry that can bind Ca^{2+}.

Using ICP analysis Tom Smith has determined that CMV preps are always isolated with a stoichiometric ratio of metal ions bound to the capsid and has proposed the metal binding site to consist of the backbone oxygen of A193 as well as the side-chain oxygens of D118, S119, D192, and E198 (Figure 7.2)[106]. In close proximity to these residues is W122 and F117 along with other aromatic amino acids making this an ideal system for studying the metal binding affinity using the fluorescence resonance energy transfer (FRET) assay described previously. Three forms of the Fny strain of CMV were studied using FRET. These include the wild type virus as well as two mutants to the putative metal binding site (D118A and D192A). Neither of these mutants is transmissible by aphids, indicating that metal binding may play a role in transmission.

Materials and Methods

Protein Purification

Three forms of CMV were used in this study, wild-type CMV, D118A, and D192A. All three forms were received from the laboratory of Keith Perry in pH 9 buffer. Before doing any FRET studies each virus was purified by size exclusion chromatography (ÄKTA 900) using a gel filtration column (Amersham Biosciences Superose 6 10/300) in the metal binding buffer (50 mM MES, 100 mM NaCl pH 6.5). All FRET experiments were performed immediately after purification.

Size Analysis by Dynamic Light Scattering (DLS)

DLS of purified CMV was performed on a Brookhaven Instruments Corporation ZetaPALS particle size analyzer equipped with a 661 nm diode laser and monitoring the

scattered light at 90^{o} with an avalanche photodiode detector. The acquired correlation functions were then fit using a non-negatively constrained least squares analysis to report a hydrodynamic diameter.

Transmission Electron Microscopy (TEM)

TEM was performed on a Leo 912 microscope operating at 100 kV accelerating voltage. Sample preparation involved placing 5 μL of purified CMV onto a formvar and carbon coated 300 mesh copper TEM grid (Ted Pella).

Fluorescence

All fluorescence experiments were performed on a SPEX Fluorolog spectrophotometer at 25 ^{o}C nearly identically to that described in chapter 6 with the exception that the excitation and emission slit widths were set to 4 and 4 nm respectively. The excitation slit was made smaller because of the abundance of Trp and Tyr in CMV, the fluorescence intensity is considerably higher than in CCMV. Solutions of Tb^{3+} were prepared by diluting a Tb^{3+} ICP standard to form working solutions of 5, 50, 500, and 5000 μM.

For competitive binding experiments stock solutions of Ca^{2+} were prepared either from salts of $CaCl_2$ prepared in doubly deionized water to (18 MΩ resistivity) or from purchased ICP standards (Aldrich) prepared in pH 6.5 buffer (50 mM MES 100 mM NaCl).

Data Analysis and Determination of Dissociation Constants

All data analysis was identical to that described in chapter 6 with the notable exception that the Tryptophan fluorescence peak shifted from 350 nm to about 330 nm indicating that the aromatic amino acid may be in a more hydrophobic cluster of amino acids[174]. The Igor macro employed in data analysis of the initial Tb^{3+} binding is found in appendix 2 and the Igor macro used for determining the dissociation constant for the competitive binding of Ca^{2+} to displace the bound Tb^{3+} is found in appendix 3.

Results

FRET experiments were performed on CMV particles purified into pH 6.5 buffer

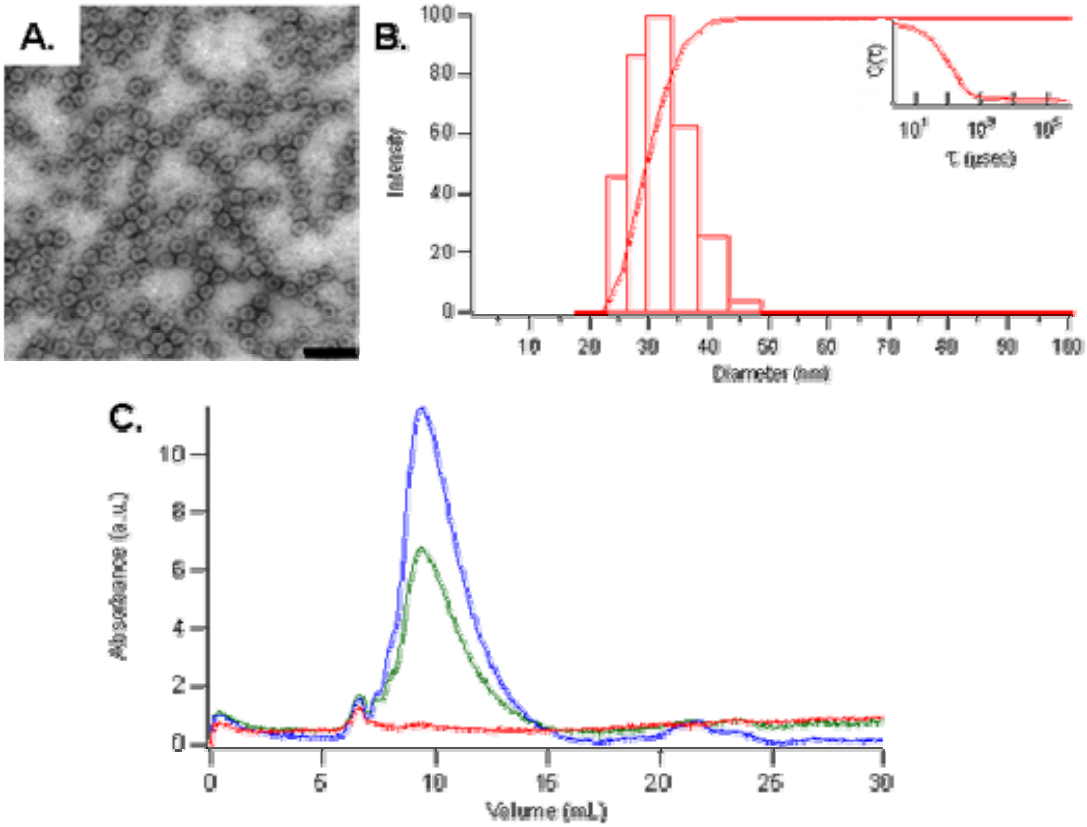

Figure 7.3: A. Negatively stained TEM image, B. SEC profile showing an elution around 12 mLs, C. DLS of purified virus immediately before metal binding.

(50 mM MES, 100 mM NaCl). SEC and DLS of the virus solutions was performed immediately before FRET experiments in order to confirm the size and purity of the solutions. The SEC profile of CMV was identical to that of CCMV, consistent with a 29 nm virus particle (Figure 7.3A) and DLS confirmed the presence of intact virus (Figure 7.3B).

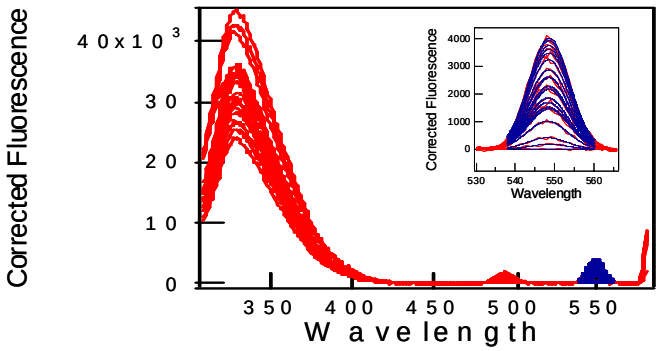

Figure 7.4: Spectra showing fluorescence from 308-580 nm , inset is the 520-570 nm spectra focusing on the Tb^{3+} fluorescence.

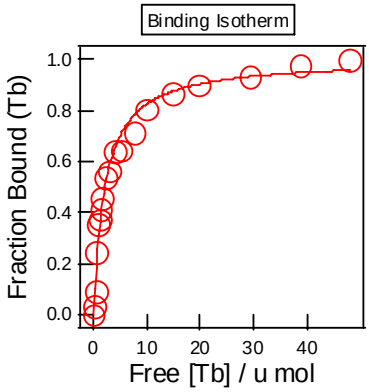

Figure 7.5: Binding isotherm of the Tb^{3+} fluorescence.

The wild type CMV was probed both for Tb^{3+} affinity and a competitive binding experiment was performed to determine the affinity of the virus for Ca^{2+}. Fluorescence spectra were collected 308 to 580 nm so that both the decrease in Trp fluorescence and

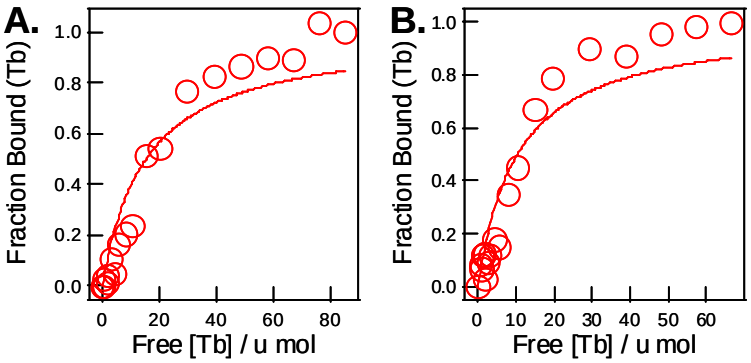

Figure 7.6: A. Binding isotherm for D118A mutant focusing on the Tb^{3+} fluorescence, B. Binding isotherm for D192A mutant.

the increase in Tb^{3+} fluorescence could be seen (Figure 7.4). The spectra were also scanned between 520 to 570 nm so that a higher resolution data set could be collected on the increase in Tb^{3+} fluorescence as the metal bound to the virus (Figure 7.4 inset). The peaks at both 340 and 545 were fit using a Gaussian peak shape and the peak heights were plotted with respect to the cation concentration and cations per subunit (Figure 7.5). After fitting these data according to the method explained in chapter 6 (appendix 1) the dissociation constant (K_d) for Tb^{3+} was determined to be 2.67 ±0.46 μM.

A competitive binding experiment was performed on wild type CMV in order to determine the dissociation constant for Ca^{2+}, the more physiologically relevant metal ion for this virus. After saturating the metal binding sites with 40 μM Tb^{3+}, aliquots of Ca^{2+} were added into the solution and the increase in Trp fluorescence (330nm) was monitored. At fit of these data yielded an apparent binding constant of 1.54 mM, which was then applied to equation 6.3 to determine the dissociation constant (K_d) to be 226 μM.

The Tb^{3+} K_d were also determined for two mutants that had residues involved in the metal binding site changed to alanine (D118A and D192A). The data were collected in the same manner as described for the wtCMV with sample spectra for the Tb^{3+}

fluorescence data and a binding isotherm shown for D192A. The K_d for Tb^{3+} binding to these single point mutations increased about 4 fold relative to dissociation of Tb^{3+} from wtCMV to 16.0 ±6.4 μM and 10.6 ±0.5 μM for D118A and D192A respectively (Figure 7.6).

Discussion

It has been known for some time that relatively minor changes to the exterior of CMV often causes phenotypic changes in the virus. Among these phenotypes are the inability to transmit the virus through the aphid transmission system. The wild type virus was shown to be transmitted by aphids and infect other plant hosts 85 out of 87 attempts. Both of the mutants in this study have zero transmission out of 20 and 30 attempts for D118A and D192A respectively. It has been suggested that the drastic change in transmission may not necessarily be due to a change to an aphid binding epitope, as many other groups have stated, but rather due to a decrease in metal binding affinity. It was presumed, based on the ICP metal analysis, that the metal binding affinity for CMV would be considerably higher than that reported for CCMV. The dissociation constant (K_d) for Tb^{3+} binding to wtCCMV has been reported to be 19 μM while that of Ca^{2+} was 1.97 mM. From the data presented in this chapter, CMV exhibits about a 10 fold higher affinity for both Tb^{3+} and the biologically relevant Ca^{2+} as compared to CCMV which has dissociation constants (K_d) of 2.3 μM and 226 μM for Tb^{3+} and Ca^{2+} respectively.

From these experiments, it is clear that mutations to the putative metal binding site of CMV do have an effect on the metal binding affinity. Single amino acid changes result in a decrease in metal binding affinity for Tb^{3+} of between 3 to 7 fold. These

mutants still have a relatively high metal binding affinity that is on the order of wtCCMV, but the decrease is significant. The K_d for bound Tb^{3+} to the D118A mutant of CMV is 16 μM while that of D192A is 10 μM. In figure 7.2 the metal binding site is shown with proposed bond distances. Based on the structural geometry of the metal binding site it is clear that a mutation to D118 would be expected to cause the greatest change in the metal binding affinity since the carboxyl binds in a bidentate fashion with bond distances of 2.48 and 3.14 Å, while the D192 appears to be only monodentate since the second carboxyl oxygen is 4.18 Å from the metal center.

The competitive binding studies for both CMV and CCMV indicate that Ca^{2+} has about a 100 fold decrease in binding affinity as compared to the trivalent Tb^{3+}. Thus, an estimation of the K_d for Ca^{2+} binding to the two mutants (D118A and D192A) will be about 2 and 1 mM for respectively. When considering the biological concentration of Ca^{2+} this is a significant change in binding affinity that could be the reason for the observed phenotype (loss of transmission).

Conclusion

In this study the metal binding affinity of wtCMV was determined for both the spectroscopically relevant lanthanide (Tb^{3+}) as well as for the biologically relevant alkaline earth metal (Ca^{2+}). CMV is not as structurally dynamic as CCMV, but does have a metal binding site that these data suggest is about ten fold greater than for CCMV. ICP analysis has previously indicated is the presence of a metal binding site in CMV and five amino acids were proposed to be involved (D118, S119, D192, A193, E198) in metal

chelation. Mutations to two of these amino acids (D118A and D192A) causes a significant decrease in metal binding affinity. This indicates that D118 and D192 are directly involved in Ca^{2+} binding and that this proposed metal binding site is indeed the highest affinity binding site in the CMV capsid.

More research must be done in order to determine if the reason for a loss of viral transmission is caused by a decrease in metal binding. The Ca^{2+} dissociation constants must be determined for the two mutations in order to confirm that the biologically relevant dissociation constant is on the order of mM while the wild type virus is in the hundreds of μM. There also must be some interaction with the aphid mouth parts that would have to be metal ion dependent.

It is also important to study multiple mutants and possibly get rid of the metal binding site all together. This is complimentary to the study involving CCMV and would indicate whether or not there is another lower affinity site somewhere else in the viral capsid.

CONCLUDING REMARKS

Protein cages serve as nano-scaffolds for biomimetic materials synthesis and metal binding. Protein cages are well defined nano-containers and when used for materials synthesis the benefits of a biological macromolecular passivating layer on the material serves both to isolate the mineral core from the environment, but also may aid in such things as catalysis, and magnetism. Furthermore, the biologically addressable protein cage can serve for using these materials in medical applications, particularly MRI contrast agents and therapeutic agent delivery. This can be controlled by altering the exterior of the protein cage with either a masking molecule that could 'hide' the cage from the immune system or a targeting molecule that would provide directionality of the protein cage to a specific cellular target. In order for these goals to be realized an understanding of all three interfaces represented by the protein cage system must be clearly understood. Knowing the surface characteristics of the interior of the protein cage enables design of protocols that allow for both native (nucleic acid/iron biomineral) and non-native (therapeutic or functional hard material) material encapsulation. Understanding the exterior of the protein cage allows the design of functionality that relies on some type of molecular recognition. The interface between subunits may give some of the best insight into what drives protein cage assembly by studying subunit/subunit interactions. One such method that has been analyzed here has been the function of metal binding at the subunit interface of some viral protein cages. Studying metal binding allows for the characterization of the role metals play in some biological

systems as well as potentially deriving a biomedically relevant high relaxivity magnetic resonance imaging agent.

The electrostatic model for biomineralization has been studied using multiple protein cage systems that vary in their electrostatic characteristics. This has been led by the model system of Fn with the design of a ferritin mimicking viral protein cage (SubE). SubE has the electrostatic characteristics for metal oxide synthesis, however it is not stable enough to be used for the preparation of magnetically interesting iron oxides. For this reason the protein cage was chemically modified in order to gain stability for a broad range of mineralization conditions. LDps also has a similar electrostatic interior surface as Fn, and has been used for a range of materials synthesis including crystalline phases of iron and cobalt oxides. LDps has a benefit of being thermally stable, similar to Fn. WtCCMV has the opposite interior surface potential to that of Fn and can not be used for metal oxide mineralization, but if the choice of precursor ion is changed from a cation to some anionic species, wtCCMV is also able to direct mineral encapsulation. The method by which mineralization takes place in CCMV allows for the preparation of monodisperse mineral particles that conform to the exact dimensions of the interior of the protein cage. This makes the synthesized materials interesting from a perspective of understanding the biological/mineral interface. While polyoxometallates are not biologically relevant, the basic principles of biomineralization can be explored using a number of techniques including HRTEM, through focal series reconstruction, and 3D-TEM image reconstruction.

From a purely materials perspective, protein cages offer a range of possibilities that include the production of technology and imaging capabilities. Furthermore, these nano-reaction vessels are synthesized biologically making a seemingly endless supply of protein cages. The reactions performed inside protein cages do scale up as has been demonstrated by the synthesis of gram quantities of Mn_2O_3-Fn.

Metal binding studies were performed on CCMV and CMV for the purpose of determining a metal binding affinity. Gaining insight into metal binding affinity may yield insight into the protein interactions that drive the structural dynamics prevalent in biological systems as well as possibly gain insight in the role of metals in viral infectivity and transmission. In CCMV several forms were studied in order to learn about the modes of metal binding, the results indicate that metal binding is dominated by the metal binding site and other modes (nucleic acid binding metals) probably play a small role. As an extension of metal binding affinity, the paramagnetic lanthanide (Gd^{3+}) was also studied for the purpose of using Gd-CCMV as an MRI contrast agent. Gd-CCMV increase both T1 and T2 relaxivity by more than 100 fold above small molecule Gd^{3+}-chelates. The metal binding affinity of CCMV for Gd^{3+} is still too low for Gd-labeled virus to be used as a contrast agent, however studies are underway to increase the binding affinity by functionalizing the protein with Gd^{3+} chelators that will allow the combination of the strong binding of Gd-chelates with the contrast enhancing effect of CCMV.

For CMV the metal binding affinity was determined in order to study the effect of mutations to the putative metal binding site to viral transmission. The results of the metal

binding studies must still be combined with biochemical data in order to gain greater insight to the role of Ca^{2+} in viral transmission.

REFERENCES CITED

1. Mann, S.; Archibald, D. D.; Didymus, J. M.; Douglas, T.; Heywood, B. R.; Meldrum, F. C.; Reeves, N. J., Crystallization at Inorganic-Organic Interfaces - Biominerals and Biomimetic Synthesis. *Science* **1993,** 261, (5126), 1286-1292.

2. Koeck, P. J. B.; Kagawa, H. K.; Ellis, M. J.; Hebert, H.; Trent, J. D., Two-dimensional crystals of reconstituted .beta.-subunits of the chaperonin TF55 from Sulfolobus shibatae. *Biochim. Biophys. Acta* **1998,** 1429, (1), 40-44.

3. Trent, J. D., A review of acquired thermotolerance, heat-shock proteins, and molecular chaperones in archaea. *FEMS Microbiol. Rev.* **1996,** 18, (2-3), 249-258.

4. Trent, J. D.; Kagawa, H. K.; Yaoi, T.; Olle, E.; Zaluzec, N. J., Chaperonin filaments: the archaeal cytoskeleton? *Proc. Natl. Acad. Sci. U. S. A.* **1997,** 94, (10), 5383-5388.

5. Wiedenheft, B.; Mosolf, J.; Willits, D.; Yeager, M.; Dryden, K. A.; Young, M.; Douglas, T., An archaeal antioxidant: Characterization of a Dps-like protein from Sulfolobus solfataricus. *Proceedings of the National Academy of Sciences of the United States of America* **2005,** 102, (30), 10551-10556.

6. Ramsay, R.; Wiedenheft, B.; Allen, M.; Gauss, G. H.; Lawrence, C. M.; Young, M.; Douglas, T., Dps-like protein from the hyperthermophilic archaeon *Pyrococcus furiosus*. *Journal of Inorganic Biochemistry* **2006,** 100, 1061-1068.

7. Grant, R. A.; Filman, D. J.; Finkel, S. E.; Kolter, R.; Hogle, J. M., The crystal structure of Dps, a ferritin homolog that binds and protects DNA. *Nature Structural Biology* **1998,** 5, (4), 294-303.

8. Bozzi, M.; Mignogna, G.; Stefanini, S.; Barra, D.; Longhi, C.; Valenti, P.; Chiancone, E., A Novel Non-heme Iron-binding Ferritin Related to the DNA-binding Proteins of the Dps Family in *Listeria innocua*. *J. Biol. Chem.* **1997,** 272, 3259-3265.

9. Zhao, G.; Ceci, P.; Ilari, A.; Giangiacomo, L.; Laue, T. M.; Chiancone, E.; Chasteen, N. D., Iron and Hydrogen Peroxide Detoxification Properties of Dps. A Ferritin-Like DNA Binding Protein of *Escherichia coli*. *J. Biol. Chem.* **2002,** epub.

10. Grove, A.; Wilkinson, S. P., Differential DNA binding and protection by dimeric and dodecameric forms of the ferritin homolog Dps from Deinococcus radiodurans. *Journal of Molecular Biology* **2005,** 347, (3), 495-508.

11. Ilari, A.; Ceci, P.; Ferrari, D.; Rossi, G. L.; Chiancone, E., Iron incorporation into Escherichia coli Dps gives rise to a ferritin-like microcrystalline core. *Journal of Biological Chemistry* **2002,** 277, (40), 37619-37623.

12. Ilari, A.; Latella, M. C.; Ceci, P.; Ribacchi, F.; Su, M. H.; Giangiacomo, L.; Stefanini, S.; Chasteen, N. D.; Chiancone, E., The unusual intersubunit ferroxidase center of Listeria innocua Dps is required for hydrogen peroxide detoxification but not for iron uptake. A study with site-specific mutants. *Biochemistry* **2005,** 44, (15), 5579-5587.

13. Kauko, A.; Haataja, S.; Pulliainen, A. T.; Finne, J.; Papageorgiou, A. C., Crystal structure of Streptococcus suis dps-like peroxide resistance protein Dpr: Implications for iron incorporation. *Journal of Molecular Biology* **2004,** 338, (3), 547-558.

14. Pulliainen, A. T.; Kauko, A.; Haataja, S.; Papageorgiou, A. C.; Finne, J., Dps/Dpr ferritin-like protein: insights into the mechanism of iron incorporation and evidence for a central role in cellular iron homeostasis in Streptococcus suis. *Molecular Microbiology* **2005,** 57, (4), 1086-1100.

15. Su, M. H.; Cavallo, S.; Stefanini, S.; Chiancone, E.; Chasteen, N. D., The so-called Listeria innocua ferritin is a Dps protein. Iron incorporation, detoxification, and DNA protection properties. *Biochemistry* **2005,** 44, (15), 5572-5578.

16. Black, D. R.; Connell, C. J.; Merigan, T. C., Structure and Infectivity of Picornaviral Rna Encapsidated by Cowpea Chlorotic Mottle Virus Protein. *Journal of Virology* **1973,** 12, (6), 1209-1215.

17. Carrington, J. C.; Morris, T. J.; Stockley, P. G.; Harrison, S. C., Structure and assembly of turnip crinkle virus. *J. Mol. Biol.* **1987,** 194, 265-276.

18. Geelen, J.; Vankamme.A; Verduin, B. J. M., Structure of Capsid of Cowpea Mosaic Virus - Chemical Subunit - Molecular-Weight and Number of Subunits Per Particle. *Virology* **1972,** 49, (1), 205-&.

19. Lin, T.; Chen, Z.; Usha, R.; Stauffacher, C. V.; Dai, J. B.; Schmidt, T.; Johnson, J. E., The refined crystal structure of cowpea mosaic virus at 2.8 A resolution. *Virology* **1999,** 265, 20-34.

20. Lucas, R. W.; Larson, S. B.; McPherson, A., The crystallographic structure of brome mosaic virus. *Journal of Molecular Biology* **2002,** 317, (1), 95-108.

21. Munshi, S.; Liljas, L.; Johnson, J. E., Structure determination of Nudaurelia capensis omega virus. *Acta Crystallogr D Biol Crystallogr* **1998,** 54, (2 (Pt 6)), 1295-305.

22. Prasad, B. V.; Dokland, T.; Bella, J.; Rossmann, M. G.; Hardy, M. E.; Estes, M. K., X-ray crystallographic structure of the Norwalk virus capsid. *Science* **1999,** 286, 287-290.

23. Rees, M. W.; Short, M. N., The Primary Structure of Cowpea Chlorotic Mottle Virus Coat Protein. *Virology* **1982,** 119, (2), 500-503.

24. Smith, T. J.; Chase, E.; Schmidt, T.; Perry, K. L., The structure of cucumber mosaic virus and comparison to cowpea chlorotic mottle virus. *Journal of Virology* **2000,** 74, (16), 7578-7586.

25. Speir, J. A.; Munshi, S.; Wang, G.; Baker, T. S.; Johnson, J. E., Structures of the native and swollen forms of cowpea chlorotic mottle virus determined by X-ray crystallography and cryo-electron microscopy. *Structure* **1995,** 3, 63-78.

26. Stehle, T.; Gamblin, S. J.; Yan, Y.; Harrison, S. C., The structure of simian virus 40 refined at 3.1 A resolution. *Structure* **1996,** 4, (2), 165-182.

27. Stehle, T.; Yan, Y.; Benjamin, T. L.; HArrison, S. C., Structure of murine polyomavirus complexed with an ologosaccharide receptor fragment. *Nature* **1994,** 369, 160-183.

28. Crick, F. H. C.; Watson, J. D., Structure of Small Viruses. *Nature* **1956,** 177, 473-475.

29. Crichton, R. R., Structure and function of ferritin. *Angew. Chem. Int. Ed. Engl.* **1973,** 12, 57-65.

30. Ilari, A.; Savino, C.; Stefanini, S.; Chiancone, E.; Tsernoglou, D., Crystallization and preliminary X-ray crystallographic analysis of the unusual ferritin from Listeria innocua. *Acta Crystallographica Section D-Biological Crystallography* **1999,** 55, 552-553.

31. Lawson, D. M.; Artymiuk, P. J.; Yewdall, S. J.; Smith, J. M. A.; Livingstone, J. C.; Treffry, A.; Luzzago, A.; Levi, S.; Arosio, P.; Cesareni, G.; Thomas, C. D.; Shaw, W. V.; Harrison, P. M., Solving the Structure of Human H-Ferritin by Genetically Engineering Intermolecular Crystal Contacts. *Nature* **1991,** 349, (6309), 541-544.

32. Reddy, V.; Natarajan, P.; Okerberg, B.; Li, K.; Damodaran, K.; Morton, R.; Brooks, I. C.; Johnson, J. E., Virus Particle Explorer (VIPER), a Website for virus capsid structures and their computational analysis. *J. Virology* **2001,** 75, 11943-11947.

33. Allen, M.; Willits, D.; Mosolf, J.; Young, M.; Douglas, T., Protein Cage Constrained Synthesis of Ferrimagnetic Iron Oxide Nanoparticles. *Adv. Mater.* **2002,** in press.

34. Allen, M.; Willits, D.; Young, M.; Douglas, T., Constrained synthesis of cobalt oxide nanomaterials in the 12-subunit protein cage from Listeria innocua. *Inorganic Chemistry* **2003,** 42, (20), 6300-6305.

35. Douglas, T.; Young, M., Host-guest encapsulation of materials by assembled virus protein cages. *Nature* **1998,** 393, (6681), 152-155.

36. Douglas, T.; Strable, E.; Willits, D.; Aitouchen, A.; Libera, M.; Young, M., Protein engineering of a viral cage for constrained nanomaterials synthesis. *Advanced Materials* **2002,** 14, (6), 415-+.

37. Allen, M.; Prissel, M. M.; Minor, A.; Young, M.; Douglas, T., Synthesis and Characterization of Ferrimagnetic Particles Inside a Genetically and Chemically Altered Viral Protein Cage. *Journal of the American Chemical Society* **2006,** *In preparation*.

38. Allen, M.; Bulte, J. W. M.; Liepold, L.; Basu, G.; Zywicke, H. A.; Frank, J. A.; Young, M.; Douglas, T., Paramagnetic viral nanoparticles as potential high-relaxivity magnetic resonance contrast agents. *Magnetic Resonance in Medicine* **2005,** 54, (4), 807-812.

39. Basu, G.; Allen, M.; Willits, D.; Young, M.; Douglas, T., Metal binding to cowpea chlorotic mottle virus using terbium(III) fluorescence. *Journal of Biological Inorganic Chemistry* **2003,** 8, (7), 721-725.

40. Harrison, P. M.; Arosio, P., The ferritins: molecular properties, iron storage function and cellular regulation. *Biochimica et Biophysica Acta* **1996,** 1275, 161-203.

41. Matias, P. M.; Tatur, J.; Carrondo, M. A.; Hagen, W. R., Crystallization and preliminary X-ray characterization of a ferritin from the hyperthermophilic archaeon and anaerobe Pyrococcus furiosus. *Acta Crystallographica Section F-Structural Biology and Crystallization Communications* **2005,** 61, 503-506.

42. Hempstead, P. D.; Yewdall, S. J.; Fernie, A. R.; Lawson, D. M.; Artymiuk, P. J.; Rice, D. W.; Ford, G. C.; Harrison, P. M., Comparison of the three-dimensional structures of recombinant human H and horse L ferritins at high resolution. *J. Mol. Biol.* **1997,** 268, 424-448.

43. Kurtz, D. M., Jr., Structural similarity and functional diversity in diiron-oxo proteins. *JBIC, J. Biol. Inorg. Chem.* **1997,** 2, (2), 159-167.

44. Bou-Abdallah, F.; Lewin, A. C.; Le Brun, N. E.; Moore, G. R.; Chasteen, N. D., Iron detoxification properties of Escherichia coli bacterioferritin - Attenuation of oxyradical chemistry. *Journal of Biological Chemistry* **2002,** 277, (40), 37064-37069.

45. Chiancone, E.; Ceci, P.; Ilari, A.; Ribacchi, F.; Stefanini, S., Iron and proteins for iron storage and detoxification. *Biometals* **2004,** 17, (3), 197-202.

46. Pierre, J. L.; Fontecave, M., Iron and activated oxygen species in biology: The basic chemistry. *BioMetals* **1999,** 12, 195-199.

47. Kehrer, J. P., *Toxicology* **2000,** 149, 43-50.

48. Sawyer, D. T.; Sobkowiak, A.; Matsushita, T., *Accounts of Chemical Research* **1996,** 29, 409-416.

49. Martins, E. A. L.; Robalinho, R. L.; Meneghini, R., Oxidative Stres Induces Activation of a Cytosolic Protein Responsible for Control of Iron Uptake. *Archives of Biochemistry and Biophysics* **1995,** 316, (1), 128-134.

50. Theil, E. C., Ferritin: Structure, Gene Regulation, and Cellular Function in Animals, Plants, and Microorganisms. *Annual Review in Biochemistry* **1987,** 56, 289-315.

51. Williams, J.; Chasteen, N. D.; Moreton, K., The effect of salt concentration on the iron-binding properties of human transferrin. *Biochem. J.* **1982,** 201, (3), 527-32.

52. Arosio, P.; Levi, S., Ferritin, iron homeostasis, and oxidative damage. *Free Radical Biology and Medicine* **2002,** 33, (4), 457-463.

53. Rodriguez, G. M.; Smith, I., Mechanism of iron regulation in mycobacteria: role in physiology and virulence. *Molecular Microbiology* **2003,** 47, (6), 1485-1494.

54. Eisenstein, R. S.; Garcia-Mayol, D.; Pettingell, W.; Munro, H. N., Regulation of ferritin and heme oxygenase synthesis in rat fibroblasts by different forms of iron. *Cell Biology* **1991,** 88, 688-692.

55. Dix, D. J.; Lin, P. N.; Kimata, Y.; Theil, E. C., The Iron Regulatory Region of Ferritin mRNA is also a Positive Control Element for Iron-Independent Translation. *Biochemistry* **1992,** 31, (10), 2818-2822.

56. Lawrence, C. M.; Ray, S.; Babyonyshev, M.; Galluser, R.; Borhani, D. W.; Harrison, S. C., Crystal structure of the ectodomain of human transferrin receptor. *Science* **1999,** 286, (5440), 779-782.

57. Harris, D. C., Iron Exchange between Ferritin and Transferrin *in Vitro*. *Biochemistry* **1978,** 17, (15), 3071-3078.

58. Treffry, A.; Harrison, P. M., *Journal of Biochemistry* **1979,** 181, 708-716.

59. Mosolf, J.; Allen, M.; Klem, M. T.; Young, M.; Douglas, T., Photochemical Mineralization of Ferritin with Iron(III) citrate. **2006,** *in preparation*.

60. Mayer, D. E.; Rohrer, J. S.; Schoeller, D. A.; Harris, D. C., Fate of Oxygen during Ferritin Iron Incorporation. *Biochemistry* **1983,** 22, 876-880.

61. Chasteen, N. D.; Harrison, P. M., Mineralization in Ferritin: An Efficient Means of Iron Storage. *J. Struct. Biol.* **1999,** 126, (3), 182-194.

62. Douglas, T.; Ripoll, D. R., Calculated electrostatic gradients in recombinant human H-chain ferritin. *Protein Sci.* **1998,** 7, (5), 1083-1091.

63. Theil, E. C.; Takagi, H.; Small, G. W.; He, L.; Tipton, A. R.; Danger, D., The Ferritin Iron Entry and Exit Problem. *Inorganica Chimica Acta* **2000,** 297, 242-251.

64. Yang, X.; Arosio, P.; Chasteen, N. D., Molecular diffusion into ferritin: pathways, temperature dependence, incubation time, and concentration effects. *Biophys. J.* **2000,** 78, (4), 2049-2059.

65. Zhao, G.; Bou-Abdallah, F.; Arosio, P.; Levi, S.; Janus-Chandler, C.; Chasteen, N. D., Multiple Pathways for Mineral Core Formation in Mammalian Apoferritin. The Role of Hydrogen Peroxide. *Biochemistry* **2003,** 42, 3142-3150.

66. Yang, X.; Chen-Barrett, Y.; Arosio, P.; Chasteen, N. D., Reaction Paths of Iron Oxidation and Hydrolysis in Horse Spleen and Recombinant Human Ferritins. *Biochemistry* **1998,** 37, (27), 9743-9750.

67. Bou-Abdallah, F.; Biasiotto, G.; Arosio, P.; Chasteen, N. D., The Putative "Nucleation Site" in Human H-Chain Ferritin is Not Required for Mineralization of the Iron Core. *Biochemistry* **2004,** 43, 4332-4337.

68. Juan, S. H.; Aust, S. D., The Effect of Putative Nucleation Sites on the Loading and Stability of Iron in Ferritin. *Archives of Biochemistry and Biophysics* **1998,** 350, (2), 259-265.

69. Zhao, G.; Arosio, P.; Chasteen, N. D., Iron(II) and Hydrogen Peroxide Detoxification by Human H-Chain Ferritin. An EPR Spin-Trapping Study. *Biochemistry* **2006,** 45, 3429-3436.

70. Santambrogio, P.; Levi, S.; Cozzi, A.; Corsi, B.; Arosio, P., Evidence that the specificity of iron incorporation into homopolymers of human ferritin L- and H-chains is conferred by the nucleation and ferroxidase centres. *Biochem. J.* **1996,** 314, 139-144.

71. Douglas, T.; Stark, V. T., Nanophase Cobalt Oxyhydroxide Mineral Synthesized within the Protein Cage of Ferritin. *Inorg. Chem.* **2000,** 39, 1828-1830.

72. Kim, J. W.; Choi, S. H.; Lillehei, P. T.; Chu, S. H.; King, G. C.; Watt, G. D., Cobalt oxide hollow nanoparticles derived by bio-templating. *Chemical Communications* **2005**, (32), 4101-4103.

73. Tsukamoto, R.; Iwahor, K.; Muraoka, M.; Yamashita, I., Synthesis of Co3O4 nanoparticles using the cage-shaped protein, apoferritin. *Bulletin of the Chemical Society of Japan* **2005,** 78, (11), 2075-2081.

74. Mackle, P.; Charnock, J. M.; Garner, C. D.; Meldrum, F. C.; Mann, S., Characterisation of the manganese core of reconstituted ferritin by X-ray absorption spectroscopy. *JACS* **1994**.

75. Mann, S.; Meldrum, F. C., Controlled synthesis of inorganic materials using supramolecular assemblies. *Adv. Mat.* **1991,** 3, 316-318.

76. Meldrum, F. C.; Douglas, T.; Levi, S.; Arosio, P.; Mann, S., Reconstitution of manganese oxide cores in horse spleen and recombinant ferritins. *J. Inorg. Biochem.* **1995,** 58, 59-68.

77. Zhang, B.; Harb, J. N.; Davis, R. C.; Kim, J. W.; Chu, S. H.; Choi, S.; Miller, T.; Watt, G. D., Kinetic and thermodynamic characterization of the cobalt and manganese oxyhydroxide cores formed in horse spleen ferritin. *Inorganic Chemistry* **2005,** 44, (10), 3738-3745.

78. Douglas, T.; Bulte, J. W. M.; Dickson, D. P. E.; Frankel, R. B.; Pankhurst, Q. A.; Moskowitz, B. M.; Mann, S., Inorganic-Protein Interactions in the Synthesis of a Ferrimagnetic Nanocomposite. In *Hybrid Organic-Inorganic Composites*, Amer Chemical Soc: Washington, 1995; Vol. 585, pp 19-28.

79. Kramer, R. M.; Li, C.; Carter, D. C.; Stone, M. O.; Naik, R. R., Engineered protein cages for nanomaterial synthesis. *Journal of the American Chemical Society* **2004,** 126, (41), 13282-13286.

80. Meldrum, F. C.; Heywood, B. R.; Mann, S., Magnetoferritin - Invitro Synthesis of a Novel Magnetic Protein. *Science* **1992,** 257, (5069), 522-523.

81. Polanams, J.; Ray, A. D.; Watt, R. K., Nanophase iron phosphate, iron arsenate, iron vanadate, and iron molybdate minerals synthesized within the protein cage of ferritin. *Inorganic Chemistry* **2005,** 44, (9), 3203-3209.

82. Sano, K.; Sasaki, H.; Shiba, K., Utilization of the pleiotropy of a peptidic aptamer to fabricate heterogeneous nanodot-containing multilayer nanostructures. *Journal of the American Chemical Society* **2006,** 128, (5), 1717-1722.

83. Wong, K. K. W.; Douglas, T.; Gider, S.; Awschalom, D. D.; Mann, S., Biomimetic Synthesis and Characterization of Magnetic Proteins (Magnetoferritin). *Chem. Mater.* **1998,** 10, (1), 279-285.

84. Wong, K. K. W.; Mann, S., Biomimetic Synthesis of Cadmium Sulfide Ferritin Nanocomposites. *Advanced Materials* **1996,** 8, 928-932.

85. Stafiej, J.; Dymitrowska, M.; Badiali, J. P., Field theoretic approach of electrified interfaces. *Electrochimica Acta* **1996,** 41, (14), 2107-2113.

86. Atkins, P., *Physical Chemistry*. 6 ed.; W.H. Freeman and Company/Oxford English Press: New York, 1998; p 999.

87. Almiron, M.; Link, A. J.; Furlong, D.; Kolter, R., A novel DNA-binding protein with regulatory and protective roles in starved *Escherichia coli*. *Genes Development* **1992,** 6, 2646-2654.

88. Ceci, P.; Ilari, A.; Falvo, E.; Chiancone, E., The Dps protein of Agrobacterium tumefaciens does not bind to DNA but protects it toward oxidative cleavage. *Journal of Biological Chemistry* **2003,** 278, (22), 20319-20326.

89. Marjorette, M.; Pena, O.; Bullerjahn, G. S., The DpsA Protein of *Synechococcus* sp. Strain PCC7942 Is a DNA-binding Hemoprotein. *The Journal of Biological Chemistry* **1995,** 270, (38), 22478-22482.

90. Reindel, S.; Schmidt, C. L.; Anemuller, S.; Matzanke, B. F., Characterization of a non-haem ferritin of the Archaeon Halobacterium salinarum, homologous to Dps (starvation-induced DNA-binding protein). *Biochemical Society Transactions* **2002,** 30, 713-715.

91. Ishikawa, T.; Mizunoe, Y.; Kawabata, S.; Takade, A.; Harada, M.; Wai, S. N.; Yoshida, S., The Iron-Binding Protein Dps Confers Hydrogen Peroxide Stress Resistance to *Campylobacter jejuni*. *Journal of Bacteriology* **2003,** 185, (3), 1010-1017.

92. Stefanini, S.; Cavallo, S.; Montagnini, B.; Chiancone, E., Incorporation of iron by the unusual dodecameric ferritin from Listeria innocua. *Biochemical Journal* **1999,** 338, 71-75.

93. Ilari, A.; Stefanini, S.; Chiancone, E.; Tsernoglou, D., The dodecameric ferritin from *Listeria innocua* contains a novel intersubunit iron-binding site. *Nature Structral Biology* **2000,** 7, 38-43.

94. Harrison, S. C.; Skehel, J. J.; Wiley, D. C., Virus structure. In *Fundamental Virology*, Fields, B. N.; Knipe, D. M.; Howley, P. K., Eds. Lippincott-Raven: New York, N.Y, 1996; pp 59-99.

95. Caspar, D. L. D.; Klug, A., Physical principles in the construction of regular viruses. *Cold Spring Harbor Symp. Quant. Biol.* **1962,** 27, 1-24.

96. Baker, T. S.; Johnson, J. E., Principles of virus structure. In *Structural Biology of Viruses*, Chiu, W.; Burnett, R. M.; R.L., G., Eds. Oxford University Press: New York, N.Y, 1997; pp 38-79.

97. Speir, J. A.; Munshi, S.; Baker, T. S.; Johnson, J. E., Preliminary-X-Ray Data-Analysis of Crystalline Cowpea Chlorotic Mottle Virus. *Virology* **1993,** 193, (1), 234-241.

98. Allison, R.; Janda, M.; Ahlquist, P., Infectious *in vitro* transcripts from cowpea chlorotic mottle virus cDNA clones and exchange of individaul RNA components with brome mosaic virus. *J. Virol.* **1988,** 62, 3581-3588.

99. Bancroft, J. B.; Hiebert, E., Formation of an infectious nucleoprotein from protein and nucleic acid isolated from a small spherical virus. *Virology* **1967,** 32, 354-356.

100. Bancroft, J. B.; Wagner, G. W.; Bracker, C. E., The self-assembly of a nucleic-acid free pseudo-top component for a small spherical virus. **1968**, 146-149.

101. Tama, F.; Brooks, C. L., The mechanism and pathway of pH induced swelling in cowpea chlorotic mottle virus. *Journal of Molecular Biology* **2002,** 318, (3), 733-747.

102. Brumfield, S.; Willits, D.; Tang, L.; Johnson, J. E.; Douglas, T.; Young, M., Heterologous expression of the modified coat protein of Cowpea chlorotic mottle bromovirus results in the assembly of protein cages with altered architectures and function. *Journal of General Virology* **2004,** 85, 1049-1053.

103. Holm, R. H.; Kennepohl, P.; Solomon, E. I., Structural and Functional Aspects of Metal Sites in Biology. *Chemical Reviews* **1996,** 96, 2239-2314.

104. Rayment, I.; Johnson, J. E.; Rossmann, M. G., Metal-free Southern Bean Mosaic Virus Crystals. *The Journal of Biological Chemistry* **1979,** 254, (12), 5243-5245.

105. Hiebert, E.; Bancroft, J. B., Factors affecting the assembly of some spherical viruses. *Virology* **1969,** 39, 296-311.

106. Smith, T. J.; Perry, K. L., Metal Binding Site in Cucumber Mosaic Virus. **2006,** *In preparation*.

107. Ng, J. C. K.; Josefsson, C.; Clark, A. J.; Franz, A. W. E.; Perry, K. L., Virion stability and aphid vector transmissibility of Cucumber mosaic virus mutants. *Virology* **2005,** 332, (1), 397-405.

108. Ng, J. C. K.; Liu, S. J.; Perry, K. L., Cucumber mosaic virus mutants with altered physical properties and defective in aphid vector transmission. *Virology* **2000,** 276, (2), 395-403.

109. Perry, K. L.; Zhang, L.; Palukaitis, P., Amino acid changes in the coat protein of cucumber mosaic virus differentially affect transmission by the aphids Myzus persicae and Aphis gossypii. *Virology* **1998,** 242, (1), 204-210.

110. Perry, K. L.; Zhang, L.; Shintaku, M. H.; Palukaitis, P., Mapping Determinants in Cucumber Mosaic-Virus for Transmission by Aphis-Gossypii. *Virology* **1994,** 205, (2), 591-595.

111. Brittain, H. G.; Richardson, F. S.; Martin, R. B., Terbium(III) Emission as a Probe of Calcium(II) Binding Sites in Proteins. *Journal of the American Chemical Society* **1976,** 98, (25), 8255-8260.

112. Richardson, F. S., Terbium(III) and Europium(III) Ions as Luminscent Probes and Stains for Biomolecular Systems. *Chemical Reviews* **1982,** 82, 541-552.

113. Fogg, D. E.; Radzilowski, L. H.; Dabbousi, B. O.; Schrock, R. R.; Thomas, E. L.; Bawendi, M. G., Fabrication of Quantum Dot-Polymer Composites: Semiconductor Nanoclusters in Dual-Function Polymer Matrixes with Electron-Transporting and Cluster-Passivating Properties. *Macromolecules* **1997,** 30, (26), 8433-8439.

114. Heine, J. R.; Rodriguez-Viejo, J.; Bawendi, M. G.; Jensen, K. F., Synthesis of CdSe quantum dot-ZnS matrix thin films via electrospray organometallic chemical vapor deposition. *J. Cryst. Growth* **1998,** 195, (1-4), 564-568.

115. Jiang, H.; Chen, Y. J.; Lian, G. D., Sputtered FeCoN soft magnetic thin films with high resistivity. *Ieee Transactions on Magnetics* **2003,** 39, (6), 3559-3562.

116. Meldrum, F. C.; Kotov, N. A.; Fendler, J. H., Formation of Thin Films of Platinum, Palladium, and Mixed Platinum: Palladium Nanocrystallites by the Langmuir Monolayer Technique. *Chem. Mater.* **1995,** 7, (6), 1112-16.

117. Guo, Q.; Teng, X.; Rahman, S.; Yang, H., Patterned Langmuir-Blodgett Films of Monodisperse Nanoparticles of Iron Oxide Using Soft Lithography. *Journal of the American Chemical Society* **2002,** 125, 630-631.

118. Hyeon, T.; Lee, S. S.; Park, J.; Chung, Y.; Na, H. B., Synthesis of Highly Crystalline and Monodisperse Maghemite Nanocrystallites without a Size-selection Process. *Journal of the American Chemical Society* **2001,** 123, 12798-12801.

119. Kang, Y. S.; Risbud, S.; Rabolt, J. F.; Stroeve, P., Synthesis and Characterization of Nanometer-Size Fe3O4 and g-Fe2O3 particles. *Chemistry of Materials* **1996,** 8, 2209-2211.

120. Zeng, H.; Jing, L.; Wang, Z. L.; Liu, J. P.; Sun, S., Bimagnetic Core/Shell FePt/Fe3O4 Nanoparticles. *Nano Letters* **2004,** 4, (1), 187-190.

121. Zhang, Z. J.; Wang, Z. L.; Chakoumakos, B. C.; Yin, J. S., Temperature Dependence of Cation Distribtuion and Oxidation State in Magnetic Mn-Fe Ferrite Nanocrystals. *Journal of the American Chemical Society* **1998,** 120, 1800-1804.

122. Jana, N. R.; Chen, Y.; Peng, X., Size- and Shape-Controlled Magnetic (Cr, Mn, Fe, Co, Ni) Oxide Nanocrystals via a Simple and General Approach. *Chemistry of Materials* **2004,** 16, 3931-3935.

123. Yu, L.; Banerjee, I. A.; Matsui, H., Direct Growth of Shape-Controlled Nanocrystals on Nanotubes via Biological Recognition. *Journal of the American Chemical Society* **2003,** 125, 14837-14840.

124. Mann, S., *Biomimetic Materials Chemistry*. VCH Publishers: New York, 1996.

125. Nedoloujko, A.; Kiwi, J., Parameters affecting the homogeneous and heterogeneous degradation of quinoline solutions in light-activated processes. . *Journal of Photochemistry and Photobiology A-Chemistry* **1997,** 110, (2), 149-157.

126. Finsy, R., Particle Sizing by Quasi-Elastic Light-Scattering. *Advances in Colloid and Interface Science* **1994,** 52, 79-143.

127. Structure file 9362 (Co3O4), I. C. S. D., Karlsruhe, Germany.

128. Powder Diffraction File 07-0169 (Heterogenite Co(O)OH, J. C. o. P. D. S., Swarthmore, PA, In.

129. Flenniken, M. L.; Willits, D. A.; Brumfield, S.; Young, M. J.; Douglas, T., The Small Heat Shock Protein from Methanococcus jannaschii is a Versatile Nano-scale Platform for Genetic and Chemical Modification. *Nano Letters* **2003,** 3, 1573-1576.

130. Slocik, J. M.; Naik, R. R.; Stone, M. O.; Wright, D. W., Viral templates for gold nanoparticle synthesis. *Journal of Materials Chemistry* **2005,** 15, (7), 749-753.

131. Varpness, Z.; Peters, J. W.; Young, M.; Douglas, T., Biomimetic synthesis of a H-2 catalyst using a protein cage architecture. *Nano Letters* **2005,** 5, (11), 2306-2309.

132. Akerman, M. E.; Chan, W. C. W.; Laakkonen, P.; Bhatia, S. N.; Ruoslahti, E., Nanocrystal targeting in vivo. *Proceedings of the National Academy of Sciences of the United States of America* **2002,** 99, (20), 12617-12621.

133. Mao, C. B.; Flynn, C. E.; Hayhurst, A.; Sweeney, R.; Qi, J. F.; Georgiou, G.; Iverson, B.; Belcher, A. M., Viral assembly of oriented quantum dot nanowires. *Proceedings of the National Academy of Sciences of the United States of America* **2003,** 100, (12), 6946-6951.

134. Mao, C. B.; Solis, D. J.; Reiss, B. D.; Kottmann, S. T.; Sweeney, R. Y.; Hayhurst, A.; Georgiou, G.; Iverson, B.; Belcher, A. M., Virus-based toolkit for the directed synthesis of magnetic and semiconducting nanowires. *Science* **2004,** 303, (5655), 213-217.

135. Okuda, K.; Urabe, I.; Yamada, Y.; Okada, H., Reaction of Glutaraldehyde with Amino and Thiol Compounds. *Journal of Fermentation and Bioengineering* **1991,** 71, (2), 100-105.

136. Wong, S. S., Chemistry of Protein Conjugation and Cross-Linking. In CRC Press, Inc.: Boca Raton, Florida, 1991.

137. Conway, J. F., Cheng, N., Zlotnick, A., Wingfield, P.T., Stahl, S.J., Steven, A.C., Virus Capsid by Cryo-electron Microscopy. *Nature* **1997,** 386, 91-94.

138. Jiles, D., *Introduction to Magnetism and Magnetic Materials*. Chapman and Hall: New York, 1998; p 535.

139. Kilcoyne, S. H.; Cywinski, R., Ferritin - a Model Superparamagnet. *Journal of Magnetism and Magnetic Materials* **1995,** 140, 1466-1467.

140. Lu, S.; Ke, Y.; Li, J.; Zhang, Y., Synthesis, structure and characterizations of a molybdenum sulfide complex with inorganic cluster [Mo-3 S-13](2-) and organic amine Me4N+. *Crystal Research and Technology* **2002,** 37, (11), 1153-1159.

141. Mastai, Y.; Homyonfer, M.; Gedanken, A.; Hodes, G., Room temperature sonoelectrochemical synthesis of molybdenum sulfide fullerene-like nanoparticles. *Advanced Materials* **1999,** 11, (12), 1010-1013.

142. Paskach, T. J.; Hilsenbeck, S. J.; Thompson, R. K.; McCarley, R. E.; Schrader, G. L., Synthesis and characterization of a novel platinum molybdenum sulfide containing the Mo6S8 cluster. *Journal of Alloys and Compounds* **2000,** 311, (2), 169-180.

143. Hinnemann, B.; Moses, P. G.; Bonde, J.; Jorgensen, K. P.; Nielsen, J. H.; Horch, S.; Chorkendorff, I.; Norsdov, J. K., Biomimetic Hydrogen Evolution: MoS2 Nanoparticles as Catalyst for Hydrogen Evolution. *Journal of the American Chemical Society* **2005,** 127, 5308-5309.

144. Fox, J. M.; Zhao, X. X.; Speir, J. A.; Young, M. J., Analysis of a salt stable mutant of cowpea chlorotic mottle virus. *Virology* **1996,** 222, (1), 115-122.

145. MinCryst, www.mincryst.com/English. In.

146. Tenne, *et al.*

147. Kisielowski, C.; Hetherington, C. J. D.; Wang, Y. C.; Kilaas, R.; O'Keefe, M. A.; Thust, A., Imaging columns of the light elements carbon, nitrogen and oxygen with sub angstrom resolution. *Ultramicroscopy* **2001,** 89, 243-263.

148. Banin, U.; Lee, C. J.; Guzelian, A. A.; Kadavanich, A. V.; Alivisatos, A. P.; Jaskolski, W.; Bryant, G. W.; Efros, A. L.; Rosen, M., Size-dependent electronic level structure of InAs nanocrystal quantum dots: Test of multi-band effective mass theory. *J. Chem. Phys.* **1998,** 109, (6), 2306-2309.

149. Bawendi, M. G., Synthesis and spectroscopy of II-VI quantum dots: An overview. *NATO ASI Ser., Ser. B* **1995,** 340, (Confined Electrons and Photons), 339-56.

150. Dabbousi, B. O.; Onitsuka, O.; Rubner, M. F.; Bawendi, M. g., Size dependent electroluminescence from CdSe nanocrystallites (quantum dots). *Mater. Res. Soc. Symp. Proc.* **1995,** 358, (Microcrystalline and Nanocrystalline Semiconductors), 707-12.

151. Alivisatos, A. P., Semiconductor clusters, nanocrystals, and quantum dots. *Science* **1996,** 271, (5251), 933-7.

152. Alivisatos, A. P., Colloidal semiconductor quantum dots. *Abstr. Pap. - Am. Chem. Soc.* **2000,** 220th, HYS-524.

153. Klem, M. T.; Gilmore, K.; Allen, M.; Hollroyd, J.; Resnick, D.; Idzerda, Y., X-ray Absorption Spectroscopy of Protein Encapsulated Nano-particles. In National Synchrotron Light Source: 2003.

154. Gilmore, K.; Klem, M. T.; Allen, M.; Young, M.; Douglas, T.; Idzerda, Y., Surface contribution to the Anisotropy Energy of Spherical Magnetite Particles. *Journal of Applied Physics* **2005,** 97, 10B301-1-3.

155. Usselman, R. J.; Klem, M. T.; Allen, M.; Walter, E. D.; Gilmore, K.; Douglas, T.; Young, M.; Idzerda, Y.; Singel, D. J., Electron Magnetic Resonance of Iron Oxide Nanoparticles Mineralized in Protein Cages. *Journal of Applied Physics* **2005,** 97, 10M523-1-3.

156. Incardona, N. l.; McKee, S.; Flanegan, J. B., Noncovalent Interactions in Viruses - Characterization of Their Role in Ph and Thermally Induced Conformational-Changes in Bromegrass Mosaic-Virus. *Virology* **1973,** 53, (1), 204-214.

157. Hsu, H. T.; Aebig, J.; Rochow, W. F., Differences among monoclonal antibodies to barley yellow dwarf viruses. *Phytopathology* **1984,** 74, 600-605.

158. Rayment, I.; Argos, P.; Johnson, J. E., Crystalline Cowpea Chlorotic Mottle Virus. *Journal of Ultrastructure Research* **1977,** 61, (2), 240-242.

159. Sorger, P. G.; Stockley, P. G.; Harrison, S. C., Structure and assembly of turnip crinkle virus II. Mechanism of reassembly *in vitro*. *J. Mol. Biol.* **1986,** 191, 639-658.

160. Hogue, C. W. V.; MacManus, J. P.; Banville, D.; Szabo, A. G., Comparison of Terbium(III) Luminescence Enhancement in Mutants of EF Hand Calcium Binding Proteins. *The Journal of Biological Chemistry* **1992,** 267, (19), 13340-13347.

161. Clark, I. D.; Hill, I.; Sikorska-Walker, M.; MacManus, J. P.; Szabo, A. G., A novel peptide designed for sensitization of terbium(III) luminescence. *FEBS Lett.* **1993,** 333, 96-98.

162. Ye, Y.; Shealy, S.; Lee, H. W.; Torshin, I.; Harrison, R.; Yang, J. J., A grafting approach to obtain site-specific metal-binding properties of EF-hand proteins. *Protein Engineering* **2003,** 16, (6), 429-434.

163. Lane, L. C., The Bromoviruses. In *Handbook of plant virus infection and comparative diagnosis*, Kurstak, E., Ed. Elsevier/North-Holland: Amsterdam, 1981.

164. Johnson, J. M.; Willits, D. A.; Young, M. J.; Zlotnick, A., Interaction with capsid protein alters RNA structure and the pathway for in vitro assembly of Cowpea chlorotic mottle virus. *Journal of Molecular Biology* **2004,** 335, (2), 455-464.

165. Vandergraaf, M.; Kroon, G. J. A.; Hemminga, M. A., Conformation and Mobility of the Rna-Binding N-Terminal Part of the Intact Coat Protein of Cowpea Chlorotic Mottle Virus - a 2-Dimensional Proton Nuclear-Magnetic-Resonance Study. *Journal of Molecular Biology* **1991,** 220, (3), 701-709.

166. Willits, D.; Zhao, X.; Olson, N.; Baker, T. S.; Zlotnick, A.; Johnson, J. E.; Douglas, T.; Young, M. J., Effects of the Cowpea chlorotic mottle bromovirus beta-hexamer structure on virion assembly. *Virology* **2003,** 306, (2), 280-288.

167. Zlotnick, A.; Aldrich, R.; Johnson, J. M.; Ceres, P.; Young, M. J., Mechanism of capsid assembly for an icosahedral plant virus. *Virology* **2000,** 277, (2), 450-456.

168. Flenniken, M. L.; Douglas, T.; Young, M., Cell-specific targeting with CCMV. In Montana State University: 2006.

169. Liepold, L. O.; Revis, J.; Allen, M.; Oltrogge, L.; Young, M.; Douglas, T., Structural transitions in Cowpea chlorotic mottle virus (CCMV). *Physical Biology* **2005,** 2, (4), S166-S172.

170. Hvattum, E.; Normann, P. T.; Jamieson, G. C.; Lai, J. J.; Skotland, T., Detection and Quantitation of Gadolinium Chelates in Human Serum and Urine by High-Performance Liquid-Chromatography and Postcolumn Derivatization of Gadolinium with Arsenazo-Iii. *Journal of Pharmaceutical and Biomedical Analysis* **1995,** 13, (7), 927-932.

171. Anderson, E. A.; Isaacman, S.; Peabody, D. S.; Wang, E. Y.; Canary, J. W.; Kirshenbaum, K., Viral Nanoparticles Donning a Paramagnetic Coat: Conjugation of MRI Contrast Agents to the MS2 Capsid. *Nano Letters* **2006,** *In press*.

172. Palukaitis, P.; Roossinck, M. J.; Dietzgen, R. G.; Francki, R. I. B., Cucmber Mosaic Virus. *Advances in Virus Research* **1992,** 41, 281-348.

173. Wikoff, W. R.; Tsai, C. J.; Wang, G.; Baker, T. S.; Johnson, J. E., The Structure of Cucumber Mosaic Virus: Cryoelectron Microscopy, X-Ray Crystallography, and Sequence Analysis. *Virology* **1997,** 232, 91-97.

174. Vivian, J. T.; Callis, P. R., Mechanisms of Tryptophan Fluorescence Shifts in Proteins. *Biophysical Journal* **2001,** 80, 2093-2109.

APPENDICES

APPENDIX A

IGOR MACRO FOR LOADING DATA FROM THE PHYSICAL PROPERTIES MEASUREMENT SYSTEM

APPENDIX A

Macro for Loading Data from the Physical Properties Measurement System

This macro is an Igor procedure that was written by Michael Klem for taking data from the physical properties measurement system (PPMS). This macro is used for the purpose of interpreting ACMS and VSM data discussed in chapters three and five. The ACMS involves a frequency separator and the VSM will plot moment vs. temperature or field.

Macro:

```
#pragma rtGlobals=1             // Use modern global access method.
// 6/1/03  Started PPMS data handling Macro.
// 6/2/03  Added Display VSM routine, reads waves but does not plot correctly yet.
// 6/16/03  Plot function fixed, yeah!
// 6/16/03 The much delayed frequency Seperator is done!
//.....
// Launches the AC Frequency Seperator

Function ACFrequencySeperatorProc(ctrlName) : ButtonControl
        String ctrlName
        Execute "LoadACFrequencyPanel()"
End

//.....
Window LoadACFrequencyPanel() : Panel
        PauseUpdate; Silent 1           // building window...
        NewPanel /W=(444.75,343.25,668.25,440) as "AC Frequency Seperator"
        DoWindow/C tmp_LoadACFrequencyPanel

        String dfSave = GetDataFolder(1)
        String dfVSM = "root:data:ACMS", srchsrt = "moment_"
        //String wv

        // shift to data folder in Packages to store globals for VSM, ACMS.
        SetDataFolder root:Packages:MainControlPPMS

        // Create global variables used by the control panel.
        String/G GKillPanelName = "tmp_LoadACFrequencyPanel"


        //String wvlist = root:Packages:MainControlPPMS
```

```
	PopupMenu
WaveSelect,pos={26,17},size={167,21},proc=ACFreqSepProc,title="Select File to
Seperate"
	PopupMenu WaveSelect,mode=1,popvalue="Allen",value=
#"DFWaveSearch2(\"root:data:ACMS\",\"ACMoment_\")"
	Button KillButton,pos={62,58},size={99,23},proc=ClosePanelProc,title="Close
When Done"


	SetDataFolder dfSave
EndMacro

//.....
//Calls Seperator

Function ACFreqSepProc(ctrlName,popNum,popStr) : PopupMenuControl
	String ctrlName
	Variable popNum
	String popStr
	ACFreqSep(popStr)

End

//.....
// My kludgy frequency Seperator

Function ACFreqSep(wvname)
	String wvname
	String newfolder
	variable index, stop, numberofpoints, numfreq, notmade, index2, index3
	Variable freqmarker, tmpfreq, tracker, wavesize
	String freq, temp, fieldw, amp, Xrealw, Ximagw, Mom, phasew, tmpwv

	newfolder = "freqsep_" + wvname
	//string dfSave = GetDataFolder(1)
	SetDataFolder root:data:ACMS
	NewDataFolder /O $newfolder  // Creates a new Folder with the user given name
under ACMS

	Wave frequency = $("ACFreq_" + wvname)
	Wave Temperature = $("ACTemp_" + wvname)
	Wave Field = $("ACField_" + wvname)
```

```
	Wave Amplitude = $("ACAmplitude_" + wvname)
	Wave Xreal = $("ACXreal_" + wvname)
	Wave Ximag = $("ACXimag_" + wvname)
	Wave Moment = $("ACMoment_" + wvname)
	Wave phase = $("ACphase_" + wvname)


	freq = "freq_" + wvname
	temp = "temp_" + wvname
	fieldw = "field_" + wvname
	amp = "amplitude_" + wvname
	Xrealw = "Xreal_" + wvname
	Ximagw = "Ximag_" + wvname
	Mom = "moment_" + wvname
	phasew = "phase_" + wvname

	index = 1
	stop = 0
	freqmarker = frequency(0)
	wavestats frequency
	numberofpoints = V_npnts


	do                                                    // Scans the frequency Wave
and determines number of different frequencies present
		if (stop)
			break
		endif

		if (freqmarker == frequency(index))
			stop = 1
		endif

		index += 1

	while (1)

SetDataFolder root:data:ACMS:$newfolder

stop = 0
numfreq = index - 2
index = 0
notmade = 1
wavesize = numberofpoints/(numfreq+1)
```

```
	do                                                                    //
creates frequency seperated waves with the file names
		if (stop)                                                     //
[freq][type]_[user given name]
			break
		endif

		if (notmade)
			if (index == numfreq)
				notmade = 0
				stop = 1
			endif
			tmpfreq = frequency(index)
			tmpwv = num2str(tmpfreq) + freq
			Make/N=(wavesize)/D/O $tmpwv
			tmpwv = num2str(tmpfreq) + temp
			Make/N=(wavesize)/D/O $tmpwv
			tmpwv = num2str(tmpfreq) + fieldw
			Make/N=(wavesize)/D/O $tmpwv
			tmpwv = num2str(tmpfreq) + amp
			Make/N=(wavesize)/D/O $tmpwv
			tmpwv = num2str(tmpfreq) + Xrealw
			Make/N=(wavesize)/D/O $tmpwv
			tmpwv = num2str(tmpfreq) + Ximagw
			Make/N=(wavesize)/D/O $tmpwv
			tmpwv = num2str(tmpfreq) + Mom
			Make/N=(wavesize)/D/O $tmpwv
			tmpwv = num2str(tmpfreq) + phasew
			Make/N=(wavesize)/D/O $tmpwv
		Endif

		index += 1

	while (1)

	stop = 0
	index3 = 0
	index2 = 0
	index = 0
	tmpfreq = frequency(index)
```

```
        do                                                              // Now
the wave writing begins
                if (stop)
                        break
                endif

                if (index3 <= numfreq)                                  //  Tracker is
just a debugging variable
                        if (index <= (numberofpoints-1))
                                tmpwv = num2str(tmpfreq) + freq
                                wave temp2 = $tmpwv
                                tracker = frequency ((index + index3))
                                temp2[index2] = frequency((index + index3))
                                Redimension/N=(wavesize) temp2

                                tmpwv = num2str(tmpfreq) + temp
                                wave temp2 = $tmpwv
                                tracker = Temperature((index + index3))
                                temp2[index2] = Temperature((index + index3))
                                Redimension/N=(wavesize) temp2


                                tmpwv = num2str(tmpfreq) + fieldw
                                wave temp2 = $tmpwv
                                tracker = Field((index + index3))
                                temp2[index2] = Field((index + index3))
                                Redimension/N=(wavesize) temp2

                                tmpwv = num2str(tmpfreq) + amp
                                wave temp2 = $tmpwv
                                tracker = Amplitude((index + index3))
                                temp2[index2] = Amplitude((index + index3))
                                Redimension/N=(wavesize) temp2

                                tmpwv = num2str(tmpfreq) + Xrealw
                                wave temp2 = $tmpwv
                                tracker = Xreal((index + index3))
                                temp2[index2] = Xreal((index + index3))
                                Redimension/N=(wavesize) temp2

                                tmpwv = num2str(tmpfreq) + Ximagw
                                wave temp2 = $tmpwv
                                tracker = Ximag((index + index3))
```

```
                        temp2[index2] = Ximag((index + index3))
                        Redimension/N=(wavesize) temp2

                        tmpwv = num2str(tmpfreq) + Mom
                        wave temp2 = $tmpwv
                        tracker = Moment((index + index3))
                        temp2[index2] = Moment((index + index3))
                        Redimension/N=(wavesize) temp2

                        tmpwv = num2str(tmpfreq) + phasew
                        wave temp2 = $tmpwv
                        tracker = phase((index + index3))
                        temp2[index2] = phase((index + index3))
                        Redimension/N=(wavesize) temp2

                        index2 +=1
                        index += (numfreq + 1)
                endif

                if (index > (numberofpoints-1))
                        index3 += 1
                        index = 0
                        index2 = 0
                        tmpfreq = frequency(index+index3)
                endif

                if (index3>numfreq)
                        stop = 1
                endif

        endif

    while(1)

End


//.....
//This function returns the names of waves in a data folder (DF) that match a search
criteria.  It takes as parameters the full
//path to the DF and the search string.  The function only performs searches for waves
that begin with a certain string.  Future
//versions will allow for more refined searches.  The names of the matching waves are
returned via a string list.
```

```
Function/S DFWaveSearch2(dfname,matchstr)
	string dfname, matchstr

	variable matchlen = strlen(matchstr)
	variable counter, totwv, index = 0
	string tmpwv ="", wvlist =""
	string appendedname =""
//	Print "Past the declarations"

	counter = matchlen - 1
	totwv = CountObjects(dfname,1)			//The "1" flag counts only
waves in the DF


	do
		if ( index == totwv)
			break
	//terminates the while loop
		endif
		tmpwv = GetIndexedObjName(dfname,1,index)		//Get the name
of the wave

		if (cmpstr(tmpwv[0,matchlen -1],matchstr) == 0)		//If the wave
name matches the search criteria, add it to the list
			sscanf tmpwv, "ACMoment_%s", appendedname
			wvlist += appendedname + ";"
		endif

		index += 1

	while (1)
	return wvlist
	//return the list of wave names
End

//.....
// This function defines the path to where the data files are stored

Function ChoosePathProc(ctrlName) : ButtonControl
	String ctrlName
	NewPath /O/Q/M="Use the Browse button to select data folder" DataPath
	PathInfo DataPath
	//Sets the S_path variable
```

```
		String PathAlert = "The data loading path is now " + S_path + "."
		DoAlert 0, PathAlert
		Print PathAlert
End

//.....
// Load VSM button definition.  Calls the Load VSM panel

Function LoadVSMProc(ctrlName) : ButtonControl
		String ctrlName
		Execute "LoadVSMPanel()"
End

//.....
// Load ACMS button definition.  Calls the Load ACMS panel

Function LoadACMSProc(ctrlName) : ButtonControl
		String ctrlName
		Execute "LoadACMSPanel()"
End

//.....
Function DisplaySingleVSMProc(ctrlName) : ButtonControl
		String ctrlName
		Execute "DisplaySingleVSMPanel()"
End

//.....
// Load VSM Window, I hope

Window LoadVSMPanel() : Panel
		PauseUpdate; Silent 1		// building window...
		NewPanel /K=2 /W=(621.75,233,866.25,512) as "Load VSM Spectrum"
		DoWindow/C tmp_LoadVSMPanel

		String dfSave = GetDataFolder(1)

		// shift to data folder in Packages to store globals for VSM, ACMS
		SetDataFolder root:Packages:MainControlPPMS

		// Create global variables used by the control panel.
		String fname = StrVarOrDefault(":Gfname", "filename")
		String/G Gfname = fname
		String/G GKillPanelName = "tmp_LoadVSMPanel"
```

```
	String ftype = StrVarOrDefault(":Gftype", "scantype")
	String/G Gftype = "VSM"
	String/G appendwavename

	// Draw Control box for VSM file loading
	SetDrawEnv fsize= 18,fstyle= 1
	DrawText 88,176,"OR"
	DrawText 23,16,"Select a name to append on the"
	DrawText 38,35,"waves.  Short and no spaces!!!"
	SetDrawEnv fsize= 18,fstyle= 1
	DrawText 75,103,"THEN"
	Button
ChooseFile,pos={69,114},size={75,21},proc=ChooseFileProc,title="Choose File"
	SetVariable
filename,pos={18,194},size={185,16},proc=TypeFileProc,title="Type in File Name"
	SetVariable filename,limits={-Inf,Inf,1},value=
root:Packages:MainControlPPMS:Gfname
	Button KillButton,pos={55,232},size={99,23},proc=ClosePanelProc,title="Close
When Done"
	SetVariable appendname,pos={11,45},size={200,16}
	SetVariable appendname,value=
root:Packages:MainControlPPMS:appendwavename

	SetDataFolder dfSave
	Print fname
EndMacro

//.....
// Load ACMS Window

Window LoadACMSPanel() : Panel
	PauseUpdate; Silent 1		// building window...
	NewPanel /K=2 /W=(621.75,233,866.25,512) as "Load ACMS Spectrum"
	DoWindow/C tmp_LoadACMSPanel

	String dfSave = GetDataFolder(1)

	// shift to data folder in Packages to store globals for VSM, ACMS
	SetDataFolder root:Packages:MainControlPPMS

	// Create global variables used by the control panel.
	String fname = StrVarOrDefault(":Gfname", "filename")
	String/G Gfname = fname
	String/G GKillPanelName = "tmp_LoadACMSPanel"
```

```
	String ftype = StrVarOrDefault(":Gftype", "scantype")
	String/G Gftype = "ACMS"
	String/G appendwavename

	// Draw ACMS load file window
	SetDrawEnv fsize= 18,fstyle= 1
	DrawText 88,176,"OR"
	DrawText 23,16,"Select a name to append on the"
	DrawText 38,35,"waves.  Short and no spaces!!!"
	SetDrawEnv fsize= 18,fstyle= 1
	DrawText 75,103,"THEN"
	Button
ChooseFile,pos={69,114},size={75,21},proc=ChooseFileProc,title="Choose File"
	SetVariable
filename,pos={18,194},size={185,16},proc=TypeFileProc,title="Type in File Name"
	SetVariable filename,limits={-Inf,Inf,1},value=
root:Packages:MainControlPPMS:Gfname
	Button KillButton,pos={55,232},size={99,23},proc=ClosePanelProc,title="Close
When Done"
	SetVariable appendname,pos={11,45},size={200,16}
	SetVariable appendname,value=
root:Packages:MainControlPPMS:appendwavename

	SetDataFolder dfSave
	Print fname
EndMacro

//.....
// Add a menu item to display the control panel
Menu "Macros"
	"Display Main PPMS Control Panel", DisplayMainPPMSControlPanel()
End

//.....
// This is a top level routine which makes sure that the globals
// and their data folders exist and then make sure the control
// panel is displayed.
// Stolen from page 1118 of Igor Manual (pdf)!

Function DisplayMainPPMSControlPanel()
	// If the panel exists just bring it to the front
	DoWindow/F MainPPMSControlPanel  // Brings the Window to the Front
	if (V_Flag != 0)  // Check verify Flag for windows existance
		return 0
```

```
	endif

	String dfSave = GetDataFolder(1)

	// Create Daa folders to store PPMS Data
	NewDataFolder/O root:data
	NewDataFolder/O root:data:VSM
	NewDataFolder/O root:data:ACMS

	// Create a folder in Packages to store globals.
	NewDataFolder/O/S root:Packages
	NewDataFolder/O/S root:Packages:MainControlPPMS

	// Create the Control Panel
	Execute "MainPPMSControlPanel()"
	SetDataFolder dfSave

End

//.....
//This function loads general text waves via a Windows dialog box
Function ChooseFileProc(ctrlName) : ButtonControl
	String ctrlName
	variable scanwaves
	string scantype

	String dfSave = GetDataFolder(1)

	//Check to see which type of scan is supposed to be loaded, set the expected
number of waves, and the data folder
	SetDataFolder root:Packages:MainControlPPMS
	scantype = StrVarOrDefault(":Gftype", "scantype")		//Gftype stores the
scan type

	if (cmpstr(scantype,"VSM") == 0)					//Set
number of columns to be entered.  This is used
		scanwaves = 3
	//in the RenameWaves() function
		SetDataFolder root:data:VSM
	elseif (cmpstr(scantype,"ACMS") == 0)
		scanwaves = 10
		SetDataFolder root:data:ACMS
	endif
```

```
	if (cmpstr(scantype, "VSM") == 0)				//If
statement controls how the data is loaded between VSM and ACMS outputs
		LoadWave /O/J/L={21,22,0,2,3}/N=tmp/P=DataPath		//LoadWave
via Windows dialog box {nameLine, firstline, numLines, first Colum, numColumns}
	elseif (cmpstr(scantype, "ACMS") == 0)
		LoadWave /O/J/L={20,21,0,2,10}/N=tmp/P=DataPath
	endif

	If (V_flag != scanwaves)
	//Check for proper number of waves.  If wrong, go to error handling routine
		WaveInputErrorProc(V_flag)
		SetDataFolder dfSave
	//Return to prior data folder
		Abort
	endif

	// Set name of file just loaded into global variable
	String dfSave2 = GetDataFolder(1)
	SetDataFolder root:Packages:MainControlPPMS
	String/G Gfname = S_fileName
	SetDataFolder dfSave2

	RenameWaves(scanwaves)
			//Drop to routine that renames the waves
	SetDataFolder dfSave
					//Return to prior data folder
End

//.....
Function WaveInputErrorProc(loadwavenum)
	Variable loadwavenum
	string scantype, alertstr, wavekill
	variable scanwaves
	string dfSave = GetDataFolder(1)
	//save current data folder position
	SetDataFolder root:Packages:MainControlPPMS			//switch to
location of global variables

	scantype = StrVarOrDefault(":Gftype", "scantype")
	if (cmpstr(scantype,"VSM") == 0)
		scanwaves = 3
	elseif (cmpstr(scantype,"ACMS") == 0)
		scanwaves = 10
	endif
```

```
	SetDataFolder dfSave
	//switch back to original data folder
	variable i
	if (loadwavenum < scanwaves)
		alertstr = "Warning!  Fewer waves than expected for " + scantype + " scan loaded.  Kill these waves?"
		DoAlert 1, alertstr
		// DoAlert 1 puts up alert w/ yes/no button
		if (V_flag == 1)
			//V_flag set by alert window.  1 = "YES"
			For (i = loadwavenum; i > 0; i -= 1)
				wavekill = "tmp" + num2str(i - 1)
				//Print wavekill
				KillWaves $wavekill
			EndFor
		else
			Abort "You must Rename the 'tmp*' waves by hand or they will be over-written on the next load file command."
		endif
	elseif (loadwavenum > scanwaves)
		alertstr = "Warning!  More waves than expected for " + scantype + " scan loaded.  Kill these waves?"
		DoAlert 1, alertstr
		// DoAlert 1 puts up alert w/ yes/no button
		if (V_flag == 1)
			For (i = loadwavenum; i > 0; i -= 1)
				wavekill = "tmp" + num2str(i - 1)
				//Print i, wavekill
				KillWaves $wavekill
			EndFor
		else
			Abort "You must Rename the 'tmp*' waves by hand or they will be over-written on the next load file command."
		endif
	endif
End


//.....
//This function renames the "tmp" waves from the general text load command with the proper file number identifier
Function RenameWaves(scanwaves)
	variable scanwaves
```

```
string tmpwv, nwwv, susc, field
Svar appendname = root:Packages:MainControlPPMS:appendwavename



if (scanwaves == 3)
	//Rename the temporary waves w/ the file number
	tmpwv = "tmp0"
	nwwv = "Temper_" + appendname
	Duplicate /o  $tmpwv, $nwwv; KillWaves $tmpwv
	tmpwv = "tmp1"
	nwwv = "Field_" + appendname
	field = nwwv
	Duplicate /o  $tmpwv, $nwwv; KillWaves $tmpwv
	tmpwv = "tmp2"
	nwwv = "Moment_" + appendname
	Duplicate /o  $tmpwv, $nwwv; KillWaves $tmpwv
	susc = "Suscep_" + appendname
	Duplicate /o $nwwv $susc
elseif (scanwaves == 10)
	//Rename the temporary waves w/ the file number
	killwaves tmp4, tmp5
	tmpwv = "tmp0"
	nwwv = "ACTemp_" + appendname
	Duplicate /o  $tmpwv, $nwwv; KillWaves $tmpwv
	tmpwv = "tmp1"
	nwwv = "ACField_" + appendname
	Duplicate /o  $tmpwv, $nwwv; KillWaves $tmpwv
	tmpwv = "tmp2"
	nwwv = "ACFreq_" + appendname
	Duplicate /o  $tmpwv, $nwwv; KillWaves $tmpwv
	tmpwv = "tmp3"
	nwwv = "ACAmplitude_" + appendname
	Duplicate /o  $tmpwv, $nwwv; KillWaves $tmpwv
	tmpwv = "tmp6"
	nwwv = "ACXreal_" + appendname
	Duplicate /o  $tmpwv, $nwwv; KillWaves $tmpwv
	tmpwv = "tmp7"
	nwwv = "ACXimag_" + appendname
	Duplicate /o  $tmpwv, $nwwv; KillWaves $tmpwv
	tmpwv = "tmp8"
	nwwv = "ACMoment_" + appendname
	Duplicate /o  $tmpwv, $nwwv; KillWaves $tmpwv
	tmpwv = "tmp9"
```

```
                nwwv = "ACphase_" + appendname
                Duplicate /o  $tmpwv, $nwwv; KillWaves $tmpwv
        endif
End

//.....
//This function kills the referenced Panel Window
Function ClosePanelProc(ctrlName) : ButtonControl
        String ctrlName
        SVAR GKillPanelName = root:Packages:MainControlPPMS:GKillPanelName
        DoWindow/K $GKillPanelName
End

//.....
//This function loads general text waves by typing in the data file name
Function TypeFileProc(ctrlName,varNum,varStr,varName) : SetVariableControl
        String ctrlName
        Variable varNum
        String varStr
        String varName
        variable scanwaves
        String scantype
        String dfSave = GetDataFolder(1)                        //save current data
folder reference

        //Check to see which type of scan is supposed to be loaded, set the expected
number of waves, and the data folder
        SetDataFolder root:Packages:MainControlPPMS
        scantype = StrVarOrDefault(":Gftype", "scantype")       //Gftype stores the
scan type
        if (cmpstr(scantype,"VSM") == 0)
                scanwaves = 3
                SetDataFolder root:data:VSM
        elseif (cmpstr(scantype,"ACMS") == 0)
                scanwaves = 10
                SetDataFolder root:data:ACMS
        endif

        if (cmpstr(scantype, "VSM") == 0)
                LoadWave /O/J/L={21,22,0,2,3}/N=tmp/P=DataPath varStr
//LoadWave via direct input {nameLine, firstline, numLines, first Colum, numColumns}
        elseif (cmpstr(scantype, "ACMS") == 0)
                LoadWave /O/J/L={20,21,0,2,10}/N=tmp/P=DataPath varStr
        endif
```

```
	If (V_flag != scanwaves)
	//Check for proper number of waves.  If wrong, go to error handling routine
		WaveInputErrorProc(V_flag)
		SetDataFolder dfSave
	//Return to prior data folder
		Abort
	endif

	// Set name of file just loaded into global variable
	String dfSave2 = GetDataFolder(1)
	SetDataFolder root:Packages:MainControlPPMS
	String/G Gfname = S_fileName
	SetDataFolder dfSave2

	RenameWaves(scanwaves)				//Drop to routine that
renames the waves
	SetDataFolder dfSave					//Return to prior data
folder
End

//.....
//This function returns the names of waves in a data folder (DF) that match a search
criteria.  It takes as parameters the full
//path to the DF and the search string.  The function only performs searches for waves
that begin with a certain string.  Future
//versions will allow for more refined searches.  The names of the matching waves are
returned via a string list.

Function/S DFWaveSearch(dfname,matchstr)
	string dfname, matchstr

	variable matchlen = strlen(matchstr)
	variable counter, totwv, index = 0
	string tmpwv ="", wvlist =""
	string appendedname =""
//	Print "Past the declarations"

	counter = matchlen - 1
	totwv = CountObjects(dfname,1)			//The "1" flag counts only
waves in the DF


	do
```

```
		if ( index == totwv)
			break
	//terminates the while loop
		endif
		tmpwv = GetIndexedObjName(dfname,1,index)		//Get the name
of the wave

		if (cmpstr(tmpwv[0,matchlen -1],matchstr) == 0)		//If the wave
name matches the search criteria, add it to the list
			sscanf tmpwv, "Moment_%s", appendedname
			wvlist += appendedname + ";"
		endif

		index += 1

	while (1)
	return wvlist
	//return the list of wave names
End

//-------------------------------------------------------------------------------------------------------
----------------------
Window DisplaySingleVSMPanel() : Panel
	PauseUpdate; Silent 1		// building window...
	NewPanel /W=(444.75,343.25,804,476.75) as "Graph Single VSM run"
	DoWindow/C tmp_DisplaySingleVSMPanel

	String dfSave = GetDataFolder(1)
	String dfVSM = "root:data:VSM", srchsrt = "moment_"
	//String wv

	// shift to data folder in Packages to store globals for VSM, ACMS.
	SetDataFolder root:Packages:MainControlPPMS

	// Create global variables used by the control panel.
	String/G GKillPanelName = "tmp_DisplaySingleVSMPanel"
	Variable/G VSM_MvsT, VSM_MvsH, VSM_XvsT

	//String wvlist = root:Packages:MainControlPPMS


	PopupMenu
WaveSelect,pos={6,47},size={167,21},proc=GraphSingleVSMProc,title="Select File to
Graph"
```

```
	PopupMenu WaveSelect,mode=1,popvalue="Allen",value=
#"DFWaveSearch(\"root:data:VSM\",\"moment_\")"
	Button
KillButton,pos={127,106},size={99,23},proc=ClosePanelProc,title="Close When Done"
	CheckBox plot1,pos={195,23},size={133,14},title="Moment vs Temperature"
	CheckBox plot1,variable= root:Packages:MainControlPPMS:VSM_MvsT
	CheckBox plot2,pos={195,49},size={95,14},title="Moment vs Field"
	CheckBox plot2,variable= root:Packages:MainControlPPMS:VSM_MvsH
	CheckBox plot3,pos={195,72},size={156,14},title="Susceptibility vs
Temperature"
	CheckBox plot3,variable= root:Packages:MainControlPPMS:VSM_XvsT

	SetDataFolder dfSave
EndMacro

//.....
Function GraphSingleVSMProc(ctrlName,popNum,popStr) : PopupMenuControl
	String ctrlName
	Variable popNum
	String popStr
	GraphSingleVSM(popStr)
End

//.....
Function GraphSingleVSM(wvname)
	String wvname
	//string dfSave = GetDataFolder(1)
	SetDataFolder root:data:VSM
	NVAR MvsT = root:Packages:MainControlPPMS:VSM_MvsT
	NVAR MvsH = root:Packages:MainControlPPMS:VSM_MvsH
	NVAR XvsT = root:Packages:MainControlPPMS:VSM_XvsT

	Wave Temp = $("Temper_"   + wvname)
	Wave Field = $("Field_" + wvname)
	Wave Moment = $("Moment_" + wvname)
	Wave Suscep = $("Suscep_" + wvname)


	Suscep = Suscep / Field

	if (MvsT)
		Preferences 0
		Display  Moment vs Temp;DelayUpdate
		Label bottom "Temperature (K)"
```

```
		Label left "Moment (emu)"
		Legend/C/N=text0/A=RT/X=1.73/Y=5.21
	endif

	if (MvsH)
		Preferences 0
		Display  Moment vs Field;DelayUpdate
		Label bottom "Field (Oe)"
		Label left "Moment (emu)"
		Legend/C/N=text0/A=LT/X=64.48/Y=14.22
	endif

	if (Xvst)
		Preferences 0
		Display  Suscep vs Temp;DelayUpdate
	endif

	Execute "GraphVSMStyle()"


End

//.....

Proc GraphVSMStyle() : GraphStyle
	PauseUpdate; Silent 1		// modifying window...


EndMacro

//.....
Window MainPPMSControlPanel() : Panel
	PauseUpdate; Silent 1		// building window...
	NewPanel /W=(564.75,55.25,945.75,380)
	SetDrawLayer UserBack
	SetDrawEnv fsize= 14,fstyle= 1
	DrawText 118,28,"File Loading Utilities"
	SetDrawEnv fsize= 14,fstyle= 1
	DrawText 120,193,"Magnetic Display Utilities"
	SetDrawEnv linethick= 10,linepat= 4,linefgc= (30464,30464,30464)
	DrawLine 15,164,363,164
	Button
ChoosePath,pos={120,51},size={140,20},proc=ChoosePathProc,title="Choose Path to
Data Files"
```

```
	Button LoadVSM,pos={12,94},size={170,20},proc=LoadVSMProc,title="Load
VSM data file"
	Button
LoadACMS,pos={196,94},size={170,20},proc=LoadACMSProc,title="Load ACMS
data file"
	Button
DisplaySingleVSM,pos={14,211},size={170,20},proc=DisplaySingleVSMProc,
title="Plot a single VSM run"
	Button
button0,pos={207,210},size={170,22},proc=ACFrequencySeperatorProc,title="AC
Frequency Seperator"
EndMacro

//.....
```

APPENDIX B

IGOR MACRO FOR DETERMINING METAL BINDING ISOTHERMS

APPENDIX B

Macro for Metal Binding

This macro is an igor procedure that was written as a joint effort of Gautam Basu, Mark Allen, Trevor Douglas, and Lars Liepold. This particular version involves a macro on determining the dissociation constant for a metal binding run on which 9 additions of a metal solution (a total of 10 spectra) were made while monitoring the fluorescence from 308-580 nm in 1 nm increments. The macro has several sections including loading the fluorescence spectra, baseline correcting the data by deleting all points that are part of a peak and doing a polynomial subtraction, fitting the data with a Gaussian at both the Trp fluorescence peak and the Tb^{3+} fluorescence peak, plotting the highest point on each peak vs Tb^{3+} concentration and finally normalizing each peak to gain the fraction bound to the cage and thus the dissociation constant.

Macro:

```
Function/D mono_fit(w,x)
      Wave/D w; Variable/D x
      return (w[0]*w[1]*x/(1.0+w[1]*x))
//       This can be correlated to the same formula as the theta = K[Mfree]/(1+K[Mfree])
//       w[0] is the same as w_0 in the fit results and is equal to the limiting fluorescence
//       w[1] is the same as w_1 and is the association constant or 1/Kd
//       When writing the isotherm and raw parts of the macro, in the FuncFit line
//       make it read "FuncFit/H="10" mono_fit w_new
//       The number 10 does not mean 10, it means 1 and 0 or for two variables (w[0] and
w[1])
//       The one means that the number can be varied i.e. in the fit the Kd is varied in
order to
//       get the best fit or w_1 (w[1]) can be varied
//       and the 0 means that the variable is set constant or w_1
```

```
endmacro

Macro load_fl()
	LoadWave/G/D/A=wave/P=home "inp0" // Load fluorescence data
	LoadWave/G/D/A=wave/P=home "inp1"
	LoadWave/G/D/A=wave/P=home "inp2"
	LoadWave/G/D/A=wave/P=home "inp3"
	LoadWave/G/D/A=wave/P=home "inp4"
	LoadWave/G/D/A=wave/P=home "inp5"
	LoadWave/G/D/A=wave/P=home "inp6"
	LoadWave/G/D/A=wave/P=home "inp7"
	LoadWave/G/D/A=wave/P=home "inp8"
	LoadWave/G/D/A=wave/P=home "inp9"
	LoadWave/G/D/A=wave/P=home "inp10"

	Rename wave0, lambda; // kill and rename data
	Rename wave1, fl0;
	KillWaves wave2
	Rename wave3, fl1;
	KillWaves wave4
	Rename wave5, fl2;
	KillWaves wave6
	Rename wave7, fl3;
	KillWaves wave8
	Rename wave9, fl4;
	KillWaves wave10
	Rename wave11, fl5;
	KillWaves wave12
	Rename wave13, fl6;
	KillWaves wave14
	Rename wave15, fl7;
	KillWaves wave16
	Rename wave17, fl8;
	KillWaves wave18
	Rename wave19, fl9;
	KillWaves wave20
	Rename wave21, fl10;

	LoadWave/G/D/A=wave/P=home "vol_add"
	Rename wave0 vol_add
	LoadWave/G/D/A=wave/P=home "conc_add"
	Rename wave0 conc_add
	Duplicate vol_add vol_ini
	Duplicate vol_add sub_ini
```

```
End Macro

Macro vol(xval,yval)
	Variable xval, yval // declare numeric params
	Prompt xval, "Enter initial vol(ul): " // set prompt for xval param
	Prompt yval, "Enter initial subunit conc (umol): "
	vol_ini=xval
	sub_ini=yval
End Macro

Macro cal_conc()
	Duplicate vol_add I544
	Duplicate vol_add I350
	Duplicate vol_add frac_bound
	Duplicate vol_add frac_bound_trp
	Duplicate vol_add total_Tb
	Duplicate vol_add total_Tb_trp
	Duplicate vol_add free_Tb
	Duplicate vol_add free_Tb_trp
	Duplicate vol_add vol_corr
	Duplicate vol_add vol_int
	Integrate vol_int

	Variable lim=numpnts(vol_add) // use input parameter as the loop limit
	Variable i,sum=0	// use i as the loop variable
	do
		sum += conc_add(i) * vol_add(i) / (vol_int(i) + vol_ini(i)) // loop body
		total_Tb(i)= sum
		i += 1 // increment our loop variable
	while(i <lim)

	vol_corr = vol_add + vol_ini
	vol_corr = vol_corr / vol_ini
End Macro

Macro baseline()
	Duplicate lambda w0
	Duplicate fl0 f0
	Duplicate fl1 f1
	Duplicate fl2 f2
	Duplicate fl3 f3
	Duplicate fl4 f4
	Duplicate fl5 f5
	Duplicate fl6 f6
```

```
Duplicate fl7 f7
Duplicate fl8 f8
Duplicate fl9 f9
Duplicate fl10 f10
DeletePoints 1,184, w0,f0,f1,f2,f3,f4,f5,f6,f7,f8,f9,f10
Make/N=273/D f0_new,f1_new,f2_new,f3_new,f4_new,f5_new,f6_new
Make/N=275/D f7_new,f8_new,f9_new,f10_new
CurveFit poly 3, f0 /X=w0 /D
f0_new=fl0-poly(W_coef,lambda)
CurveFit poly 3, f1 /X=w0 /D
f1_new=fl1-poly(W_coef,lambda)
CurveFit poly 3, f2 /X=w0 /D
f2_new=fl2-poly(W_coef,lambda)
CurveFit poly 3, f3 /X=w0 /D
f3_new=fl3-poly(W_coef,lambda)
CurveFit poly 3, f4 /X=w0 /D
f4_new=fl4-poly(W_coef,lambda)
CurveFit poly 3, f5 /X=w0 /D
f5_new=fl5-poly(W_coef,lambda)
CurveFit poly 3, f6 /X=w0 /D
f6_new=fl6-poly(W_coef,lambda)
CurveFit poly 3, f7 /X=w0 /D
f7_new=fl7-poly(W_coef,lambda)
CurveFit poly 3, f8 /X=w0 /D
f8_new=fl8-poly(W_coef,lambda)
CurveFit poly 3, f9 /X=w0 /D
f9_new=fl9-poly(W_coef,lambda)
CurveFit poly 3, f10 /X=w0 /D
f10_new=fl10-poly(W_coef,lambda)
CurveFit poly 3, f11 /X=w0 /D
f11_new=fl11-poly(W_coef,lambda)
CurveFit poly 3, f12 /X=w0 /D
f12_new=fl12-poly(W_coef,lambda)

Duplicate f0_new f0_newTb
Duplicate f1_new f1_newTb
Duplicate f2_new f2_newTb
Duplicate f3_new f3_newTb
Duplicate f4_new f4_newTb
Duplicate f5_new f5_newTb
Duplicate f6_new f6_newTb
Duplicate f7_new f7_newTb
Duplicate f8_new f8_newTb
Duplicate f9_new f9_newTb
```

```
	Duplicate f10_new f10_newTb

K0=0
	CurveFit/H="1000" gauss f0_new[15,66] /X=lambda /D
	I350(0)=W_coef[1]
	CurveFit/H="1000" gauss f1_new[15,66] /X=lambda /D
	I350(1)=W_coef[1]
	CurveFit/H="1000" gauss f2_new[15,66] /X=lambda /D
	I350(2)=W_coef[1]
	CurveFit/H="1000" gauss f3_new[15,66] /X=lambda /D
	I350(3)=W_coef[1]
	CurveFit/H="1000" gauss f4_new[15,66] /X=lambda /D
	I350(4)=W_coef[1]
	CurveFit/H="1000" gauss f5_new[15,66] /X=lambda /D
	I350(5)=W_coef[1]
	CurveFit/H="1000" gauss f6_new[15,66] /X=lambda /D
	I350(6)=W_coef[1]
	CurveFit/H="1000" gauss f7_new[15,66] /X=lambda /D
	I350(7)=W_coef[1]
	CurveFit/H="1000" gauss f8_new[15,66] /X=lambda /D
	I350(8)=W_coef[1]
	CurveFit/H="1000" gauss f9_new[15,66] /X=lambda /D
	I350(9)=W_coef[1]
	CurveFit/H="1000" gauss f10_new[15,66] /X=lambda /D
	I350(10)=W_coef[1]
	K0=I350(0)
	I350=I350 - K0

K0=0
	CurveFit/H="1000"  gauss f0_newTb[234,248]/X=lambda /D
	I544(0)=W_coef[1]
	CurveFit/H="1000"  gauss f1_newTb[234,248]/X=lambda /D
	I544(1)=W_coef[1]
	CurveFit/H="1000"  gauss f2_newTb[234,248]/X=lambda /D
	I544(2)=W_coef[1]
	CurveFit/H="1000"  gauss f3_newTb[234,248]/X=lambda /D
	I544(3)=W_coef[1]
	CurveFit/H="1000"  gauss f4_newTb[234,248]/X=lambda /D
	I544(4)=W_coef[1]
	CurveFit/H="1000"  gauss f5_newTb[234,248]/X=lambda /D
	I544(5)=W_coef[1]
	CurveFit/H="1000"  gauss f6_newTb[234,248]/X=lambda /D
	I544(6)=W_coef[1]
	CurveFit/H="1000"  gauss f7_newTb[234,248]/X=lambda /D
```

```
	I544(7)=W_coef[1]
	CurveFit/H="1000"  gauss f8_newTb[234,248]/X=lambda /D
	I544(8)=W_coef[1]
	CurveFit/H="1000"  gauss f9_newTb[234,248]/X=lambda /D
	I544(9)=W_coef[1]
	CurveFit/H="1000"  gauss f10_newTb[234,248]/X=lambda /D
	I544(10)=W_coef[1]
	K0=I544(0)
	I544=I544 - K0
EndMacro


Macro graphs()
	Display /W=(49,43,254,212) fl0,fl1,fl2,fl3,fl4,fl5,fl6,fl7,fl8 vs lambda
	AppendToGraph fl9,fl10 vs lambda
	ModifyGraph tick=2
	ModifyGraph mirror=2
	ModifyGraph lblMargin(left)=8,lblMargin(bottom)=3
	ModifyGraph lblLatPos(left)=1,lblLatPos(bottom)=-1
	Label left "\\Z12Raw Fluorescence"
	Label bottom "\\Z12Wavelength"
	   TextBox/C/N=text0/A=MT/E "Uncorrected fluorescence"
	Display /W=(271,45,473,214) f0_new,f1_new,f2_new,f3_new,f4_new vs lambda
	AppendToGraph f5_new,f6_new,f7_new,f8_new,f9_new,f10_new vs lambda
	AppendToGraph fit_f0_new,fit_f1_new,fit_f2_new,fit_f3_new,fit_f4_new
	AppendToGraph fit_f5_new,fit_f6_new,fit_f7_new,fit_f8_new,fit_f9_new
	AppendToGraph fit_f10_new
	ModifyGraph rgb(fit_f0_new)=(1,3,39321),rgb(fit_f1_new)=(1,3,39321)
	ModifyGraph rgb(fit_f2_new)=(1,3,39321),rgb(fit_f3_new)=(1,3,39321)
	ModifyGraph rgb(fit_f4_new)=(1,3,39321),rgb(fit_f5_new)=(1,3 ,39321)
	ModifyGraph rgb(fit_f6_new)=(1,3,39321),rgb(fit_f7_new)=(1,3,39321)
	ModifyGraph rgb(fit_f8_new)=(1,3 ,39321),rbg(fit_f9_new)=(1,3,39321)
	ModifyGraph rgb(fit_f10_new)=(1,3,39321)
	ModifyGraph tick=2
	ModifyGraph zero=1
	ModifyGraph mirror=2
	ModifyGraph lblMargin(left)=8,lblMargin(bottom)=5
	Label left "\\Z12Corrected Fluorescence"
	Label bottom "\\Z12Wavelength"
	   TextBox/C/N=text0/A=MT/E "Trp fluorescence"

	Display /W=(271,45,473,214) f0_newTb,f1_newTb,f2_newTb,f3_newTb vs lambda
	AppendToGraph f4_newTb,f5_newTb,f6_newTb,f7_newTb,f8_newTb vs lambda
	AppendToGraph f9_newTb,f10_newTb vs lambda
```

```
	AppendToGraph fit_f0_newTb,fit_f1_newTb,fit_f2_newTb,fit_f3_newTb
	AppendToGraph fit_f4_newTb,fit_f5_newTb,fit_f6_newTb,fit_f7_newTb
	AppendToGraph fit_f8_newTb,fit_f9_newTb,fit_f10_newTb
	ModifyGraph rgb(fit_f0_newTb)=(1,3,39321),rgb(fit_f1_newTb)=(1,3,39321)
	ModifyGraph rgb(fit_f2_newTb)=(1,3,39321)rgb(fit_f3_newTb)=(1,3,39321)
	ModifyGraph rgb(fit_f4_newTb)=(1,3,39321),rgb(fit_f5_newTb)=(1,3 ,39321)
	ModifyGraph rgb(fit_f6_newTb)=(1,3,39321),rgb(fit_f7_newTb)=(1,3,39321)
	ModifyGraph rgb(fit_f8_newTb)=(1,3,39321),rgb(fit_f9_newTb)=(1,3,39321)
	ModifyGraph rgb(fit_f10_newTb)=(1,3,39321)
	ModifyGraph tick=2
	ModifyGraph zero=1
	ModifyGraph mirror=2
	ModifyGraph lblMargin(left)=8,lblMargin(bottom)=5
	Label left "\\Z12Corrected Fluorescence"
	Label bottom "\\Z12Wavelength"
	TextBox/C/N=text0/A=MT/E "Terbium Fluorescence"

Macro bind_raw()
	Make/N=2/D w_raw
	w_raw(0)=I544(numpnts(vol_add)-1)
	w_raw(1)=1.0
	Duplicate vol_add Tb_by_prot
	Tb_by_prot=total_Tb/sub_ini
	FuncFit/H="10" mono_fit w_raw I544 /X=total_Tb /D
	Display /W=(49,249,252,428) I544 vs total_Tb
	AppendToGraph fit_I544
	AppendToGraph/B=newaxis I544 vs Tb_by_prot
	ModifyGraph mode(I544)=3,mode(I544#1)=2
	ModifyGraph marker(I544)=8,marker(I544#1)=41
	ModifyGraph msize(I544)=5,msize(I544#1)=5
	ModifyGraph mrkThick(I544)=1,mrkThick(I544#1)=1
	ModifyGraph tick(left)=2,tick(bottom)=2
	ModifyGraph mirror(left)=2,mirror(bottom)=2
	ModifyGraph lblMargin(left)=12,lblMargin(bottom)=3
	ModifyGraph axOffset(bottom)=5.66667
	ModifyGraph lblPos(bottom)=33,lblPos(newaxis)=40
	ModifyGraph lblLatPos(bottom)=-4,lblLatPos(newaxis)=2
	ModifyGraph freePos(newaxis)=46
	Label left "\\Z12I544"
	Label bottom "\\Z12Total [Tb], u mol"
	Label newaxis "\\Z12Total [Tb] / [Sub Unit]"

	  TextBox/C/N=text0/A=MT/E "Raw Fit"
```

```
//      String fitText
//        sprintf fitText, "\JCRaw Fit \rKd (uM) =%g ± %g", 1/(w_raw(1)),
(W_sigma(1)/w_raw(1))*(1/(w_raw(1)))
//        TextBox/C/N=FitResults/A=MT/E fitText


       Make/N=2/D w_rawtrp
       w_rawtrp(0)=I350(numpnts(vol_add)-1)
       w_rawtrp(1)=1.0
       FuncFit/H="10" mono_fit w_rawtrp I350/X=total_Tb /D
       Display /W=(49,249,252,428) I350 vs total_Tb
       AppendToGraph fit_I350
       AppendToGraph/B=newaxis I350 vs Tb_by_prot
       ModifyGraph mode(I350)=3,mode(I350#1)=2
       ModifyGraph marker(I350)=8,marker(I350#1)=41
       ModifyGraph msize(I350)=5,msize(I350#1)=5
       ModifyGraph mrkThick(I350)=1,mrkThick(I350#1)=1
       ModifyGraph tick(left)=2,tick(bottom)=2
       ModifyGraph mirror(left)=2,mirror(bottom)=2
       ModifyGraph lblMargin(left)=12,lblMargin(bottom)=3
       ModifyGraph axOffset(bottom)=5.66667
       ModifyGraph lblPos(bottom)=33,lblPos(newaxis)=40
       ModifyGraph lblLatPos(bottom)=-4,lblLatPos(newaxis)=2
       ModifyGraph freePos(newaxis)=46
       Label left "\\Z12I350"
       Label bottom "\\Z12Total [Tb], u mol"
       Label newaxis "\\Z12Total [Tb] / [Sub Unit]"

          TextBox/C/N=text0/A=MT/E "Raw Tb"

//      String fitText
//        sprintf fitText, "\JCRaw Fit \rKd (uM) =%g ± %g", 1/(w_raw(1)),
(W_sigma(1)/w_raw(1))*(1/(w_raw(1)))
//        TextBox/C/N=FitResults/A=MT/E fitText
//


          Make/N=1/D num_bind
      num_bind=1
EndMacro

//        Macro binding_sites(xxval)
```

```
//              Variable xxval // declare numeric params
//              Prompt xxval, "Enter number of bindinng sites / sub unit: " // set prompt for
xxval param
//              Duplicate vol_add num_bind
//              num_bind=xxval
//        End Macro

Macro bind_isotherm()
      Make/N=2/D w_isotherm
      w_isotherm(0)=1.0
      w_isotherm(1)=1.0
      frac_bound=I544/w_raw(0)
      free_Tb=total_Tb-(num_bind*frac_bound)
      FuncFit/H="10"  mono_fit w_isotherm frac_bound /X=free_Tb /D
      Display /W=(277,252,475,428) frac_bound vs free_Tb
      AppendToGraph fit_frac_bound
      ModifyGraph mode(frac_bound)=3
      ModifyGraph marker(frac_bound)=8
      ModifyGraph msize(frac_bound)=5
      ModifyGraph mrkThick(frac_bound)=1
      ModifyGraph tick=2
      ModifyGraph mirror=2
      ModifyGraph lblMargin(left)=7,lblMargin(bottom)=4
      Label left "\\Z12Fraction Bound (Tb)"
      Label bottom "\\Z12Free [Tb] / u mol"

      Make/N=2/D w_isotherm_trp
      w_isotherm_trp(0)=1.0
      w_isotherm_trp(1)=1.0
      frac_bound_trp=I350/w_rawtrp(0)
      free_Tb_trp=total_Tb-(num_bind*frac_bound_trp)
      FuncFit/H="10"  mono_fit w_isotherm_trp frac_bound_trp /X=free_Tb_trp /D
      Display /W=(277,252,475,428) frac_bound_trp vs free_Tb_trp
      AppendToGraph fit_frac_bound_trp
      ModifyGraph mode(frac_bound_trp)=3
      ModifyGraph marker(frac_bound_trp)=8
      ModifyGraph msize(frac_bound_trp)=5
      ModifyGraph mrkThick(frac_bound_trp)=1
      ModifyGraph tick=2
      ModifyGraph mirror=2
      ModifyGraph lblMargin(left)=7,lblMargin(bottom)=4
      Label left "\\Z12Fraction Bound (Trp)"
      Label bottom "\\Z12Free [Tb] / u mol"
EndMacro
```

```
Macro dissociation_constants()
	Print ""
	Print " ====================="
	Print "Kd (Tb) (Raw Data), in Micro Molar IS: ", 1/(w_raw(1))
	Print "Kd (Tb) (ISOTHERM), in Micro Molar IS: ", 1/(w_isotherm(1))
	Print " ====================="
	Print ""

		Print ""
	Print " ====================="
	Print "Kd (trp)(Raw Data), in Micro Molar IS: ", 1/(w_rawtrp(1))
	Print "Kd (trp) (ISOTHERM), in Micro Molar IS: ", 1/(w_isotherm_trp(1))
	Print " ====================="
	Print ""
EndMacro

Macro HillPlot()
	Make/N=14/D '1-Y',Hill,'Log(Tb)'
	'1-Y' = 1 - frac_bound
	Hill = log(frac_bound / '1-Y')
	'Log(Tb)' = log(free_Tb)
	Display Hill vs 'Log(Tb)'
	ModifyGraph mode=3,marker=8
EndMacro
```

APPENDIX C

IGOR MACRO FOR COMPETITIVE BINDING STUDIES

APPENDIX C

Macro for Competitive Binding

This macro is an igor procedure that was written as a joint effort of Gautam Basu and Mark Allen. Many of the aspects of this macro are also covered in appendix 2; this is an abridged version involving one addition particular version involves a macro on determining the dissociation constant for a metal binding run on which 9 additions of a metal solution were made while monitoring the fluorescence from 308-580 nm in 1 nm increments. The macro has several sections including loading the fluorescence spectra, baseline correcting the data by deleting all points that are part of a peak and doing a polynomial subtraction, fitting the data with a Gaussian at both the Trp fluorescence peak and the Tb^{3+} fluorescence peak, plotting the highest point on each peak vs Tb^{3+} concentration and finally normalizing each peak to gain the fraction bound to the cage and thus the dissociation constant.

Macro:

```
#pragma rtGlobals=1             // Use modern global access method.


Function/D monodecay(w,x)
        Wave/D w; Variable/D x
      return w[0] * w[1] / (x + w[1]) + (1-w[0])
endmacro

Macro load_fl()
        LoadWave/G/D/A=wave/P=home "inp0"        // Load fluorescence data
        LoadWave/G/D/A=wave/P=home "inp1"
```

```
        Rename wave0, lambda;                   // kill and rename data
        Rename wave1, fl0;
        KillWaves  wave2
        Rename wave3, fl1;

        LoadWave/G/D/A=wave/P=home "vol_add"       // load vol and conc
        Rename wave0,vol_add;
        LoadWave/G/D/A=wave/P=home "conc_add"
        Rename wave0,conc_add;

      Make/N=2/D w_mono

//      LoadWave/G/D/A=wave/P=home "etc"
//      Rename wave0,etc_inp;

End Macro

Macro vol(xval,yval,zval) // read initial volume and initial concentrations
      Variable xval, yval, zval // declare numeric params
      Prompt xval, "Enter initial cuvette vol(ul): "       // set prompt for xval param
      Prompt yval, "Enter initial Tb conc (umol): "
      Prompt zval, "Enter initial subunit conc (umol): "

      Duplicate vol_add vol_ini
      Duplicate vol_add sub_ini
      Duplicate vol_add total_Tb

      vol_ini=xval
      total_Tb=yval
      sub_ini = zval
End Macro


Macro cal_conc()

      Duplicate total_Tb total_cat
      Duplicate vol_add vol_int vol_corr
      Integrate vol_int

      Variable lim=numpnts(vol_add) // use input parameter as the loop limit
      Variable i,sum=0       // use i as the loop variable
      do
            sum += conc_add(i) * vol_add(i) / (vol_int(i) + vol_ini(i)) // loop body
```

```
            total_cat(i)= sum
            vol_corr = vol_ini(i) / (vol_int(i) + vol_ini(i))
            total_Tb (i) = total_Tb(0) * vol_corr(i)
            i += 1 // increment our loop variable
        while(i <lim)

End Macro


Macro baseline()

      Duplicate total_Tb I544

          Duplicate lambda w0
          Duplicate fl0 f0
          Duplicate fl1 f1
          DeletePoints 50,175, w0,f0,f1
          Make/N=251/D f0_new,f1_new
          CurveFit poly 3, f0 /X=w0 /D
          f0_new=fl0-poly(W_coef,lambda)
          CurveFit poly 3, f1 /X=w0 /D
          f1_new=fl1-poly(W_coef,lambda)
          K0=0

          CurveFit/H="1000" gauss f0_new /X=lambda /D
          I544(0)=W_coef[1]
          CurveFit/H="1000" gauss f1_new /X=lambda /D
          I544(1)=W_coef[1]
          I544=I544/vol_corr
          K0=I544(0)
      Duplicate total_Tb          frac_bound
          frac_bound=I544/K0
          Duplicate total_Tb Tb_conc cat_conc cat_by_Tb
          Tb_conc = Total_Tb - sub_ini*(frac_bound)
          cat_conc = Total_cat - sub_ini*(1.0-frac_bound)
          Cat_by_Tb = Cat_conc / Tb_conc
EndMacro

Macro graphs()
          Display /W=(5,42,314,289) fl0,fl1 vs lambda as "raw_fl"
          ModifyGraph tick=2
          ModifyGraph mirror=2
          Label left "\\Z12Fluorescence"
          Label bottom "\\Z12Wavelength (nm)"
```

```
	Display /W=(5,42,314,289) f0,f1 vs w0 as "bline_fl"
	ModifyGraph tick=2
	ModifyGraph mirror=2
	Label left "\\Z12Fluorescence"
	Label bottom "\\Z12Wavelength (nm)"

	Display /W=(5,42,314,289) f0_new,f1_new vs lambda as "final_fl"
	ModifyGraph tick=2
	ModifyGraph mirror=2
	Label left "\\Z12Fluorescence"
	Label bottom "\\Z12Wavelength (nm)"

	Display /W=(5,42,314,289) frac_bound vs cat_by_tb as "comp_fl"
	ModifyGraph tick=2
	ModifyGraph mirror=2
	Label left "\\Z12Fraction (CCMV) bound to Tb"
	Label bottom "\\Z12[Cation]/[Tb]"
	ModifyGraph mode(frac_bound)=3
	ModifyGraph marker(frac_bound)=19
	ModifyGraph msize(frac_bound)=4
EndMacro

Macro fit_comp()
w_mono={1.0,50}
FuncFit monodecay w_mono frac_bound /X=cat_by_tb /D
EndMacro

Function/D comp_binding(w,x)

	Wave/D w; Variable/D x

//  w[0] is I(max)545 in Eq. 2
//  w[1] is Kapp in Eq. 2
//  (1-w[0]) is I(lim)545 in Eq. 2
//  X is the total concentration of competitive ion

		return (  w[0] * w[1] / (X + w[1]) + (1-w[0]) )
End Macro
```